



# The Role of MreB in Producing Rod-Shaped Bacterial Cells

## Permanent link

<http://nrs.harvard.edu/urn-3:HUL.InstRepos:39988025>

## Terms of Use

This article was downloaded from Harvard University's DASH repository, and is made available under the terms and conditions applicable to Other Posted Material, as set forth at <http://nrs.harvard.edu/urn-3:HUL.InstRepos:dash.current.terms-of-use#LAA>

## Share Your Story

The Harvard community has made this article openly available.  
Please share how this access benefits you. [Submit a story](#).


[Accessibility](#)

HARVARD UNIVERSITY  
Graduate School of Arts and Sciences

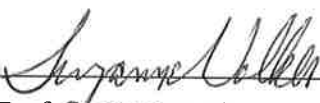


DISSERTATION ACCEPTANCE CERTIFICATE

The undersigned, appointed by the  
Department of Molecular and Cellular Biology  
have examined a dissertation entitled  
"The Role of MreB in Producing Rod-shaped Bacterial Cells"  
presented by Saman Hussain,  
candidate for the degree of Doctor of Philosophy and hereby  
certify that it is worthy of acceptance.

Signature  \_\_\_\_\_  
Typed name: Prof. Richard Losick

Signature  \_\_\_\_\_  
Typed name: Prof. Daniel Needleman

Signature  \_\_\_\_\_  
Typed name: Prof. Suzanne Walker

Date: September 5, 2017



*The Role of MreB in Producing Rod-shaped Bacterial Cells*

A dissertation presented

By

Saman Hussain

To

The Department of Molecular and Cellular Biology

in partial fulfillment of the requirements

for the degree of

Doctor of Philosophy

in the subject of

Biology

Harvard University

Cambridge, Massachusetts

September 2017

© 2017 Saman Hussain  
All rights reserved.

## The Role of MreB in Producing Rod-shaped Bacterial Cells

### **Abstract**

MreB, an actin homolog, is known to form short, membrane-associated filaments that move circumferentially in rod-shaped bacteria, in association with cell wall-synthesizing enzymes. Despite being essential for rod shape, the mechanism by which MreB filaments are able to organize themselves and move circumferentially is not known. In this thesis, I will show that MreB filaments are able to sense cell curvature and align along the dimension of greatest principal curvature. The first chapter of this thesis is an introduction where I will discuss bacterial cell shape and organization, providing an overview of the current state of knowledge in both fields, and the importance of studying them. In the second chapter, I will provide evidence for the curvature-sensing ability of MreB filaments, and show how it enables cells to both maintain rod shape from generation to generation, as well as create rod shape *de novo* in round cells. I will then provide a model for this curvature-sensing property: the intrinsic, high curvature of MreB filaments, coupled with hydrophobic residues on the filament that directly associate with membranes could allow these filaments to preferentially bind along the more curved of the two principal curvatures. In the last chapter, I will discuss the questions that remain to be answered in the field of MreB-associated cell wall synthesis, and point out future directions for the extension of my work.

## TABLE OF CONTENTS

<b>ACKNOWLEDGEMENTS</b>	<b>V</b>
<b>CHAPTER 1 - INTRODUCTION</b>	<b>1</b>
(i) BACTERIAL CELL SHAPE	1
ii) HOW DO BACTERIAL CELLS ORGANIZE THEIR CONTENTS?	10
<b>CHAPTER 2 - MREB FILAMENTS AND ROD SHAPE</b>	<b>18</b>
(ii) MAINTENANCE OF ROD SHAPE BY MREB FILAMENTS	22
(iii) <i>DE NOVO</i> CREATION OF ROD SHAPE BY MREB FILAMENTS	37
(iv) DISCUSSION AND CONCLUSION	46
<b>CHAPTER 3 FUTURE DIRECTIONS</b>	<b>53</b>
<b>APPENDIX</b>	<b>64</b>
SUPPLEMENTARY MATERIALS FOR CHAPTER 2	64
SUPPLEMENTARY MATERIALS FOR CHAPTER 3	120
<b>BIBLIOGRAPHY</b>	<b>128</b>

# Acknowledgements

I would like to thank:

- My family for their constant support and encouragement.
- My supervisor Dr. Ethan Garner for guiding, teaching and mentoring me at every step of my PhD.
- Dr. Carl Wivagg for all the guidance, experimental help and intellectual discussions.
- My qualifying exam and dissertation advisory committee members Dr. Richard Losick, Dr. Daniel Needleman, Dr. Suzanne Walker and Dr. Guido Guidotti for their valuable advice and suggestions.
- My collaborators, especially Felix Wong and Dr. Ariel Amir for their insightful discussions and comments.
- All existing and old members of the Garner lab especially Michael Dion for teaching me how to clone, Patrick Stoddard for help with biochemical work and Dr. Jenna Eun, Dr. Yingjie Sun and Dr. Alex Bisson for their help and mentoring.
- All the MCO administrative staff (old and new) especially Michael Lawrence, Patty Perez, Debbie Maddalena and Fanuel Muindi.
- The Howard Hughes Medical Institute for providing me funding through the International Student Research Fellowship program.



# Chapter 1 - Introduction

## *Overview*

In this chapter, I will first review the recent advances made in understanding bacterial cell shape, specifically rod shape formation by the actin homolog MreB. I will then discuss the organization of bacterial cells, focusing on the various strategies used by bacterial cells to organize their contents and the role bacterial polymers play in this process. The second part of this chapter has been adapted from a previously published work:

Y.-J. Eun\*, M. Kapoor\*, S. Hussain, E. C. Garner, Bacterial Filament Systems: Toward Understanding Their Emergent Behavior and Cellular Functions. *Journal of Biological Chemistry*. 290, 17181–17189 (2015).

\*These authors contributed equally to this work.

## (i) Bacterial cell shape

The focus of my thesis is a particular example of cellular organization: bacterial cell shape. The prokaryotic world is filled with a variety of cell shapes ranging from common shapes like spheres, rods and spirals to uncommon ones like star-shaped bacteria (Jiang, Caccamo, and Brun 2015). However, each bacterial species usually grows in a specific form that deviates very little from organism to organism. To understand cell shape in most bacteria, it is important to study the cell wall, a rigid outer covering that

encapsulates the cell and provides structural support. When the cell wall is degraded and removed, bacterial cells swell up and become spherical (Muchová, Wilkinson, and Barák 2011). On the other hand, if cells are killed and their cell walls isolated and examined, the walls retain their original shape (Hayhurst et al. 2008). Combined, these observations show that the cell wall confers cell shape.

The entire cell wall is one giant macromolecule whose integrity must be maintained as the cell grows and divides. It is mainly composed of peptidoglycan (PG), a polymer made of sugars with peptide side-chains that are crosslinked to form a mesh-like network around the cell (Figure 1.1A). The disaccharide subunit of peptidoglycan is N-acetylglucosamine (GlcNAc) and N-acetylmuramic acid (MurNAc) and the peptide side-chains vary between species, containing both L and D amino acids (Figure 1.1B). The monosaccharide(MurNAc)-peptide is synthesized in the cytoplasm in a series of reactions and attached to undecaprenyl phosphate to make lipid I. Lipid I is then converted to lipid II, the precursor for peptidoglycan, which is flipped to the outside of the cell (Typas et al. 2012). Incorporation of a subunit into the existing cell wall involves two steps. First, polymerization must occur to add the subunit to an existing peptidoglycan strand and second, the peptide sidechain must be crosslinked to a sidechain from an adjacent peptidoglycan strand. The second step may or may not occur as all peptides in the cell wall are not crosslinked (only about 50% of peptide sidechains in *E. coli* are crosslinked). (Glauner, Höltje, and Schwarz 1988).

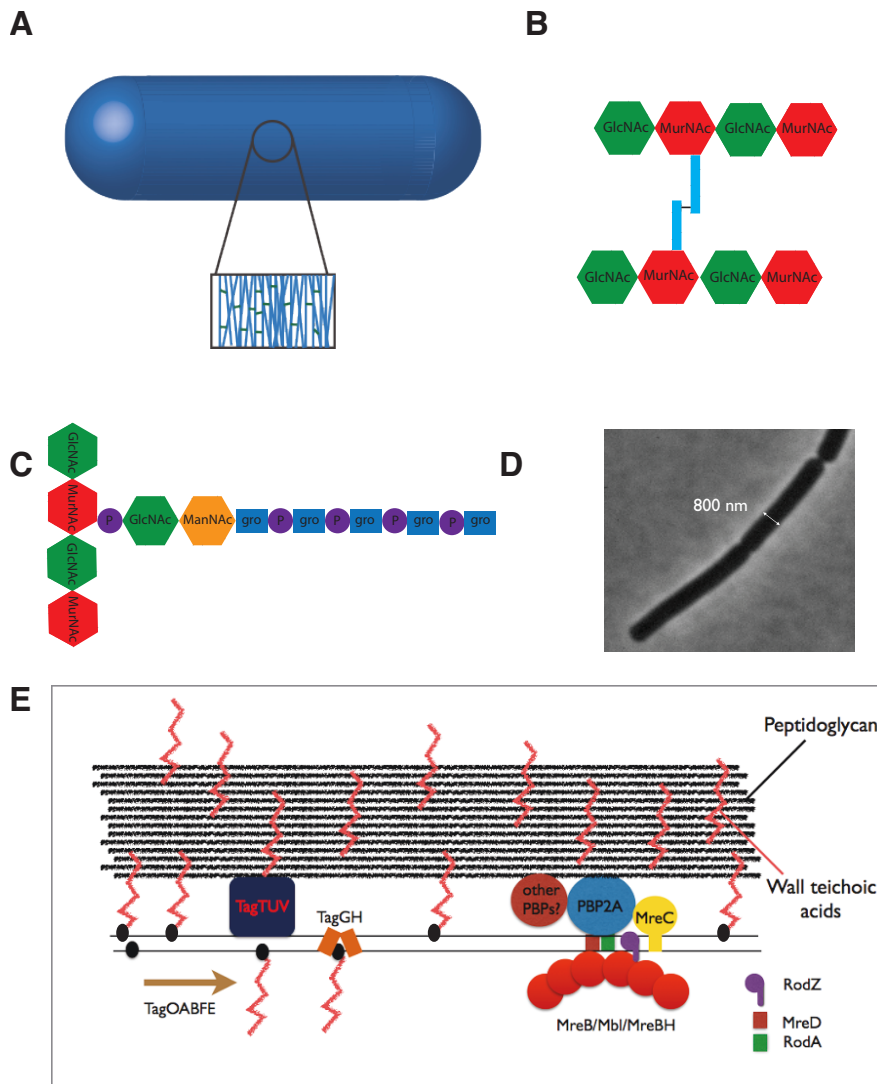


**Figure 1.1. Bacterial cell wall structure and composition.** **A)** In rod-shaped bacteria, peptidoglycan is believed to be arranged in a predominantly circumferential organization. The blue lines are glycan strands and the green lines depict peptide crosslinks between the peptidoglycan sidechains. **B)** The molecular structure of peptidoglycan showing the disaccharide subunit (GlcNAc – MurNAc) and the attached peptide sidechain (blue) that is crosslinked to another peptidoglycan strand. **C)** Molecular structure of wall teichoic acid, an important component of Gram positive cell walls, showing its composition (gro - glycerol and P - phosphate) and covalent attachment to peptidoglycan via a disaccharide subunit (GlcNAc – ManNAc). **D)** Rod shaped *Bacillus subtilis* cells growing exponentially as a chain. A constant width of 800 nm is maintained and the cells grow by increasing in length only.

**Figure 1.1 (Continued). E** A cartoon representation of cell wall synthesis in *B. subtilis* and the major enzymes and accessory proteins involved. Wall teichoic acids are synthesized and inserted into the wall by the Tag enzymes. Undecaprenyl phosphate, the lipid carrier is indicated as a black circle. Some peptidoglycan-synthesizing enzymes (PBP2A and RodA) associate with short filaments of MreB and its paralogs Mbl and MreBH, while the localization of other PBPs is unknown. MreB also associates with other proteins (MreCD, RodZ) of unknown function.

Enzymes carrying out the transglycosylation and transpeptidation reactions primarily belong to the family of penicillin binding proteins (PBPs). PBPs can be further classified into two categories: Class A PBPs, which are bifunctional, having both transglycosylase and well as transpeptidase activity and Class B PBPs, which only exhibit transpeptidase activity and have an additional domain of unknown function. In *B. subtilis*, many PBPs exist, belonging to both class A (e.g. PBP1, PBP2C, PBP4) and class B (e.g. PBP2A, PBP2B, PBP2D, PBP3, PBPI). While some of these PBPs are well known, a number of them have unknown functions as well (Errington and Wu 2017). Recently, RodA, a protein that affects cell shape and belongs to the Shape Elongation Division and Sporulation (SEDS) family of proteins, has also been discovered to have transglycosylase activity (Meeske et al. 2016).

Gram negative cell walls contain a single or double layer of peptidoglycan enclosed by an outer membrane, while Gram positive walls are composed of a 30-40 nm thick peptidoglycan layer. In addition to peptidoglycan, Gram positive cell walls also contain anionic polymers called wall teichoic acids that are covalently linked to peptidoglycan. Wall teichoic acids (WTAs) are polyol-phosphate polymers with a connecting subunit consisting of a disaccharide (N-acetylglucosamine and N-acetylmannosamine) that is

covalently attached to peptidoglycan (Figure 1.1C). WTAs are an important part of Gram positive cells wall, making up about 60% by mass of the wall and the absence of these polymers results in loss of rod shape, aberrant cell division and severely reduced growth rates (D'elia 2006). WTAs are believed to have a number of different functions, the most important being their role in scavenging cations (Brown, Santa Maria, and Walker 2013). In *B. subtilis*, WTAs are synthesized by a group of enzymes called the Tag enzymes. WTA synthesis occurs in the cytoplasm and begins by the addition of phospho-GlcNAc to the undecaprenyl phosphate carrier by the enzyme TagO. A series of intracellular steps catalyzed by TagB-F synthesize the WTA polymer, and the flippase TagGH (Schirner, Stone, and Walker 2011) flips the lipid carrying the polymer to the outside of the cell. Three partially redundant enzymes TagTUV are then proposed to covalently attach the polymer to peptidoglycan via the WTA disaccharide (phospho-GlcNAc-ManNAc) connecting unit (Figure 1.1E) (Kawai et al. 2011). The materials making up the cell wall (peptidoglycan and WTAs) do not have any intrinsic shape and thus, in order to create defined geometries, these components have to be spatially organized by the cell.

Spherical shape is the most energetically favorable conformation, given the high internal turgor pressure in bacteria, yet many bacterial species grow in other shapes, presumably due to the evolutionary advantages, such as increased cellular motility and better penetration of substrates that these other shapes confer (Chang and Huang 2014). Deviations from spherical shape require a symmetry breaking factor that can

robustly and reproducibly break cell symmetry and maintain this asymmetry over generations. One of the simplest shape asymmetry we can study is rod shape, which is also one of the most common bacterial cell shapes. To grow as a rod, the cell width needs to be fixed and growth allowed only along the cell length (Figure 1.1D).

Many models have been proposed for the arrangement of peptidoglycan in rod-shaped cell walls, but the consensus based on experimental evidence points towards a circumferential arrangement of cell wall strands. Circumferential arrangements of cell wall strands have been observed using cryo-electron and atomic force microscopy in both Gram negative and Gram positive bacteria (Hayhurst et al. 2008; Gan, Chen, and Jensen 2008; Beeby et al. 2013), although the arrangement of individual peptidoglycan chains within these strands is still unclear. This circumferential arrangement of cell wall also makes sense from a material science perspective as it enables cells to resist the higher stresses due to turgor pressure on the rod sidewalls as compared to the rod axis by aligning the stiffer glycan bonds circumferentially and the more flexible peptide bonds longitudinally (Figure 1.1A). A similar circumferential arrangement of cellulose is seen to confer rod shape in plant cells (Baskin 2005). Even at the multi-cellular level, cells secreting extracellular matrix proteins in a circumferential orientation in the *Drosophila* egg chamber during development cause it to change shape from spherical to rod-like (Gates 2012). Therefore, as a general principle across kingdoms, it appears that rod-shape is created and supported by an anisotropic outer material which constrains

expansion more along one axis than the other, although theoretically, anisotropy is by no means necessary for rod shape.

There have been significant advances in understanding the genetics underlying rod shape formation in bacteria. In bacteria such as *B. subtilis* and *E. coli* that grow dispersively (growth is uniformly distributed along the entire cell as opposed to polar growth), many genes have been identified as essential for rod shape. These fall into two main categories: 1) enzymes that synthesize and insert components of the cell wall i.e. peptidoglycan (in Gram negative and positive cell walls) and wall teichoic acids (in Gram positive cell walls only), and 2) the actin homolog MreB and its associated proteins such as RodZ, MreC, MreD. While it is easy to envision why enzymes that compose the cell wall are essential for rod shape, the role of MreB and its associated proteins has remained more elusive over the years.

While it was known earlier that MreB belonged to the actin superfamily (Bork, Sander, and Valencia 1992), in 2001, MreB was observed to form filamentous structures *in vivo* (Jones 2001). Helical filaments were observed, forming long-range, cell-spanning structures which led to proposals of MreB providing structural stability to the cell and it was hence called the bacterial 'cytoskeleton'. However, advances in imaging revealed that the observations of long helical structures were most likely artifacts of imaging and oligomerization of fluorescent protein tags (Swulius and Jensen 2012). Cryo-electron microscopy confirmed that MreB does not form helical structures in its native state *in*

*vivo* (Swulius et al. 2011). In addition, dynamic imaging of MreB using total internal reflection microscopy revealed an interesting phenomenon: MreB was observed to form short, disconnected filaments that moved circumferentially, aligned perpendicular to the long axis of the rod-shaped cell (Garner et al. 2011; van Teeffelen et al. 2011; Domínguez-Escobar et al. 2011). Other associated proteins such as RodZ, MreC, MreD, as well as the peptidoglycan synthesizing enzymes PBP2A (transpeptidase) and RodA, which has recently been shown to possess transglycosylase activity (Meeske et al. 2016, Cho et al. 2016) were also seen to move circumferentially, in association with MreB (Garner et al. 2011; van Teeffelen et al. 2011; Domínguez-Escobar et al. 2011). It was also shown that MreB filaments do not treadmill and hence do not power their own motion, rather, cell wall synthesis powers the motion of these filaments, pulling them along as the enzymes make new cell wall (Garner et al. 2011; van Teeffelen et al. 2011; Domínguez-Escobar et al. 2011). This behaviour is in contrast with actin filaments which are known to treadmill (Pollard and Borisy 2003).

Despite these advances in our knowledge of the structure and localization of MreB, its function and contribution to rod shape is still not clear. Since MreB filaments move in concert with peptidoglycan synthesizing enzymes in a circumferential manner, it is believed that their motion reflects the insertion of new cell wall, and in line with this idea, new cell wall has been observed to be inserted in a striped pattern, mirroring the trajectories of MreB filaments (Kuru et al. 2012). Hence, it has been proposed that MreB



filaments may be guiding their associated enzymes to insert new cell wall circumferentially (White and Gober 2012).

In order to guide enzymes, MreB filaments must be able to sense the cell circumference and know which way to move. Since these short, disconnected filaments have no way to gain information about global cell shape, it is unclear how they are all able to move circumferentially, perpendicular to the cell long axis. One possibility is that these filaments may be responding to cues in the existing cell wall, such as circumferential glycan strands, and using them as a template for the synthesis of new strands (Höltje 1998; White and Gober 2012). This argument, however, is weakened by the fact that L-forms lacking cell wall are able to regenerate rod shape in the absence of a template (Kawai 2014). Another idea is that these individual filament-enzyme complexes contain an intrinsic mechanism to sense the circumference and are able to align circumferentially even in the absence of cell wall, as long as a rod shape exists.

I aimed to understand the mechanism behind the circumferential motion of MreB filaments and its resultant contribution to rod shape, using the model organism *Bacillus subtilis*, a Gram positive, rod-shaped bacterium. *B. subtilis* contains 3 *mreB* homologs called *mreB* (present in the *mre* operon), and *mbl* (*mreB*-like) and *mreBH*, which are both present in distant regions of the chromosome. All 3 homologs affect cell shape and are believed to have partially redundant roles (Kawai, Asai, and Errington 2009). These homologs have been observed to co-polymerize to form mixed filaments *in vitro* and *in*

*vivo* (Dempwolff et al. 2011; Defeu Soufo and Graumann 2010). I use a variety of approaches such as *in vivo* microscopy, microfluidics and *in vitro* protein imaging to elucidate the role of MreB in creating rod-shaped cells.

## ii) How do bacterial cells organize their contents?

Living organisms of all scales are known to create ordered structures within and around themselves. By creating order, these organisms are able to grow and reproduce more efficiently (Thompson 1968). Organization is seen to emerge on all scales, from groups of cells in multicellular organisms during development, to nanometer-sized proteins and molecules that form ordered structures within cells.

One of the major roles of the eukaryotic cytoskeleton is to organize the cell (R. Li and Gunderson 2008), and with the discovery of cytoskeletal homologs in bacteria such as FtsZ and MreB, it was thought that these polymers may have similar roles. Around the same time, the discovery of fluorescent proteins and advances in imaging techniques were changing our view of the bacterial cell. Instead of containing a homogenous mixture of proteins, bacterial cells were seen to be highly organized, localizing proteins to various sub-cellular regions such as the cell poles, mid-cell and at the cell membrane (Govindarajan, Nevo-Dinur, and Amster-Choder 2012).

Certain essential processes in the cell require robust and reproducible patterns. One such process is cell division, where the cell manages to divide in half, or at a fixed

length each time. During cell division, the chromosomes also segregate between the two daughter cells in a non-random manner (Gerdes, Howard, and Szardenings 2010). Another example is cell shape, where organized cell wall synthesis ensures that the same shape is produced from generation to generation (Young 2010). Cell shape is extremely important as it sets the geometry for many downstream proteins to carry out their functions (Ben-Yehuda 2002; Becker et al. 2006; Ramamurthi et al. 2009; Møller-Jensen et al. 2003).

In addition, the bacterial chromosome itself is also organized and has a distinct structure, due to condensation by proteins belonging to the SMC family (Niki et al. 1992; Britton, Lin, and Grossman 1998; Moriya et al. 1998)<sup>3</sup>. The chromosome has a non-random spatial orientation (Nielsen et al. 2006; Teleman et al. 1998; Webb et al. 1997; X. Wang et al. 2006) that varies temporally during replication and segregation (X. Wang, Montero Llopis, and Rudner 2014). There are also reports on the localization of RNAs to regions of transcription or translation, but due to the limited methods of visualizing RNA *in vivo* and conflicting results, artifacts cannot be completely ruled out (Nevo-Dinur, Govindarajan, and Amster-Choder 2012). With the recent technical advances in imaging DNA *in vivo* (B. Chen et al. 2013), it is expected that more studies of genome organization in live cells will follow, with better spatiotemporal resolution.

Upon examining the properties of bacterial polymers that contribute to subcellular organization, it appears that they can functionally be classified into two categories: a)

polymers that form long range cell-spanning filaments to carry out organizational tasks, thus providing nanometer-sized proteins information about global cell structure and b) short polymers or oligomers that act locally but are able to organize themselves to produce long-range order.

The plasmid segregation systems ParM and AlfA, which have been studied *in vivo* and characterized *in vitro*, employ the first approach, where long-range filaments are used to find the ends of a cell, and in the process push and segregate plasmids (Garner et al. 2007; Polka et al. 2009). In addition, an actin homolog called MamK is known to form long filaments that orient magnetosomes in magnetotactic bacteria such as *Magnetospirillum* (Draper et al. 2011; Ozyamak et al. 2013).

Advances in microscopy have revealed that there is a second mechanism of subcellular organization that involves short polymers acting on local scales. In most cases, it is not completely understood how this short-scale effect is coordinated to produce long-range order. One example is the ParAB family of proteins, which are involved in the segregation of many structures, including plasmids, protein clusters, carboxysomes and, most importantly, the chromosome (Gerdes, Møller-Jensen, and Jensen 2000; Thompson, Wadhams, and Armitage 2006; Szardenings, Guymer, and Gerdes 2011; Fogel and Waldor 2006). Initially it was reported that it formed a spindle-like structure that segregates chromosomes (Ptacin et al. 2010) but there is increasing evidence that ParA forms dimers or oligomers that can be seen to move as a cloud in front of the

segregating chromosome (Lim et al. 2014). The exact mechanism of action of ParAB is still unknown.

Another example is FtsZ, a tubulin homolog that assembles in the form of a ring at the mid-cell, and is essential for cell division (Bi and Lutkenhaus 1991). Cryo-EM and super-resolution imaging have provided increasing evidence that the FtsZ ring consists of short filaments (~200nm) that form a patchy and discontinuous ring in *B. subtilis*, *E. coli*, and *C. crescentus* (Z. Li et al. 2007; Fu et al. 2010; Strauss et al. 2012; Holden et al. 2014; Biteen et al. 2012). In *B. subtilis*, short FtsZ filaments are seen to move circumferentially *in vivo* both inside as well as outside the Z ring, and treadmilling is the source of this motion (Bisson-Filho et al. 2017). In liposomes, FtsZ targeted to the membrane can assemble into a ring that is capable of constricting the membrane (Osawa and Erickson 2013; Osawa, Anderson, and Erickson 2008). FtsZ recruits PG synthesizing enzymes and other essential divisome proteins to the mid-cell, but it is still unknown whether it provides the constriction force *in vivo*. One early suggestion was that FtsZ filament curvature changes upon GTP hydrolysis, exerting force on the membrane (Lu, Reedy, and Erickson 2000). Another hypothesis is that FtsZ filaments do not undergo a change in curvature but are intrinsically more curved than the cell circumference, thus iteratively 'pinching' the membrane to produce an overall constriction (Z. Li et al. 2007). This model was supported by studies showing that attachment of an artificial amphipathic helix to either side of the bent filament could deform liposomes in opposite directions (Osawa, Anderson, and Erickson 2009). Another possibility is that FtsZ serves as a scaffold to localize peptidoglycan

synthesizing enzymes to the mid-cell, and cell wall synthesis provides the ultimate constriction force (Meier and Goley 2014). This model is difficult to test as cell wall synthesis is required for cell division and its inhibition leads to incomplete constriction (Egan and Vollmer 2013). Similarly, as discussed in Section (i), MreB was originally believed to form a cell-spanning structure but is now known to form short, diffraction-limited filaments that are able to organize their motion to move circumferentially, perpendicular to the long axis of cells. Thus, many of the major organizational tasks in bacteria seem to be carried out by short, dynamic polymers or oligomers, bringing into question whether a bacterial 'cytoskeleton' exists and is needed to organize the bacterial cell.

Crescentin, an intermediate filament homolog, plays a role in determining cell shape in *Caulobacter crescentus*. Cells lacking crescentin lose their curved morphology (Ausmees, Kuhn, and Jacobs-Wagner 2003). Crescentin forms filaments that localize to the positively curved part of the cell (relative to the inside) (Charbon, Cabeen, and Jacobs-Wagner 2009) and exhibit slow exchange with cytoplasmic crescentin, as revealed by FRAP and FLIP experiments (Esue, Rupprecht, Sun, and Wirtz 2010a). The exact mechanism of action of crescentin and its interacting partners are unknown and so it cannot be said whether crescentin acts locally or globally to carry out its function. However, rheology experiments by Esue *et al.* indicate that crescentin is significantly less stiff than eukaryotic IFs, making it unlikely that it can form a global structure that forces the cell to curve (Esue, Rupprecht, Sun, and Wirtz 2010b). An

alternate idea is that crescentin reduces new cell wall insertion where it binds, and this differential insertion of PG produces a curved morphology (Cabeen et al. 2009).

Bacterial cells also employ other strategies to localize proteins. Recently, membrane curvature has been recognized as an important cue for protein localization. The first protein identified was SpoVM in *B. subtilis*, which localizes to positive membrane curvature and hence is able to distinguish between the endospore and the mother cell (Ramamurthi et al. 2009). Next, it was shown that DivIVA in *B. subtilis* binds to regions of negative curvature, which is why it is able to localize to the cell poles and septa (Ramamurthi et al. 2009). These proteins, in turn, act as anchors for many other proteins. SpoVM recruits coat proteins that assemble on the endospore and form the spore coat (McKenney, Driks, and Eichenberger 2013). DivIVA recruits MinJ, MinD and RacA to the cell pole (Marston et al. 1998; Ben-Yehuda 2002). MinD in turn recruits MinC, which prevents the formation of the FtsZ ring at the pole (de Boer, Crossley, and Rothfield 1992). RacA anchors the chromosome to the cell pole during sporulation (Ben-Yehuda 2002).

In *E. coli*, a different approach is used to prevent the FtsZ ring from forming at the poles. An additional protein, MinE, dephosphorylates MinD and results in oscillations of MinCD gradients that have a time averaged minimum at the mid-cell (Raskin and de Boer 1999). This strategy uses the differential localization of MinD in the nucleotide-bound and nucleotide-free state to produce a self-organized system of protein gradients, which

inhibits FtsZ assembly at the poles. In *C. crescentus*, MipZ inhibits the formation of the FtsZ ring at the pole by associating with the origin of the chromosome through interactions with ParB (Thanbichler and Shapiro 2006). MipZ has been shown to form a nucleotide dependent gradient around the chromosome origin, rather than discrete foci, indicating that there is a dynamic exchange of protein between the cytoplasm and the chromosome (Thanbichler and Shapiro 2006). By binding to the origin and promoting the disassembly of FtsZ, MipZ acts as a spatial co-ordinator between chromosome segregation and cell division. PopZ, the chromosome anchoring protein in *C. crescentus*, has been shown to multimerize at the pole in a ParA-dependent manner (Laloux 2013).

From the above examples, it is clear that long-range filaments are not a requirement for cellular organization, and both short filaments acting locally, as well as reaction-diffusion systems and other cues such as curvature are able to guide subcellular organization. It is also known that not all long-range filaments contribute to organizing the cell. In yeast, metabolic enzymes form filaments that do not appear to play any role in organizational tasks (O'Connell et al. 2012; Noree et al. 2010; Narayanaswamy et al. 2009).

Recent evidence has brought into question the validity of some of the subcellular organization observed (Landgraf et al. 2012). Landgraf *et al.* showed that Clp protease clusters, which were believed to be functionally relevant, were a consequence of fluorescent protein oligomerization in *E. coli*. Further tests revealed that five other



proteins in *E. coli* also formed foci due to the clustering of fluorescent proteins, indicating that this might be a common phenomenon. Additionally, most fluorescently-tagged proteins in these studies were expressed under inducible promoters, with expression levels many times above their wild type, which contributed to their aggregation. Recent work by Wang *et al.* showed that even monomeric photoactivatable proteins such as mMaple are prone to dimerization (Wang et al. 2014). They reported variations in the localization of proteins, including nucleoid-associated proteins such as H-NS and HU, when different photoactivatable proteins were used to tag them. These studies highlight the importance of selecting a suitable fluorescent protein tag when doing localization studies.

Protein localization helps organize cells and enables them to carry out essential processes like growth and division. However, it should be noted that in some cases localization may not be functionally relevant. It could be a consequence of the crowded environment of the cell, which limits diffusion and enhances the clustering of proteins translated together (Zimmerman and Trach 1991; Mika and Poolman 2011). Co-transcriptional translation further restricts the mobility of proteins and RNA. Polar localizations may simply be due to exclusion from the chromosomal space (Saberly and Emberly 2010). These recent ideas are hinting towards a heterogeneous cellular environment in bacteria that displays certain principles of organization to help with major organizational tasks, but is ultimately dominated by Brownian motion, due to the smaller spatial scales involved.

## Chapter 2 - MreB filaments and rod shape

### *Overview*

In this chapter, I will provide evidence that MreB filaments are able to sense cell membrane curvature, which enables them to create and maintain rod shape. This chapter is a publication that is currently in review:

Hussain, S.\* , Wivagg C. N.\* , Szwedziak P., Wong F., Izore´ T., Renner L. D., Amir A., Löwe J., Garner E. C. MreB filaments create rod shape by aligning along principal membrane curvature. *In review*.

\*These authors contributed equally to this work.

### (i) Introduction

Although many bacteria are rod shaped, the cellular mechanisms that construct and replicate this geometry have remained largely unknown. Bacterial shape is determined by the cell wall sacculus, a giant, encapsulating macromolecule that serves to resist internal turgor pressure. One of the primary components of the cell wall is peptidoglycan (PG), which is created by the polymerization of single glycan strands linked by peptide crossbridges. Studies of isolated cell walls from rod-shaped bacteria suggest that glycan strands are generally oriented circumferentially around the rod, perpendicular to the long axis of the cell (Gan, Chen, and Jensen 2008; Hayhurst et al. 2008; Verwer 1980). This circumferential, hoop-like organization of cell wall material allows the cell wall to better resist the internal turgor pressure, which is twice as large in the

circumferential direction (on the rod sidewalls) than the axial direction (Chang and Huang 2014). This organization confers a mechanical anisotropy to the wall: the mechanically weaker crosslinks in the axial direction allow the cell wall to stretch more along its length than across its width for a given stress, and this anisotropy may assist rod-shaped cells in preferentially elongating along their length (Chang and Huang 2014). Concordantly, atomic force microscopy (AFM) has shown that *Escherichia coli* sacculi are 2-3 times more elastic along their length than across their width (Yao et al. 1999). This rod-reinforcing circumferential organization is also observed in the cell walls of plants; hypocotyl and root axis cells rapidly elongate as rods by depositing cellulose fibrils in circumferential bands around their width, resulting not only in a similar dispersive rod-like growth, but also a similar anisotropic response to stress (Baskin, 2005). The organized deposition of cellulose arises from cortical microtubules self-organizing into a radial array oriented around the rod width, and this orients the directional motions of the cellulose synthases to insert material in circumferential bands (Paredes 2006).

In contrast to our understanding of the self-organization underlying rod-shaped growth in plants, how bacteria construct a circumferential organization of glycan strands is not known. This organization may arise via the actions of a small number of genes known to be essential for the formation and maintenance of rod shape. Collectively termed the Rod complex, these include the conserved *mreBCD* operon (Wachi and Matsushashi, 1989) and the glycosyltransferase/transpeptidase enzyme pair RodA/Pbp2 (Cho et al.,

2016). The spatial coordination of RodA/Pbp2-mediated PG synthesis is conferred by *mreB*, an actin homolog (Jones 2001). MreB polymerizes onto membranes as antiparallel double filaments, which have been observed to bend liposome membranes inward (Figure 2.1A) (Salje et al. 2011; van den Ent, Izoré, et al. 2014). Loss or depolymerization of MreB causes rod-shaped cells to grow as spheres (Jones 2001). *In vivo*, MreB filaments move circumferentially around the width of the rod (Domínguez-Escobar et al. 2011; Garner et al. 2011; van Teeffelen et al. 2011). Super-resolution imaging has demonstrated that MreB filaments always translocate along their length, moving in the direction of their orientation (Olshausen et al. 2013). MreB filaments move in concert with MreC, MreD, and RodA/Pbp2 (Domínguez-Escobar et al. 2011; Garner et al. 2011), and loss of any one component stops the motion of the others. The directional motion of MreB filaments and associated Rod complexes depends on, and thus likely reflects, the insertion of new cell wall, as this motion halts upon the addition of cell wall synthesis-inhibiting antibiotics (Domínguez-Escobar et al. 2011; Garner et al. 2011; van Teeffelen et al. 2011), or specific inactivation or depletion of Pbp2 (Garner et al. 2011; van Teeffelen et al. 2011) or RodA (Cho et al., 2016).

It is not known how MreB and its associated PG-synthetic enzymes construct rod-shaped cells. As the motions of the Rod complexes reflect the insertion of new cell wall, the circumferential motions could deposit glycans in the hoop-like organization required to both build and reinforce rod shape. Therefore, we worked to understand the origin of this circumferential organization, seeking to determine what orients the motions of MreB

and associated enzymes around the rod width in *Bacillus subtilis*. *B. subtilis* contains 3 MreB paralogs (MreB, Mbl, and MreBH) that co-polymerize into mixed filaments and always colocalize *in vivo* (Defeu Soufo and Graumann 2006) (Defeu Soufo and Graumann 2010) (Dempwolff et al. 2011). Thus, we assume throughout that MreB and Mbl are interchangeable for fluorescent imaging.

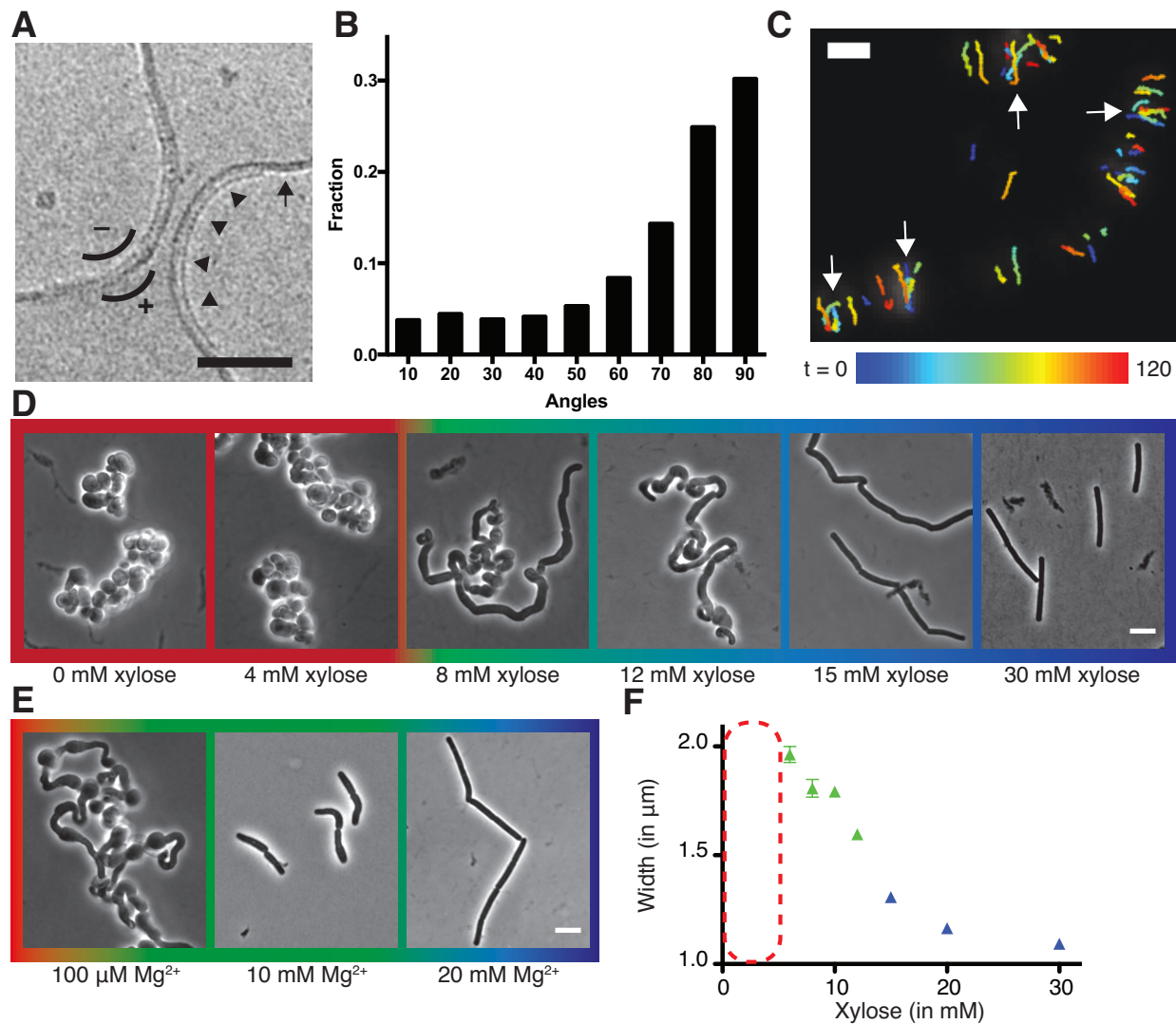


**Figure 2.1. Curved MreB filament motions do not follow an ordered template (A-C)**  
- **(A)** The negative curvature of MreB filaments (arrowheads) aligns with the negative principal curvature of the liposome surface (arrow). Scale bar is 50 nm. **(B)** Angular distribution of GFP-Mbl trajectories relative to the long axis of the cell indicates that while the distribution has a mode of 90°, it is broad (SD = 34°).

**Figure 2.1 (Continued).** **(C)** Particle tracking of Mbl-GFP during 100 seconds (1 rotation) indicates trajectories close in time frequently cross paths (white arrows). Scale bar is 1  $\mu\text{m}$ . Modulating teichoic acid levels titrates cell width and shape (D-F) - **(D)** Strains with *tagO* under inducible control display a teichoic acid-dependent decrease in width. **(E)** BEG300 at an intermediate level of *tagO* induction (15mM xylose) shows a  $\text{Mg}^{2+}$  dependent decrease in width. All scale bars are 5  $\mu\text{m}$ . See also Figure S1. **(F)** Plot of cell width as a function of *tagO* induction in LB supplemented with 20 mM  $\text{Mg}^{2+}$ , calculated from rod-shaped cells (error bars are Standard Error of the Mean (SEM)). Areas not plotted at lower xylose levels (red dashed rectangle) are regions where cells are round (no width axis). Color scheme for D-F: red indicates round cells (no width axis), blue indicates rods (measurable width axis), and green indicates intermediate regimes where both rods and round cells are observed.

## (ii) Maintenance of rod shape by MreB filaments

### Oriented MreB Motion Cannot Arise from an Ordered Cell Wall Template

The mechanism by which MreB filaments and associated PG synthases orient their motion around the rod circumference is not known. Each filament-synthase complex is disconnected from the others, moving independently of proximal neighbors (Garner et al. 2011). The organized, circumferential motion of these independent filament-synthase complexes could arise in 2 ways: 1) A templated organization, where cell wall synthetic complexes move along an existing pattern of ordered glycan strands in the cell wall as they insert new material into it (Höltje 1998), or 2) A template-independent organization, where each synthetic complex has an intrinsic mechanism that orients its motion and resultant PG synthesis around the rod circumference.

To explore the extent of order within the motions of the Rod complex, we analyzed the trajectories of GFP-Mbl filaments during the period of one axial revolution using total internal reflection fluorescence microscopy (TIRFM). We observed that filament

trajectories close in time (within the period of one revolution) frequently cross (Figure 2.1C, Movie S1), making it unlikely that MreB filaments move along a perfectly ordered template. Rather, the motions of filaments are overall oriented, but not perfectly aligned, a characteristic reflected by the broad distribution of angles that MreB (Figure 2.1B) and the other components of the Rod complex move relative to the long axis of the cell (Garner et al. 2011; Domínguez-Escobar et al. 2011). As MreB movement reflects the insertion of new glycan strands, these motions indicate that the sacculus is built from somewhat disorganized, yet predominantly circumferential strands, a conclusion in agreement with previous studies that assayed cell wall organization with cryo-electron microscopy (Gan et al., 2008), atomic force microscopy (Hayhurst et al. 2008), and X-ray diffraction (Balyuzi et al., 1972). Furthermore, preexisting cell wall is not necessary for the regeneration of rod shape from wall-less *B. subtilis* L-forms (Kawai, Mercier, and Errington 2014), indicating that both oriented MreB motion and rod shape can arise without an ordered template.

### **MreB Motions Become Isotropic in the Absence of Rod Shape**

As it appeared that organized MreB motion does not arise from patterns in the cell wall, we hypothesized there was an intrinsic mechanism orienting the motion of each filament-cell wall synthetic complex. To test this hypothesis, we examined MreB motions as we changed the shape of cells from rods to spheres. As the internal turgor pressure and stiffness of *B. subtilis* resists external mechanical perturbations to its shape (Renner et al., 2013), we first altered the shape of cells by controlling the level of wall

teichoic acids (WTAs), negatively charged cell wall polymers believed to increase the rigidity of the sacculus via their coordination of extracellular  $Mg^{2+}$  (Matias and Beveridge 2005) or modulation of hydrolase activity (Atilano et al., 2010). Knockouts in *tagO*, the first gene in the WTA synthesis pathway, create large, slow-growing, round cells that still synthesize PG, building extremely thick and irregular cell walls (D'Elia et al. 2006). Inhibition of WTA synthesis does not appear to alter the rate of PG incorporation in *B. subtilis* (Pooley et al., 1993) or cellular levels of lipid II in *S. aureus* (Atilano et al., 2010). We placed *tagO* under xylose-inducible control and grew cells at different induction levels. At high TagO inductions, cells displayed normal widths, as expected. As we reduced TagO levels, rods became gradually wider (Figure 2.1D,1F) until, beneath a given induction, cells were no longer able to maintain rod shape, growing as spheres (or clumps of spheres) with no identifiable long axis. At intermediate induction levels, we observed a transition region between the two states, with cells growing as steady state populations of interconnected rods and spheres (Figure 2.1D). In agreement with models that cell wall rigidity is conferred via WTA-mediated coordination of  $Mg^{2+}$  (Thomas and Rice 2014), both cell width and the amount of TagO induction determining the rod/sphere transition could be modulated by  $Mg^{2+}$  levels (Figure 2.1E, S1).

By tracking the motion of GFP-MreB filaments in these differing cell shapes, we found that motion is always oriented in rods, moving predominantly circumferentially at all induction levels above the rod/sphere transition. However, in round cells (those induced



beneath the rod/sphere transition point or in *tagO* knockouts) MreB filaments continued to move directionally, but their motions were isotropic, moving in all directions (Figure 2.2A, Movie S2A). To quantify the relative alignment of MreB under each condition, we calculated the angle between trajectory pairs less than 1  $\mu\text{m}$  apart (Figure 2.2B, S2A). This analysis revealed that MreB motions are more aligned when cells are rods: above the rod/sphere transition, trajectories have a median angle difference of  $26^\circ$ ; while at low TagO inductions, where cells are round, the angle difference increases to  $42^\circ$ , close to that of randomly oriented trajectories ( $45^\circ$ ).

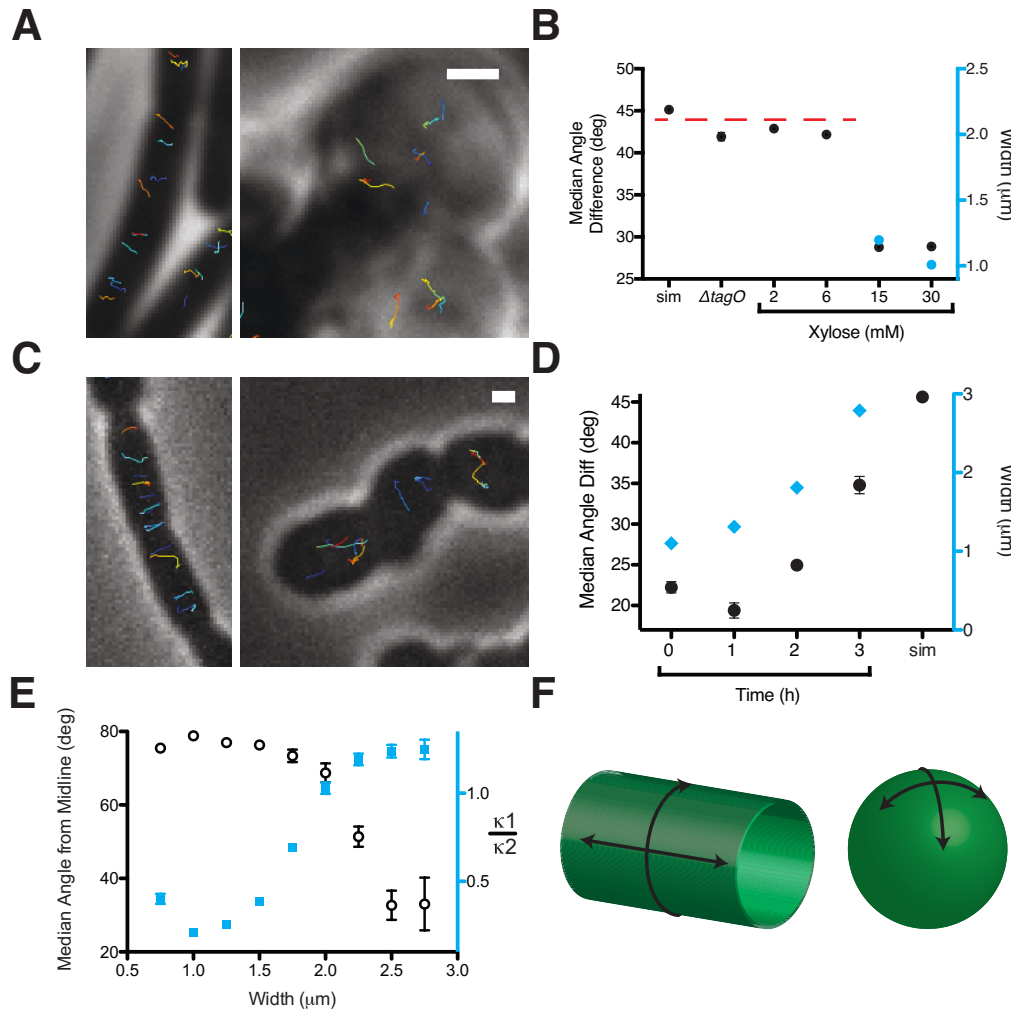


**Figure 2.2. Oriented MreB motion correlates with rod shape.**

**Figure 2.2 (Continued).** **(A)** BEG300 at maximum tagO induction (30 mM) is rod-shaped, and MreB tracks are largely oriented perpendicular to the midline of the cell (left).  $\Delta tagO$  cells show round morphologies with unaligned MreB motion (right). **(B)** Median inter-track angle difference for track pairs  $\leq 1 \mu\text{m}$  apart, plotted for BEG300 at several tagO induction levels,  $\Delta tagO$  cells, and a simulation of randomly oriented angles (sim). For spherical cells width is not measurable, indicated with a dashed red line. **(C)**  $\Delta pbpH$  cells with *pbpA* under IPTG control display aligned MreB motion when *pbpA* is fully induced and cells are rods (left), but display unaligned MreB motion as Pbp2a levels reduce and cells become round (right). **(D)** Median inter-track angle difference for track pairs  $1 \mu\text{m}$  apart during Pbp2a depletion with cell widths at each time point. **(E)** Median angle from the midline (white circles) calculated for all rod-shaped cells from experiments in 2A-D plotted as a function of cell width. MreB filament alignment falls off rapidly beyond  $2 \mu\text{m}$ , a point corresponding to where cells become round, as shown by the ratio of principal curvatures (blue squares) approaching 1. See Figure S2E for further explanation. **(F)** Schematic showing the difference between the 2D surface curvature profile of rods and spheres. On the inside surface of spheres, all points have negative, yet equal values for both principal curvatures. In rods, however, one principal curvature is negative (the radius), while the other is 0 (the flat axis along the rod). All scale bars are  $1 \mu\text{m}$ . All error bars are SEM. See also Figure S2.

To verify that the loss of oriented MreB motion was due to the changes in cell shape, and not from some other effect of reduced WTA levels, we created round cells by alternate means. Depletion of both elongation PG transpeptidases (Pbp2a and PbpH) causes rod-shaped cells to become wider over time as they convert to spheres (Garner et al. 2011). We used this gradual transition of rods into spheres to examine both the width and overall shape dependence of MreB motion. At initial points of depletion (1 - 2 hours) the rods widened but maintained circumferential MreB motion. At 2.5 hours of PbpA depletion, cells were a mix of spheres and rods of differing widths. These cells displayed the same pattern of MreB orientation observed above: round cells contained unoriented MreB, while nearby rod shaped cells showed circumferential motion (Figure 2.2C, Movie S2B). Quantitation of trajectories from all cells (both rods and spheres) at

each time point of depletion indicated an increase in the median angle between trajectories as the population grew wider and rounder over time (Figure 2.2D, S2D).

In *E. coli*, the angle of mutant MreB filaments relative to the long axis has been reported to increase with cell width (Ouzounov et al. 2016). To test if the angle of MreB movement changes with respect to cell width in *B. subtilis*, we calculated the angle of each trajectory to the long axis for all cells in our data with an identifiable width axis. At the same time, we also measured the curvature of each cell to determine how the overall shape of the cell affected the orientation of motion (Figure S2E). This revealed that MreB motion in rods remained equivalently oriented over a wide range of rod widths, up to  $\sim 2 \mu\text{m}$  (Figure 2.2E, S2B, S2C). Beyond this width, cells began to lose their rod shape as they became more spherical, and the predominantly circumferential orientation of MreB motion was lost (Figure 2.2E, S2E). This suggested that oriented MreB motion does not sense or rely on a specific cell radius; rather the orientation relies on differences between the two principal curvatures of the membrane. It appears that the motion of MreB filaments is oriented along the direction of greatest principal curvature: In rods, there is zero curvature along the rod length, and high curvature around the rod circumference, along which filaments orient. In contrast, in round cells where MreB motion is isotropic, the two principal curvatures are equal (Figure 2.2F).

## **MreB Aligns Within Round Cells and Protoplasts Forced into Rod Shape**

To further verify that MreB filaments orient in response to overall cell shape, we externally imposed rod shape on cells with unoriented MreB motion. We loaded TagO-induced cells into long  $1.5 \times 1.5 \mu\text{m}$  microfluidic chambers, then reduced TagO expression to levels insufficient to produce rods in liquid culture (Figure 2.3A, S3A). After TagO depletion, cells expanded to fill the chamber indicating that WTA-depletion caused shape changes just as in bulk culture (Figure 2.3A, S3A). Within these chambers, cells grew as rods, but at a wider width ( $1.5 \mu\text{m}$ ) than wild-type cells, set by the chamber. When cells grew out of the chamber they swelled just as in bulk culture, showing confinement was required for rod shape at this induction level (Figure 2.3B, S3A). In the TagO-depleted cells confined into rod shapes, MreB moved circumferentially (Figure 2.3C, Movie S3) with an angular distribution similar to that of wild-type cells ( $90^\circ$ ,  $\text{SD} = 36^\circ$ ) (Figure 2.3F(i)), confirming that MreB orients in response to the cells having rod shape. This experiment demonstrates that the isotropic MreB motion observed in round cells arises from the lack of rod shape, and not from some other effect of our genetic perturbations. This experiment also showed another unexpected result: the doubling time of free (unconstrained) cells induced at similar TagO levels is slow ( $53 \pm 10 \text{ min}$ ), but confining them into rod shape restored their doubling time ( $44 \pm 4 \text{ min}$ ) toward wild-type rates ( $39 \pm 9 \text{ min}$ ) (Figure S3C).

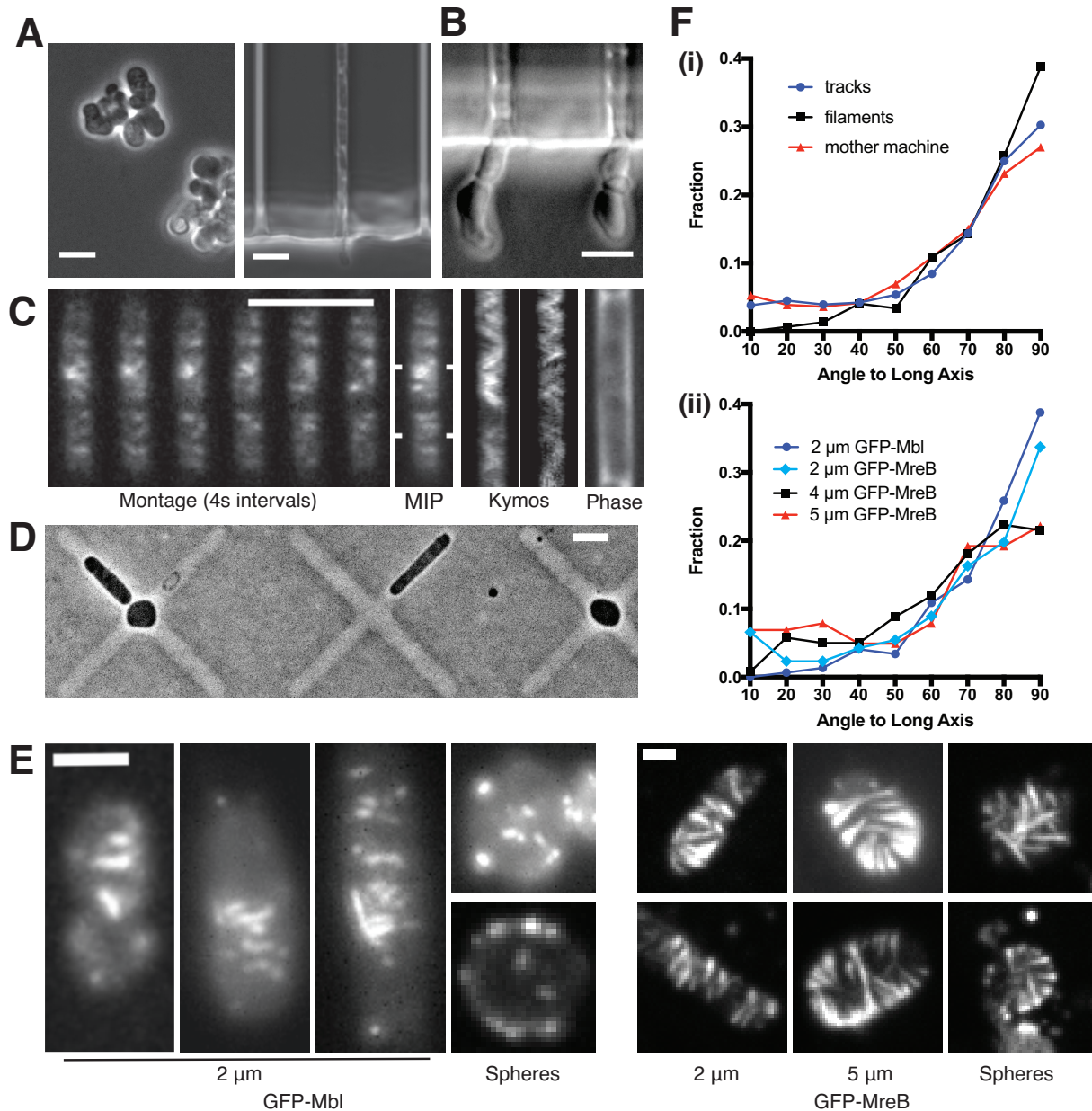


**Figure 2.3. MreB filaments align when rod shape is induced by external confinement.** (A) Phase contrast images of BEG300 grown in LB supplemented with 2 mM xylose and 20 mM  $Mg^{2+}$  in bulk culture (left) or confined into microfluidic channels of  $\sim 1.5 \mu\text{m}$  width (right). (B) Confined cells induced at 3 mM xylose in 20 mM  $Mg^{2+}$  progressively swell upon escaping confinement into free culture. See also Figure S3A. (C) (Left) Montage of MreB filaments moving across a confined cell. (Right) Maximal intensity projection of montage, kymographs of marked points and a phase contrast image of the cell. Scale bars for a-c = 5  $\mu\text{m}$ . (D) Phase contrast images of protoplasts contained in agar crosses. Cells in the center grow to be round while cells in arms grow as elongated rods. (E) (left) Short GFP-Mbl filaments orient circumferentially in rod-shaped protoplasts (2  $\mu\text{m}$ ) but lack orientation in round protoplasts (spheres).

**Figure 2.3 (Continued).** (right) Long GFP MreB filaments orient in rod-shaped protoplasts (2  $\mu\text{m}$ ); GFP-MreB filaments are still oriented in wider rod-shaped protoplasts (5  $\mu\text{m}$ ), but not to the same extent. In round protoplasts, GFP-MreB filaments are unoriented (spheres). See also Figure S3B. Scale bar is 2  $\mu\text{m}$ . **(F)** (i) The angular distribution of filaments within protoplasts is peaked at  $90^\circ$  (SD  $25^\circ$ ,  $n=147$ ), similar to that of MreB motion in TagO-depleted, confined cells ( $90^\circ$ , SD  $36^\circ$ ,  $n=359$ ) and MreB motion in wild-type cells ( $88^\circ$ , SD  $34^\circ$ ,  $n=1041$ ). (ii) In channels of varying widths (2, 4 and 5  $\mu\text{m}$ ), the orientation of GFP-MreB filaments remains circumferential but the angular distribution becomes wider at increasing channel width ( $93^\circ$ , SD  $34^\circ$ ,  $n=258$  at 2  $\mu\text{m}$ ), ( $81^\circ$ , SD  $35^\circ$ ,  $n=260$  at 4  $\mu\text{m}$ ) and ( $86^\circ$ , SD  $41^\circ$ ,  $n=203$  at 5  $\mu\text{m}$ ).

Next, we attempted to decouple MreB filament orientation from both A) the directional motion of filaments, and B) any structure within the cell wall. To accomplish this, we examined filament orientation in protoplasts (cells without cell wall) that we confined into different shapes, using highly expressed GFP-MreB to assay long filaments, and GFP-Mbl to assay short filaments. We protoplasted cells in osmotically stabilized media (Wyrick and Rogers 1973), then grew them under agar pads containing micro-patterned cross shapes. Cells in the center of these crosses ( $\sim 5$   $\mu\text{m}$  diameter) were forced to grow as spheres, whereas cells in the arms were constrained to grow into rods of various widths ranging from 2-5  $\mu\text{m}$ . (Figure 2.3D). Cells growing in these molds did not produce cell wall, as determined by WGA staining (Figure S3B). As reported previously (Domínguez-Escobar et al. 2011), MreB filaments within protoplasts did not move directionally (Movie S4), likely because the cell wall provides the fixed surface across which the PG synthesis enzymes move. Within the protoplasts confined into the smallest rod shapes (2  $\mu\text{m}$ ), filaments oriented at a distribution of angles predominantly perpendicular to the cell length (Figure 2.3E-F). The angular distributions of short GFP-Mbl filaments and longer GFP-MreB filaments were similar to each other ( $94^\circ \pm 25$  and

93° ± 34 respectively), and also similar to the distribution of filament trajectories observed in intact, wild-type cells (88°, SD = 34°). As we increased the width of the imposed rod shape from 2 to 5 μm, filaments remained predominantly oriented in all cases, but the distribution of alignment became increasingly broad (86°, SD = 41° at 5 μm). In contrast to confinement in rods, both short and long filaments in spherically confined protoplasts remained unoriented (Figure 2.3E). Together, these data demonstrate that MreB filaments orient to point around the rod width even in the absence of cell wall or directional motion, as long as the cell has a rod shape. These experiments also demonstrate that MreB filaments will align even in wider rods, where the difference in principal curvatures is smaller than in wild-type cells, but that, as the difference in principal curvatures decreases, filament alignment becomes more disordered.

### **MreB Filaments Orient Around Liposome Tubes *in vitro***

To test if MreB filaments are themselves sufficient to align along the predominant direction of membrane curvature, we assembled purified *T. maritima* MreB within liposomes and visualized it using electron cryo-electron microscopy and tomography. While controlling the final concentration of protein encapsulated within liposomes ≤ 1 μm is difficult, we were able to assemble MreB inside liposomes at high concentrations. At these concentrations, MreB filaments tubulated liposomes, creating rod-like shapes (Figure 2.4A-B, S4, Movie S5 first and second part). In tubulated regions, MreB filaments could be traced around the circumference of the liposome tube, while

filaments in spherical regions were found in all possible orientations (Figure 2.4A). At the highest concentrations, tubulated liposomes contained closely packed filament bundles, allowing us to observe a regular patterning of the canonical double filaments of MreB (Figure 2.4C). As it is unknown if membrane-associated MreB filaments exist *in vivo* as isolated double filaments or as bundles, we examined how filaments align when bundling is reduced by purifying MreB containing a point mutation (*T. maritima* MreB V109E) that decreases inter-protofilament interactions (van den Ent, Izoré, et al. 2014). This mutant assembled into shorter filaments that did not encircle the liposome width, yet still oriented predominantly along the short axis (Figure 2.4B, S4B, Movie S5). Purified wild-type MreB did not bind to the outside surface of small liposomes contained within larger ones (Figure 2.4A), indicating that MreB filaments preferentially polymerize on inward (negative) curvatures, akin to the inner leaflet of the bacterial membrane. Liposomes are spherical, with no deformations, in the absence of MreB (Figure S4D).



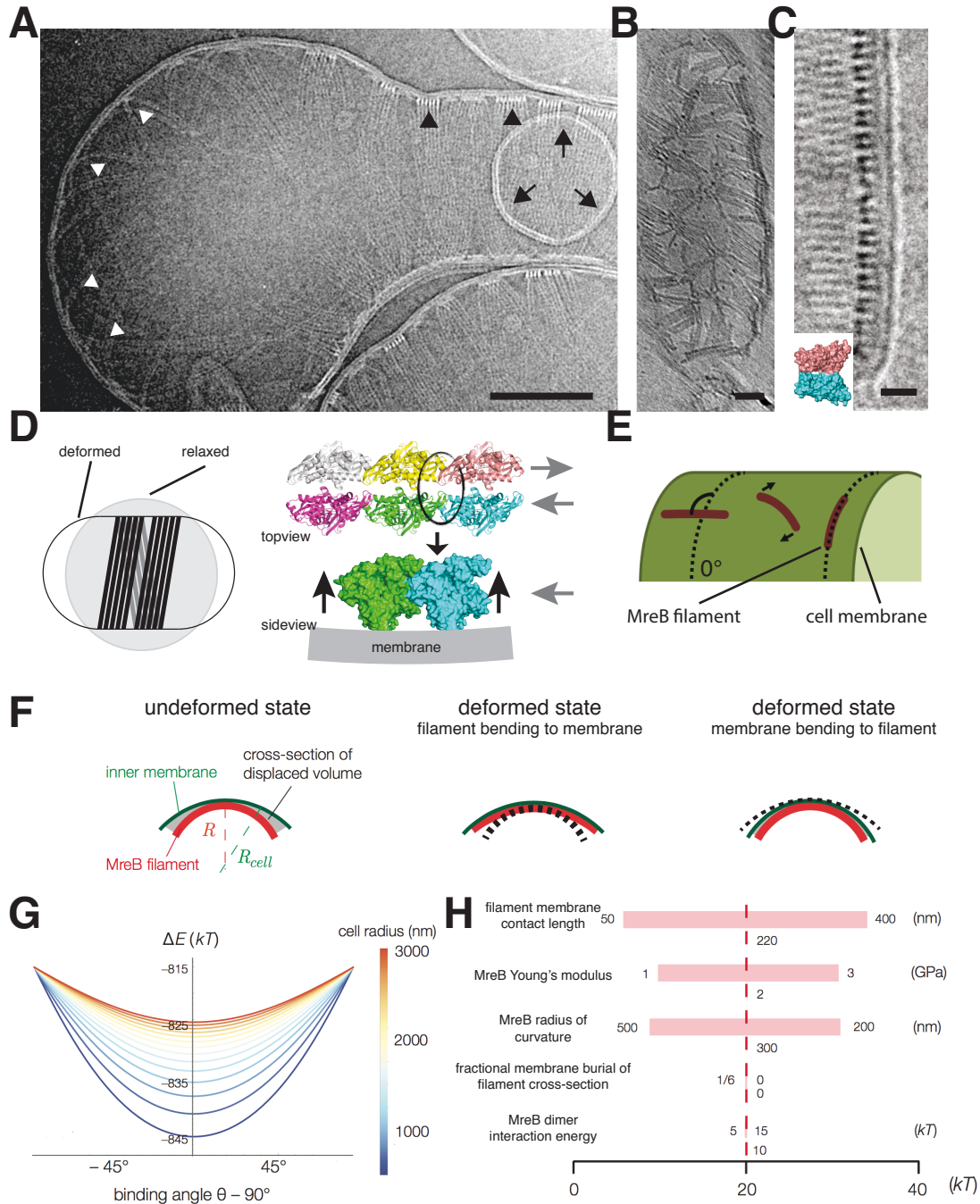


**Figure 2.4** *T. maritima* MreB filaments assembled in liposomes align perpendicular to the rod axis. **(A)** Black arrowheads show aligned bundles of filaments in a tubulated liposome, white arrowheads show unaligned bundles in a spherical region of the same liposome. Arrows show a positively curved surface inside the liposome, to which no MreB filaments bind. Scale bar is 100 nm. See also Figure S4.

**Figure 2.4 (Continued).** **(B)** *T. maritima* MreB (V109E) (Bs: V114), mutated in a residue in the inter-protofilament interface, assembled as in A. Due to lack of turgor pressure, local inward bending of liposomes by MreB filaments makes the angular distribution noisier but the general trend toward circumferential binding remains. Scale bar is 50 nm. Corresponding movie: SM5, third part. Corresponding quantification: Figure S4B **(C)** MreB in liposomes adopts a double stranded antiparallel protofilament arrangement consistent with (van den Ent et al., 2014). Scale bar is 50 nm. **(D)** (left) Schematic drawing depicting the cause of the shape change from spherical to rod-shaped liposomes: MreB wants to attain greater curvature and since there are many filaments, they are laterally stabilized. As the liposome is much more easily deformable than cells, the resulting energy minimum is a deformed liposome with an MreB helix on the inside. (right) Model showing why the unusual architecture of MreB filaments might have been selected during evolution: its juxtaposed subunits in the two antiparallel protofilaments produce putative hinges that could be the region of bending for these filaments. Canonical F-actin filament architectures, with staggered subunits, would need bending within the subunits, which is less easily achieved. **Modeling of MreB – membrane interactions and filament orientation.** **(E, F)** Hydrophobic residues are located on the outer edge of the antiparallel MreB double filament, which is here modeled as an elastic cylindrical rod. To achieve maximum hydrophobic burial, membrane deformation, MreB bending, or a combination of the two may occur. **(G)** A plot of the change in total energy ( $\Delta E$ ) caused by the MreB-membrane interaction against the binding angle  $\theta$  for various cell radii shown in the color scheme on the right. Note that  $\Delta E$  is minimal at  $\theta=90^\circ$ , which agrees with the observed orientation of MreB binding and motion. At larger rod radii, the energetic well becomes flatter and MreB binding becomes more susceptible to thermal fluctuations and other sources of stochasticity, which would result in a broader angular distribution of filaments. **(H)** A sensitivity analysis of the model over a range of model parameters.

### **Biophysical Modeling Suggests Highly Bent MreB Filaments Orient Along the Greatest Principal Curvature to Maximize Membrane Interactions, a Prediction Insensitive to Large Variations in Parameters**

The above observations demonstrate that MreB filaments sense and align along the direction of greatest principal curvature, i.e., the more curved inner surface of the rod circumference. The ultrastructure of MreB filaments provides a possible mechanism:

MreB filaments are bent (Salje et al. 2011), with the membrane-interacting surface on the outer face of the bend (Figure 2.4D). This bent conformation could cause filaments to preferentially orient along the curved rod circumference, rather than the flat rod length, to maximize the burial of hydrophobic moieties into the membrane, a mechanism suggested by previous theory (S. Wang and Wingreen 2013).

As the curvature of MreB filaments bound to liposomes is much greater (~200 nm diameter) than that of *B. subtilis* cells (~900 nm diameter), we performed analytical calculations to model how highly curved MreB filaments would align within a cell with a less curved surface (Figure 2.4E-G, Supplemental Text 1). As many of the biochemical and physical parameters of MreB are still unknown, we first assumed a fixed set of parameters, and later verified that our results were robust over a large parameter range. We initially assumed a membrane interaction energy of 10 kT per monomer (calculated from residues involved in membrane associations (Salje et al. 2011)), and a similar Young's modulus to actin (2 GPa). We modeled filaments as elastic beams made of two protofilaments. In addition, we used the Helfrich free energy to model the energetics of membrane deformation, and accounted for the work done against turgor pressure due to changes in volume (Supplemental Text 1). These calculations indicate that the total energy is minimized when filaments orient along the direction of maximal curvature (Figure 2.4G) and that, importantly, the energy penalty for incorrectly-oriented filaments is much greater than the energy of thermal fluctuations. Interestingly, this modeling indicates a decrease in energetic preference for the preferred filament orientation as the

radius of the cell is increased (Figure 2.4G), a prediction in qualitative agreement with our observations of alignment in protoplasts. Furthermore, our calculations indicate that orientation is robust over a large, biologically relevant range of parameters, including the membrane binding energy, filament length, and filament Young's modulus (Figure 2.4H).

These calculations predict that filaments should orient circumferentially both if the membrane deforms to the filament (at low turgor pressures or if filaments are stiff) (Salje et al. 2011), or if filaments deform to the membrane (at high turgor pressures or if filaments are flexible) (Figure 2.4F). Our experimental data demonstrates MreB filament alignment across a range of pressures: high within cells, low to none within liposomes, and a pressure between the two within osmotically-stabilized protoplasts. In the absence of turgor pressure, MreB filaments deform liposomes since it is energetically more favorable to bend the membranes than to bend the filaments, as observed in our *in vitro* data (Figure 2.4A-B, S4). However, in live cells, our modeling predicts that MreB filaments cannot deform the inner membrane due to the large turgor pressure, and instead deform to match the greatest principal membrane curvature. Hence filaments create curvature in liposomes and sense it in cells.

### (iii) *De novo* creation of rod shape by MreB filaments

#### **Rod-Shape is Lost in a Global Manner, but Reforms Locally**

Together, the above data demonstrate that MreB filaments are sufficient to preferentially orient along the direction of greatest principal membrane curvature. In rod-shaped cells, this direction is along the rod circumference. As filaments move along their length, their orientation constrains the spatial activity of the PG synthetic enzymes such that new cell wall is inserted in a mostly circumferential direction (Hayhurst et al. 2008) to reinforce rod shape (Yao et al. 1999; Chang and Huang 2014). While the ability of MreB filaments to orient in pre-existing rods can help explain how rod shape is maintained, we also wanted to understand how MreB filaments facilitate the *de novo* formation of rod shape. To explore this, we observed how cells interconvert between spheres and rods.

We first examined how rod shape fails, by growing our TagO-inducible strain at induction levels that produced rods and then reducing the  $Mg^{2+}$  concentration to induce them to convert to spheres. This transition revealed that rods convert into round cells by irreversibly swelling: once a rod begins to widen, it continues to do so until reaching a fully spherical state with no reversion during the process (Figure 2.5A). Similar rod to sphere transitions could be attained by holding  $Mg^{2+}$  constant while reducing TagO expression. Likewise, cells grown at intermediate TagO induction levels (8-12mM) grew as steady state populations of interconnected rods and spheres, indicating that cells underwent repeated cycles of rod shape formation followed by reversion to spheres

(Figure 2.1D, E). These results indicate that rod shape can be maintained only as long as the cell wall is sufficiently rigid to resist the internal turgor pressure.

We next examined how rod shape forms from round cells. As the recovery of protoplasted *B. subtilis* is so infrequent that it has never been directly visualized (Mercier et al., 2013), we assayed how round cells with preexisting cell walls convert back into rods, using three systems: 1) re-inducing WTA expression within TagO-depleted, spherical cells, 2) holding TagO expression beneath the rod/sphere transition and increasing  $Mg^{2+}$  levels, and 3) re-inducing Pbp2a expression in spherical, Pbp2a-depleted cells. In all three cases, rods reformed in a discrete, local manner; spheres did not form into rods by progressively shrinking along one axis, but rather, rods abruptly emerged from one point on the cell, growing more rapidly than the parent sphere (Figure 2.5B, Movie S6, Movie S8). This morphology is similar to the initial outgrowth of germinating *B. subtilis* spores (Pandey et al. 2013). We occasionally observed another mode of recovery, occurring when round cells were constrained, or divided into, ovoid or near-rod shapes. Once these near-rod shaped cells formed, they immediately began rapid, rod-like elongation along their long axis (Figure S5D).

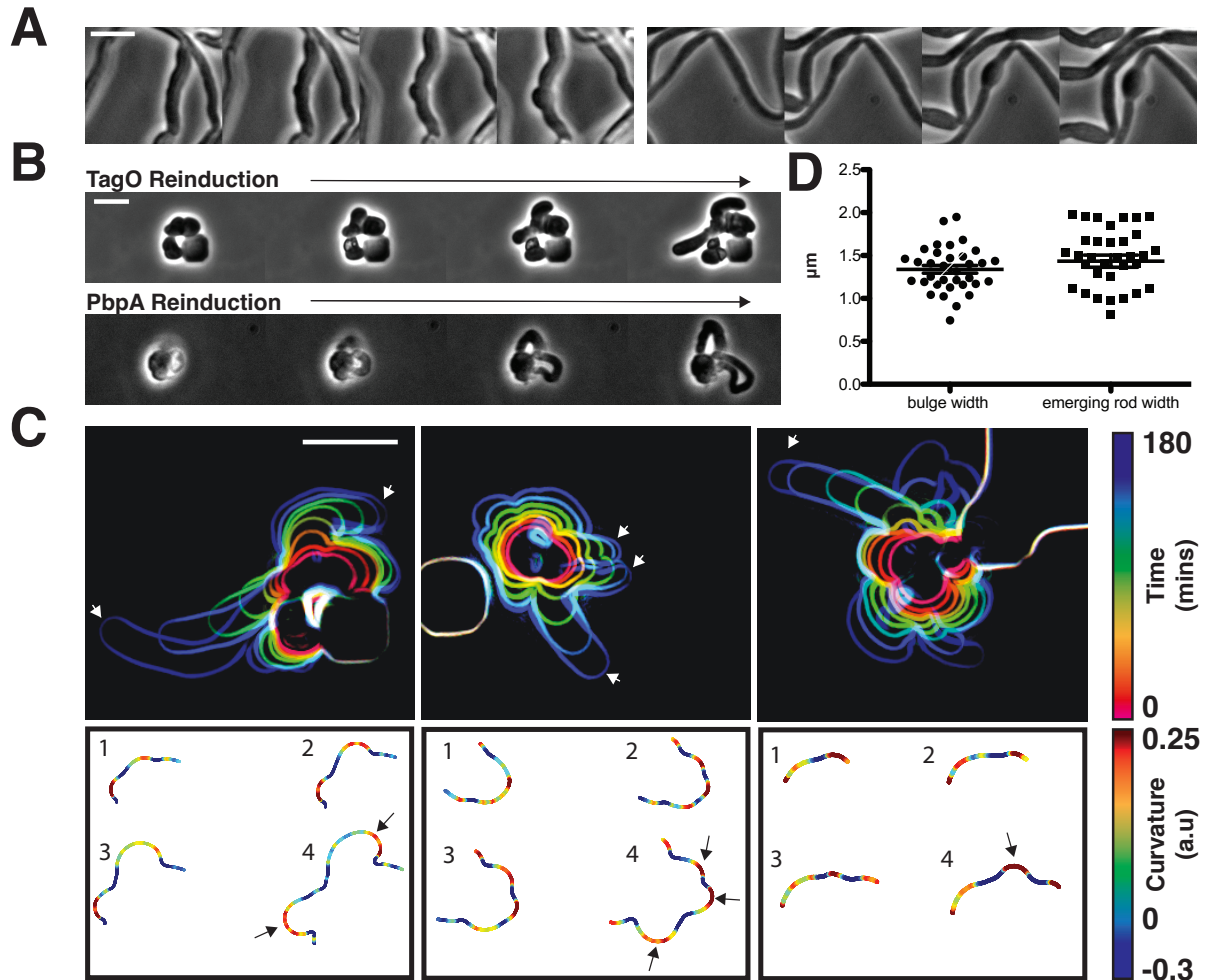


**Figure 2.5. Sphere to rod transitions occur locally and lead to faster growth. (A)** Loss of rod shape proceeds continuously and without reversals, as shown by BEG300 cells grown in 12 mM xylose, shifted from 1mM  $\text{Mg}^{2+}$  to 100  $\mu\text{M}$   $\text{Mg}^{2+}$  on a pad. Frames are 5 min apart. **(B)** Increases in expression of *tagO* or *pbpA* from depleted spherical cells causes cells to emit rapidly elongating rods from discrete points. (Top) BEG300 cells in 20 mM  $\text{Mg}^{2+}$  were grown in 0 mM xylose for 4h, then transferred to a microfluidic chamber and grown in 0 mM xylose and 20 mM  $\text{Mg}^{2+}$  for 1h. Following this, *tagO* expression was induced with 30 mM xylose at the first frame. (Bottom) BRB785 cells in 20 mM  $\text{Mg}^{2+}$  were depleted of Pbp2a by growth in 0 mM IPTG for 4h. At the start of the frames, they were transferred to an agar pad containing 1mM IPTG to induce *pbpA* expression. Frames are 30 min apart. **(C)** Plots of cell contours as cells recover from TagO depletion: (top) cell outlines are colored in time red to blue (0-180min). White arrows indicate emerging rods; (bottom) heat maps of curvature show that rods emerge from small outward bulges (red) flanked by inward curvatures (blue). Black arrows indicate points where emerging rods form.

**Figure 2.5 (Continued).** (D) The width of initial bulges and the rods that emerge from them are highly similar, indicating the initial deformations may set the starting width of the rods. Error bars are SEM. All scale bars are 5  $\mu\text{m}$ .

## **Rods Form from Local Outward Bulges and Grow Faster than Non-Rod Shaped Cells**

We focused on two salient features of the rod shape recoveries: 1) rod shape forms locally, most often at one point on the cell surface, and 2) once a rod-like region is formed, it appears self-reinforcing, both propagating rod shape and growing faster than adjacent or attached non-rod shaped cells.

We first wanted to understand how rod shape initiates *de novo* from spherical cell surfaces. By examining the initial time points of recoveries, we found that rods begin as small outward bulges: local regions of outward (positive Gaussian) curvature flanked by regions of inward (negative Gaussian) curvature (Figure 2.5C). These initial outward bulges showed a width distribution similar to that of the later emerging rods (Figure 2.5D). Once these bulges formed, they immediately began rapid elongation into nascent rods, which would then thin down to wild type width over time. Bulge formation and rod recovery were independent of cell division, as cells depleted of FtsZ still recovered rod shape (Figure S5E). Rather, these bulges appeared to arise randomly, evidenced by the fact that different cells produced rods at different times during WTA or Pbp2a repletion. We conclude that the appearance of a local outward bulge can act as the nucleating event of rod shape formation.



As emerging rods appeared to grow faster than adjacent round cells, we tested if the doubling times of rod-shaped cells were faster than those of non-rods by measuring the doubling times in our inducible TagO strain at different induction levels using both OD<sub>600</sub> measurements and single cell microscopy under steady state conditions (Figure 2.6B, S3C). This revealed a sharp transition in doubling time that matched the conditions of the rod/sphere transition: growth is slow when cells are spheres, yet greatly increases when cells are rods (Figure S3C, S5A). Furthermore, the doubling times of recovering rods was similar to that of rods at steady state (Figure S3C).

We believe the slower doubling time of rods is likely due to cell shape and not another effect, such as the lack of WTAs, as 1) the doubling time of TagO-depleted cells confined in the microfluidic chambers matched that of wild type cells; and 2) both the doubling times and the boundary of the rod/sphere transition could be equivalently shifted by changing the Mg<sup>2+</sup> concentration (Figure 2.1E, S1, S5A). Combined, these results indicate that rod shape creates local, self-reinforcing regions that are poised for more rapid growth; once any small region of the cell approximates a rod shape, growth of the rod-like region is amplified, growing faster than other regions, and thereby outcompeting non-rod growth at the population level.

## **Rod-shape Formation Correlates with Aligned MreB Motion and Increased Glycan Crosslinking**

We next sought to determine what features distinguished the rods from round cells. As the elongation of rod-shaped cells requires a sufficiently rigid cell wall (Figure 2.1D-E, 5A), the self-reinforcing growth of rods could arise from a few mutually compatible sources relative to round cells: 1) The arrangement of PG strands could be such to reinforce the rod (Amir and Nelson, 2012; Chang and Huang, 2014), 2) WTAs could be preferentially incorporated into rods, or 3) The extent of crosslinking of newly inserted material in the cell wall could be increased so as to make it more rigid (Loskill et al., 2014).

To assay the orientation of newly inserted cell wall, we imaged the motions of MreB as we induced TagO-depleted cells to recover into rods. This revealed that oriented MreB motion correlates with local shape: emerging rods displayed oriented MreB motion even at the initial points of their formation, while attached round parent cells displayed unaligned motion (Figure 2.6A, Movie S7). This demonstrates that oriented MreB motion correlates with local geometry and does not arise from a global, cell spanning change. We next examined the overall cellular distribution of MreB in recovering cells with confocal microscopy. This revealed that, immediately prior to rod emergence, MreB transiently accumulated in a bright ring oriented perpendicular to the direction of rod emergence, most often occurring at the interface of the bulge and the round cells (Figure 2.6C, S5F).

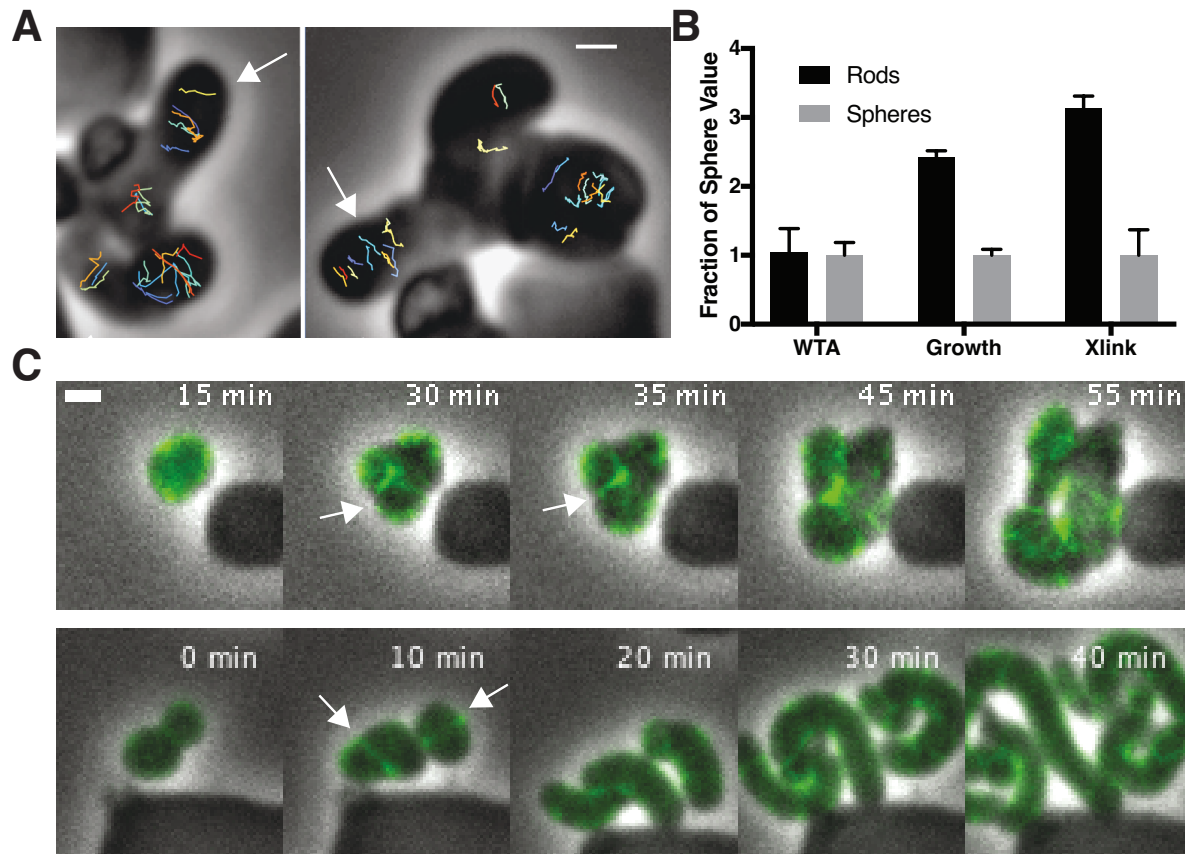


**Figure 2.6. Cell wall synthesis and growth are coupled by MreB-guided creation of the rod shape.** (A) (left) GFP-MreB trajectories during a sphere to rod transition. Emerging rods exhibit oriented MreB motion (white arrows) while attached round cells have unoriented motion. Scale bar is 1  $\mu$ m. (B) (B) Fold change in the teichoic acid incorporation, doubling times (assayed by OD<sub>600</sub> measurements), and % crosslinked muropeptides of rods (inducible TagO with 30mM xylose in LB with 20 mM Mg<sup>2+</sup>) compared to spheres (grown in LB with 20 mM Mg<sup>2+</sup>). Error bars are SD. See also Figure S3C, S5B-C, S6. (C) During shape recoveries, immediately before rod emergence, MreB transiently accumulates in a bright ring where the bulge connects to the parent sphere. See also Figure S5F. Scale bar is 2  $\mu$ m.

The local reinforcement of rod shape in recovering cells could arise from preferential incorporation of the cell wall rigidifying WTAs, as the WTA ligases have been reported to interact with MreB (Kawai et al. 2011). Thus, we tested if rod shape and oriented MreB motion correlated with increased WTA accumulation in emerging rods. To test

this, we labeled recovering cells with fluorescently labeled lectins that specifically bind to WTAs (Figure S6A). Following TagO re-induction, WTAs in recovering cells had a disperse, diffuse distribution around the cell (Figure S6B), equally present in the cell walls of both rods and spheres (Figure 2.6B). To test if the WTA ligases move with MreB, we created fluorescent fusions to these proteins at their native locus and examined their dynamics with TIRFM. We were unable to observe any of the circumferential motions expected if the WTA ligases localized to or moved with MreB; instead they appeared to be rapidly diffusing along the membrane (Figure S6C, Movie S9, Supplementary Text 2).

Next, we used mucopeptide analysis to examine if there was a difference in the amount of glycan crosslinking between rods and spheres. This revealed that the PG surrounding spheres was significantly less crosslinked than rods (Figure 2.6B, S6D). Thus, while spheres appear to synthesize more amounts of PG, the cell wall in rods is more crosslinked, and thus presumably more load bearing (Loskill et al., 2014). This result fits with the finding that WTA-depleted cell walls are thicker and more irregular (D'Elia et al., 2006), as studies of plant cell walls have shown that decreased crosslinking makes the cell wall more permeable to water, resulting in swollen, less rigid cell walls (Redgwell et al., 1997)(Ishii et al., 2001).

Previous studies have shown that the rate of PG incorporation (Pooley et al., 1993) and the amount of PG (Elbaz and Ben-Yehuda 2010) in *B. subtilis* is unchanged when the

WTA pathway is inactivated. To observe whether both spheres and rods inserted new PG during the process of rod shape recovery in our assay, we used fluorescent D-amino-acids (FDAAs), which crosslink into newly inserted cell wall. We grew TagO-depleted cells in a microfluidic device in the presence of HADA, then switched the media to contain Cy3B-ADA as we re-induced TagO expression. During rod emergence, the old cell wall signal (HADA) remained in the sphere, while the emerging rod was almost entirely composed of new (Cy3B-ADA) material, confirming the discrete nature of rod shape recovery. However, the attached spheres also incorporated Cy3B-ADA, indicating PG synthesis occurs in both rods and spheres during recovery (Figure S5C).

In summary, these data give new insights into what properties of the cell wall can be modulated to create and stabilize rod shape: rod shape is not formed by preferential localization of teichoic acids to rods, and both spheres and rods incorporate PG before and during rod shape recovery, in line with reports that PG incorporation (Pooley et al., 1993) and amount (Elbaz and Ben-Yehuda 2010) is unchanged by the inhibition of WTA synthesis. Rather, the only two differences between rod shaped and round cells we observed were 1) oriented motion of MreB in rods, coupled with 2) an increased crosslinking of the inserted glycans. Thus, it appears that not only does MreB direct glycan insertion into circumferential hoops, but also these strands are more crosslinked, and both properties would be expected to increase the strength of the cell wall. It may be that these two attributes are mechanistically linked, and a more oriented

arrangement of glycan strands might provide a more optimal arrangement of peptides for crosslinking reactions. We note that as PG and WTA precursors share a common lipid carrier and WTAs affect PG hydrolase activity (Kasahara et al., 2016) and crosslinking, their depletion may cause other rod-shape inhibiting PG abnormalities that we cannot observe.

#### (iv) Discussion and conclusion

The above experiments give new insights into the mechanism by which MreB builds rod shape. First, the curved ultrastructure of MreB filaments causes them to orient and move along the direction of greatest membrane curvature, inserting material in that direction. Second, both the formation and propagation of rod shape occurs by a local, self-reinforcing process: once a local region of rod shape forms, it propagates more rod shape. Finally, as far as we can determine, the primary differences between the growth of rods and non-rods is the circumferential orientation of MreB motion and increased glycan crosslinking.

Combined, these findings indicate that MreB filaments function as curvature-sensing rudders, a property that allows them to organize cell wall synthesis so that it builds rod shape: MreB filaments orient along the greatest membrane principal curvature, thereby constraining the activity of the associated PG synthases so that, as they move via their synthetic activity, they deposit highly crosslinked glycans oriented in the direction of that curvature, and this arrangement of insertion reinforces rod shape. Even during the initial

stages of rod shape formation, oriented MreB motion and rod shape always coincide, and the intrinsic curvature of MreB filaments suggests these properties cannot be uncoupled. This coupling appears to be an essential component of the Rod system: by linking filaments that orient along the greatest principal curvature to cell wall synthetic enzymes reinforcing that curvature, the Rod complex creates a local, self-organizing system that allows bacteria to both maintain rod shape and also establish rod shape *de novo*.

In established rods, we propose that MreB maintains and propagates rod shape via feedback between existing shape, filament orientation, and subsequent shape-reinforcing PG synthesis. As rod-shaped cells grow (Figure 2.7A1), MreB filaments orient along the more curved axis around the bacterial width (Figure 2.7A2). Because MreB filaments always translocate along their length (Olshausen et al. 2013), filament orientation constrains the activity of the associated PG synthases such that new cell wall is inserted in bands predominantly oriented around the width of the rod (Figure 2.7A3). This circumferential insertion of glycan strands, combined with a high level of crosslinking between them, yields a highly connected, anisotropic arrangement of material that reinforces rod shape (Figure 2.7A1), which allows continued MreB filament orientation. This feedback loop can continue as long as the material within the rod sidewalls is sufficiently rigid to withstand the stresses arising from the internal turgor pressure, allowing the rod shape to be robust once it is formed.

The coupling between the local sensing and reinforcement of differences in principal curvature could also allow the *de novo* formation of rod shape. In round cells, there is no difference in principal curvatures (Figure 2.7B1), so MreB motion is isotropic. Rods do not form by squeezing these round cells across one axis, rather we observe them forming by the amplification of local rod-like regions. Given the rapid timescale of our recoveries, the Rod system appears poised to propagate any shape variations that create curved regions favorable to oriented MreB motion. Once regions of oriented motion are established, they self-propagate and elongate, creating a new rod shape and thus continued oriented MreB motion. The most common shape variation we observe preceding rod emergence is small outward bulges flanked by regions of inward curvature (Figure 2.5C). It remains to be determined how these initial bulges form and what cellular factors are involved in this process. They could arise from local changes in cell wall stiffness: a local softening of the cell wall has been observed to induce the rod shaped outgrowth of germinating fission yeast spores (Bonazzi et al., 2014).



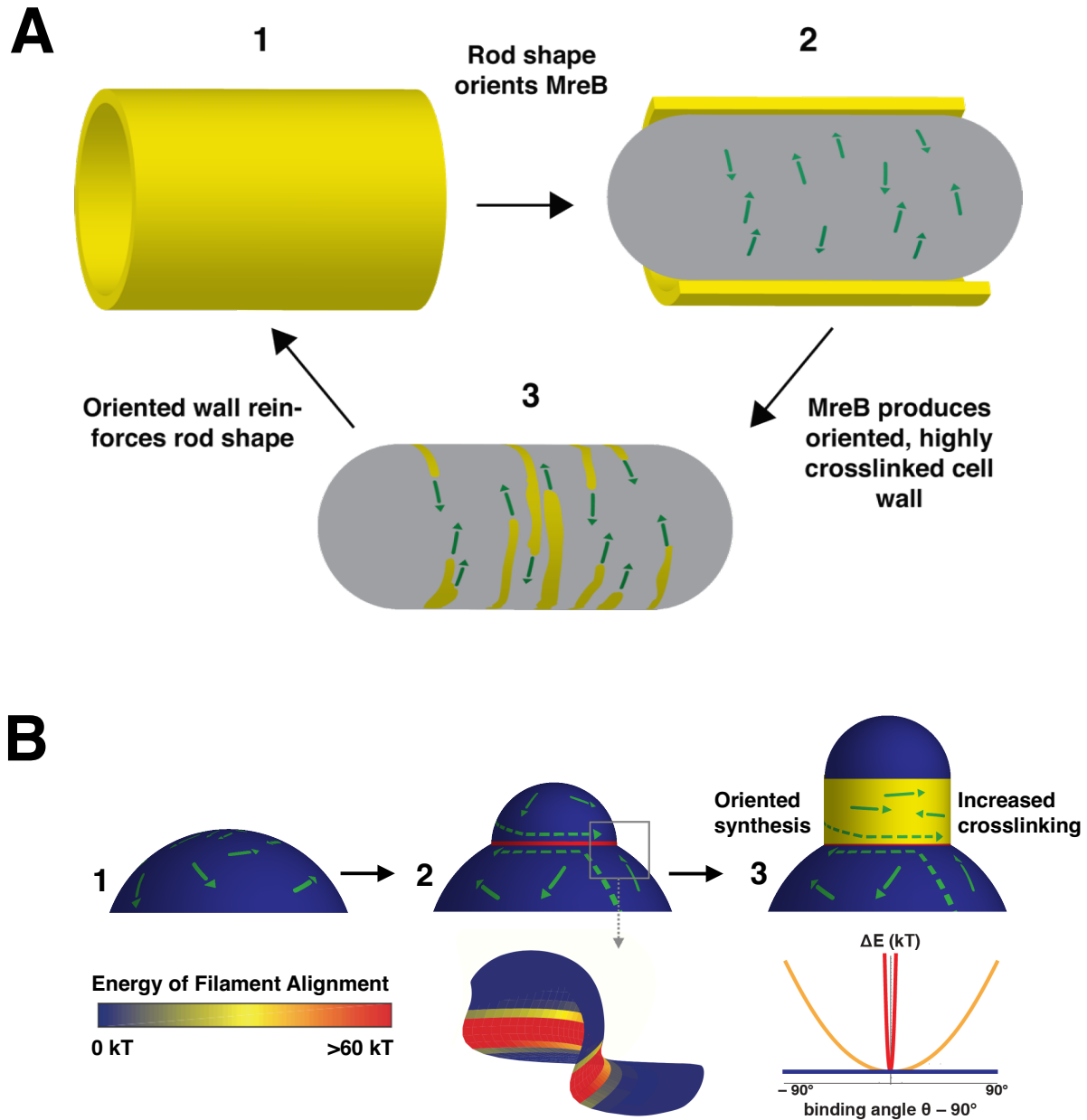


**Figure 2.7. Model for how MreB orientation along the greatest curvature can both maintain and establish rod shape. (A)** Rod-shaped cells present a single curved axis along which MreB filaments orient (1). This orientation determines the direction of MreB motion (2), thus orienting the insertion of new cell wall material around the rod, and allowing an increased crosslinking between strands (3). This highly cross-linked, circumferential arrangement of cell wall material reinforces rod shape (1), leading to more aligned MreB filaments, thus creating a local feedback between the orientation of MreB filaments, oriented cell wall synthesis, structural integrity of the rod, and overall rod shape.

**Figure 2.7 (Continued). (B)** MreB motion in spherical cells is isotropic (1), but the introduction of an outward bulge (2, upper) creates a curved geometry (red) at the neck of the bulge that initiates rod shape formation. Due to the high energy of alignment in this region, (2 lower and chart), any filaments that encounter the neck of the bulge would prefer to align to point around the neck rather than cross it, creating a ring-shaped region of aligned MreB motion that nucleates rod formation. Repeated rounds of oriented synthesis around the ring could initiate the elongation of a rod from the initial bulge site (3), beyond which rod shaped elongation would be self-sustaining. Colors correspond to the difference of alignment energies along the two principal curvatures at the negatively curved neck region (red), flat regions with one dimension of curvature (yellow), and the positively-curved sphere/bulge (blue).

The geometry at the interface of these outward bulges plays a central role in our model of rod shape formation. In three dimensions, the intersection at the bulge and the sphere creates a geometry that can establish a zone of aligned filaments: while both the parent sphere and the outward bulge have principal curvatures in the same direction (positive Gaussian curvature), the intersection of the sphere and bulge creates an interface with strong differences in principal curvatures, one inward, and one outward (negative Gaussian curvature). Upon entering these negatively curved regions it is energetically unfavorable for the inwardly curved MreB filaments to deviate from their preferred binding orientation, as our modeling indicates that this region presents a steep well in the energy profile for alignment (Figure 2.7B2 and Supplemental Text 1). Thus, filaments moving into this rim from either side would reorient to move along it, creating a concentrated band of filaments moving around the bulge neck. This concentrated ring of oriented MreB filaments may then construct a local region of rod shape that subsequently self-propagates into an emerging rod (Figure 2.7B3). In support of this hypothesis, immediately preceding rod shape formation, we observe concentrated bands of MreB transiently appearing at the neck of emerging bulges (Figure 2.6C, S5F).

Likewise, similar patterns of MreB accumulation at points of negative Gaussian curvatures have been observed in recovering *E. coli* L-forms (Billings et al., 2014).

The common observation of MreB accumulation at the necks of rod-producing bulges in both *E. coli* and *B. subtilis* hints at a solution to an outstanding discrepancy: Why do inwardly curved MreB filaments show an enriched localization at negative Gaussian curvatures (inward dimples or the more curved faces of bent cells) (Ursell et al. 2014), and how is this enrichment maintained as filaments move around the cell? The finding that MreB filaments align along the greatest curvature poses a solution: If the sharpness of filament alignment changes in response to the difference in principal curvatures in each region they pass through, areas of negative Gaussian curvature may act as points that focus the subsequent motion of filaments so that, on average, more filaments pass through these regions.

The tendency of MreB to align and move along the direction of greatest principal curvature may also explain the absence of MreB at cell poles. Consistent with our model for binding, we observed MreB filaments bound to the round poles of liposome tubes *in vitro* (Figure 2.4B, Movie S5). In the cell, however, MreB filaments move directionally, and filaments entering the symmetrically curved pole in any orientation would quickly translocate out into the cylindrical cell body where they would reorient along the single direction of curvature.

While rod-shaped cells show both an increased rate of growth and oriented MreB motion, it is unlikely these two phenomena are mechanistically linked. Rather, the decreased rate of growth of non-rods likely arises from a downstream effect of the lack of rod shape on cell physiology. Indeed, many spatial processes in *B. subtilis*, such as chromosome segregation and division site selection, read out and partition along the long axis established by rod shape (Jain et al., 2012). Thus, the slower doubling times observed in non-rod shaped cells may arise from the improper spatial organization of these processes, or stress responses to this spatial disarray.

As the curvature of membrane-bound MreB filaments (200nm) observed *in vitro* is much greater than the cell diameter (900nm), these findings suggest that the curvature of MreB filaments does not define a specific cell radius; rather filament curvature acts to orient PG synthesis to maintain (Harris, Dye, and Theriot 2014) or reduce cell diameter. If the curvature of MreB filaments reflects the smallest possible cell diameter, bacterial width may be specified by opposing actions from the two spatially distinct classes of PG synthases: a decreasing, “thinning” activity from the action of MreB and its associated SEDS family of PG synthases, and an increasing “fattening” activity from the non-MreB associated Class A PG synthases.

## **Conclusion**

To construct regular, micron-spanning shapes made of covalently crosslinked material, nature must devise strategies for coordinating the activities of disperse, nanometer-

scale protein complexes. This work reveals that the role of MreB in creating rod shape is to locally sense and subsequently reinforce differences in principal curvatures. The local, short-range feedback between differences in curvature, MreB orientation, and shape-reinforcing cell wall synthesis provides a robust, self-organizing mechanism for the stable maintenance and rapid reestablishment of rod shape, allowing the local activity of short MreB filaments to guide the emergence of a shape many times their size.

## Chapter 3 Future directions

### *Overview*

In this chapter, I will highlight some of the remaining questions that need to be addressed for a complete understanding of MreB and MreB-associated cell wall synthesis. In addition, I will provide some unpublished data showing preliminary work done to further test our mechanistic model of MreB function and rod shape formation using two approaches: (i) searching for curvature mutants of MreB and (ii) *in vitro* MreB localization and alignment in inverse micelles.

### Regulation of MreB

While the data in Chapter 2 demonstrate the curvature-sensing ability of MreB and a possible mechanism of action based on filament structure, the regulation of MreB should also play an important role in rod shape determination. Very little is known about how MreB is regulated, how it polymerizes *in vivo* and gets recruited to the membrane

to form a stable complex with associated proteins, and what determines the ratio of MreB in monomeric (cytoplasmic) and polymeric forms. Even the stoichiometry of each MreB-associated complex is unknown. Answers to all these questions are important to gain a complete understanding of cell shape, as changes in active MreB filament levels affect cell shape and growth: depletion or depolymerization of MreB causes cells to widen (Kawai, Asai, and Errington 2009; Furchtgott, Wingreen, and Huang 2011; Zheng et al. 2016).

Many studies have reported partial loss of function MreB mutations that alter cell width in *E. coli* (Monds et al. 2014; Ouzounov et al. 2016; Harris, Dye, and Theriot 2014), making cells wider. Possible mechanisms for the shape changes postulated by these studies include alterations in MreB curvature, but upon closer examination most of these mutations are in the nucleotide-binding pocket, or the monomer-monomer interface which makes it very likely that they are affecting polymerization kinetics and therefore active polymer levels. An overall reduction in polymerized, membrane-associated MreB filaments will lead to a reduction in organized, circumferential cell wall synthesis and likely result in shape aberrations. Thus, not only the curvature-sensing MreB filaments, but also the number of active, synthesizing enzyme-filament complexes are important in determining the final width and shape of the cell.

Another important consideration is the length of MreB filaments. At native expression levels, we observe diffraction-limited filament sizes, but other studies in *E. coli* have

reported the observations of both diffraction-limited spots, patches, as well as longer filaments (Reimold 2013; Olshausen et al. 2013). At higher expression levels, we have also observed longer filaments that display circumferential binding and motion. It is yet to be determined what sets the length of these filaments and if there is any regulation of filament length *in vivo*. Alternatively, filament lengths may not be regulated and may simply be a consequence of the amounts of available monomer, polymerization kinetics, fraction of MreB bound to the membrane and the number of enzyme complexes or nucleation sites available for filament association. Our model predicts that circumferential binding and motion should be somewhat robust to changes in filament length. The protoplast data shown in the previous chapter (Figure 2.3) provides some evidence to support this, but a detailed study of MreB filament lengths and their effect on cell shape and MreB orientation remains to be done.

In *B. subtilis* there exist 3 paralogs of MreB: MreB, Mbl and MreBH. These paralogs are believed to have partially redundant roles and have been shown to co-polymerize to form mixed filaments. This redundancy is not surprising as *B. subtilis* is well-known for having multiple paralogs of a large number of proteins including the wall teichoic acid ligases TagTUV and many others (Errington and Wu 2017). It is also known that these paralogs are expressed at different levels during growth, with MreB and Mbl being expressed more in the exponential phase, and MreBH being highly expressed during stationary phase and conditions of stress (Botella et al. 2011; Carballido-López et al. 2006; W.Z. Huang et al. 2013). However, there is evidence that each paralog may have

a slightly different function: Although all three paralogs co-polymerize *in vitro*, it has been shown that MreBH does not bind the membrane by itself (Dempwolff et al. 2011). Additionally, shape defects by depletion of each protein are slightly different (Kawai, Asai, and Errington 2009; Jones 2001). Studying these proteins assembled both individually and together on liposomes using cryo-EM, as has been done for *T. maritima* MreB (Salje et al. 2011) could provide useful information about how the structure and curvature of each protein differs and help determine the properties of the mixed filaments that are formed *in vivo*.

## The search for a straight(er) MreB mutant

Our curvature-sensing model proposes that the intrinsic curvature of MreB filaments provides them with an ability to distinguish between differences in principal curvature. A conclusive test for our model would be to identify MreB mutants that form less curved or straight filaments. Such a proposed mutant would be unable to sense the cell circumference and move aberrantly. It is expected that in the absence of circumferential motion, mutant cells would lose rod shape but confining these cells to rod shape using the methods detailed in Chapter 2 would not restore circumferential binding and motion. We attempted to rationally design these mutants based on the known structure of *T. maritima* MreB. As MreB is known to form non-helical, curved filaments, it is believed that this high curvature is possible due to the non-staggered arrangement of monomers in the filaments. Due to this non-staggering, the filament is able to bend at the monomer-monomer interface, which would be much harder to achieve in a staggered



arrangement of monomers, as is the case in other filaments such as actin. Additionally, there exists a gap in this monomer-monomer interface of MreB filaments which could be functioning as a hinge to allow filament bending (Figure 2.4D).

We identified 3 key residues (L268, I279 and M306) that form this gap in *B. subtilis* MreB by homology to *T. maritima* and mutagenized them to phenylalanine, in an attempt to fill this gap and prevent filament bending (Figure 3.1A). These mutant MreB were fluorescently tagged with GFP and expressed exogenously under an IPTG-inducible promoter in separate strains. The mutant strains appeared to have more stationary and slow-moving filaments but circumferential MreB motion could be observed in all three cases (Figure 3.1B). More cytoplasmic MreB was observed in MreBM306F than the other two mutants. Pauses and reversals were also more common in these mutant strains. Since the effect of these mutations may not be apparent due to co-polymerization with wildtype MreB, Mbl and MreBH, I created the same mutations in MreB from *Bacillus megaterium*, under the assumption that *B. megaterium* MreB will not co-polymerize with the existing MreB and its paralogs in cells. However, circumferential motion of *B. megaterium* MreB mutants was also observed, which could either indicate that the mutant MreB is still functional, or that *B. megaterium* MreB can co-polymerize with *B. subtilis* MreB. Finally, I created a double knockout of *mreB* and *mbl*, expressing mutant *B. subtilis* MreB exogenously, and as only MreBH remained functional, the effect of the MreB mutations should be more apparent in these strains. Cells in these strains were a mixture of rods and spheres, with rods showing

circumferential motion, and spheres showing unoriented motion (Movie S10). Similar results were seen in the  $\Delta mreB \Delta mbl$  strain even when wildtype MreB was expressed, indicating that the phenotype was an effect of the  $\Delta mreB \Delta mbl$  background rather than the MreB mutations (Movie S10). Furthermore, increasing the amount of mutant MreB in these strains produced more rod-like cells, making it unlikely that the curvature-sensing ability of MreB filaments was affected by these mutations. No mutation combinations were tested.

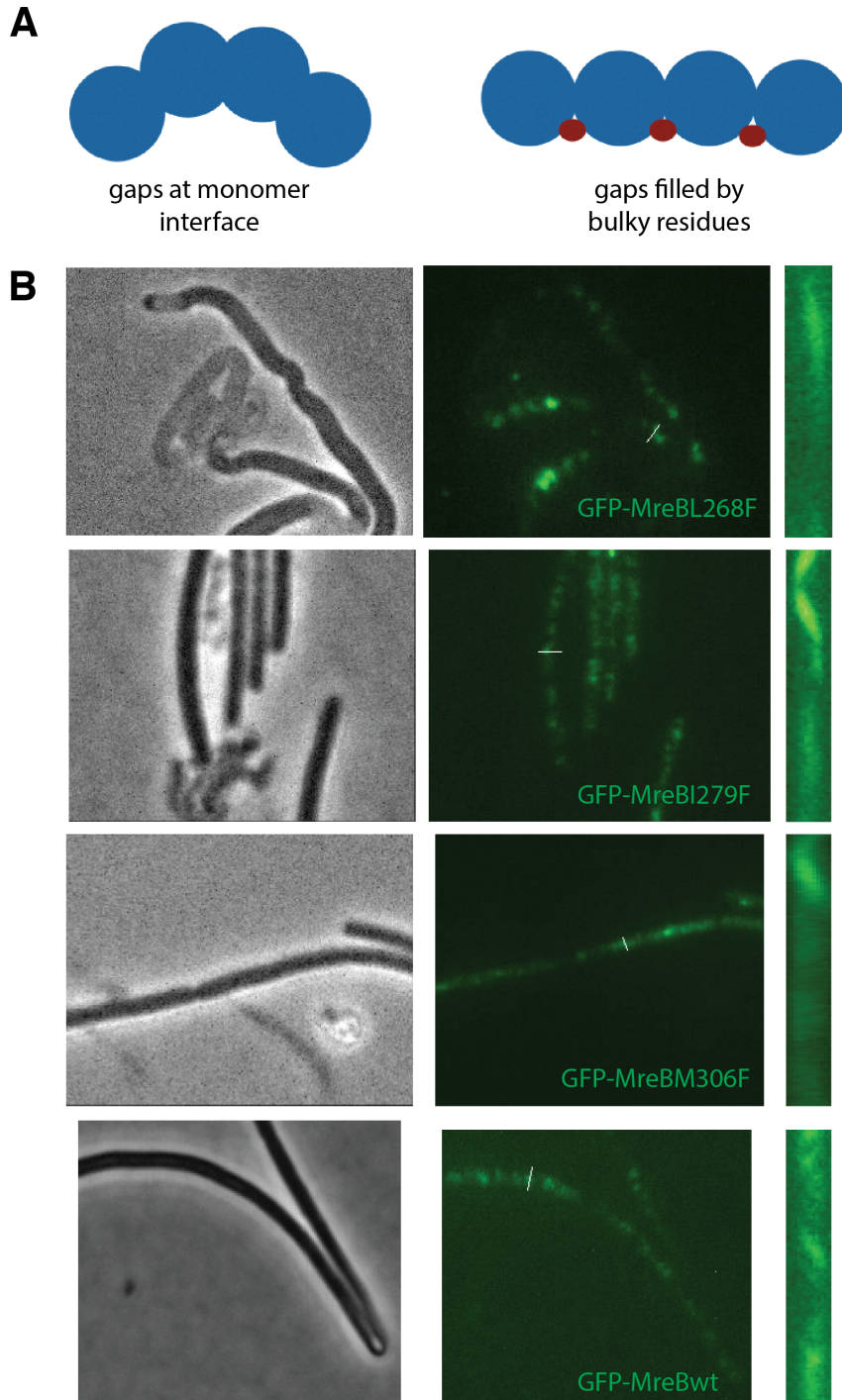


**Figure 3.1 MreB curvature mutants.** **A)** A diagram explaining the rationale behind selecting the residues L268, I279 and M306 for mutagenesis. MreB filaments are believed to bend at the monomer-monomer interface, resulting in overall curved filaments of a specific curvature (~200 nm radius of curvature). This bending is possible due to a gap that is occupied by small amino acids. Replacement of these residues by a bulkier amino acid may reduce the degree of bending between monomers, resulting in straighter filaments.

**Figure 3.1 (Continued). B)** Strains BSH14 (MreBL268F), BSH15 (MreBI279F), BSH16 (MreBM306F) and BSH25 (MreBwt), where sfGFP-MreB was expressed exogenously under an IPTG-inducible promoter are shown. Cells were grown in LB with 100  $\mu$ M IPTG and imaged using total internal reflection microscopy with images taken every 1 second for 2 minutes. On the right are kymographs of the regions indicated by white lines in the original images. Circumferential motion, indicated by diagonal lines in the kymographs can be seen in all three mutants.

An alternative approach for finding curvature mutants is to search for straighter MreB filaments in other organisms: Interestingly, there exists a family of rod-shaped, symbiotic bacteria called *Candidatus Thiosymbion* that has recently been discovered to grow by doubling its width rather than length, and dividing in half length-wise by placement of the FtsZ ring longitudinally (Leisch et al. 2012). This family also has an MreB-like protein and it would be interesting to explore the structure of this MreB and how it behaves *in vivo*.

### *In vitro* localization and alignment of MreB

Since decades, MreB has been a notoriously difficult protein to purify and work with *in vitro*, due to the presence of hydrophobic residues with an affinity for membranes. Most of the early *in vitro* work done with MreB used a mutant with the membrane-binding sequence deleted, which makes the protein easier to work with. However, since MreB polymerizes and functions on membranes, any conclusions drawn from these studies are likely not valid *in vivo*. Recently, cryo-EM studies have been done using wildtype *T. maritima* MreB assembled on liposomes (Salje et al. 2011; van den Ent, Izore, et al. 2014), which is a much more appropriate assay for biochemical studies of MreB. Our work in Chapter 2 uses the same approach, showing *T. maritima* MreB is highly curved

and able to deform liposomes into tubes. However, it has been difficult to control the concentration of proteins inside these liposomes, which are 100-200 nm wide, resulting in highly expressed, long filaments coating the inside of the liposomes.

We attempted to use fluorescence microscopy to observe purified *B. subtilis* MreB alignment in inverse micelles constrained to different widths. *B. subtilis* MreB formed patches on the inside surface of inverse micelles upon induction of polymerization. No patches were seen in the absence of polymerization (Figure 3.2A). We explored various buffer conditions but could only observe MreB patches, not individual filaments, which made it impossible to quantify filament alignment. Another challenge was nanofabrication of channels which would constrain liposomes to 800 nm – 2  $\mu$ m. Flowing the viscous oil phase of the inverse micelle solution through our fabricated devices was not possible. We then switched to using micropipettes of 2 – 10  $\mu$ m tip widths to constrain the micelles.

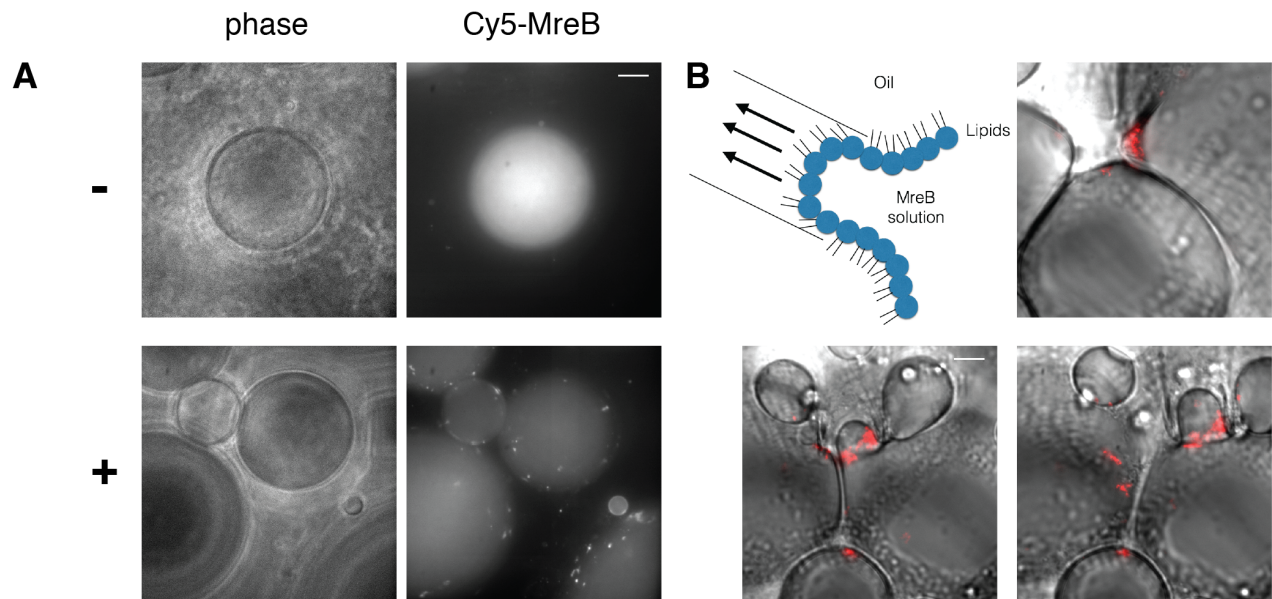


**Figure 3.2 Purified MreB assembled in inverse micelles *in vitro*.** **A)** Inverse micelles containing 5  $\mu\text{M}$  Cy5-MreB solution suspended in hexadecane. Shown are phase images and the sum of intensities of the z projections of Cy5-MreB. In the absence of polymerization (-), MreB is homogeneously distributed inside the micelles. Upon the induction of polymerization (+), by adding 5 mM  $\text{MgCl}_2$ , 1 mM EGTA and 15 mM imidazole (pH 7). MreB forms patches on the lipid surface of the micelles. **B)** Micropipettes were used to deform liposomes as shown in the top left panel (not drawn to scale). The micelles display an accumulation of Cy5-MreB (red) inside and at the neck region of these tubular deformations, similar to the localization of MreB seen during sphere to rod transitions *in vivo* in Figure 2.6C. All scale bars are 10  $\mu\text{m}$ .

MreB alignment was impossible to observe under these *in vitro* conditions using fluorescence microscopy, as individual filaments were unidentifiable. Therefore, I decided to observe MreB localization instead. I used micropipettes to create a suction force, which pushed parts of the large micelles into a tubular shape, resembling the bulges that spherical cells form when recovering rod shape (Figure 2.5B). Preliminary results showed MreB localization occurred inside and at the neck of this more curved region, similar to the localization seen at the neck of bulges in recovering cells, even though the scale is larger in this case (Figure 3.2B).

Further *in vitro* work could be done on supported lipid bilayers, using microfabricated surfaces of varying curvatures coated with lipids, where MreB localization can be easily measured. MreB alignment will be more difficult to determine unless suitable buffer conditions are identified and individual filaments can be seen using fluorescence microscopy. Although MreB alignment can be observed using cryo-EM, this technique is incompatible with the methods used to constrain liposomes to different widths (such as microfluidic devices or micropipettes). Thus, while *in vitro* study of MreB is important, especially since many properties of the filaments such as the Young's modulus are unknown, it remains to be a challenge to set up.

# Appendix

## Supplementary materials for Chapter 2

### Supplemental Figures

Figure S1– Varying magnesium levels in the growth medium changes cell shape. Related to Figure 2.1.

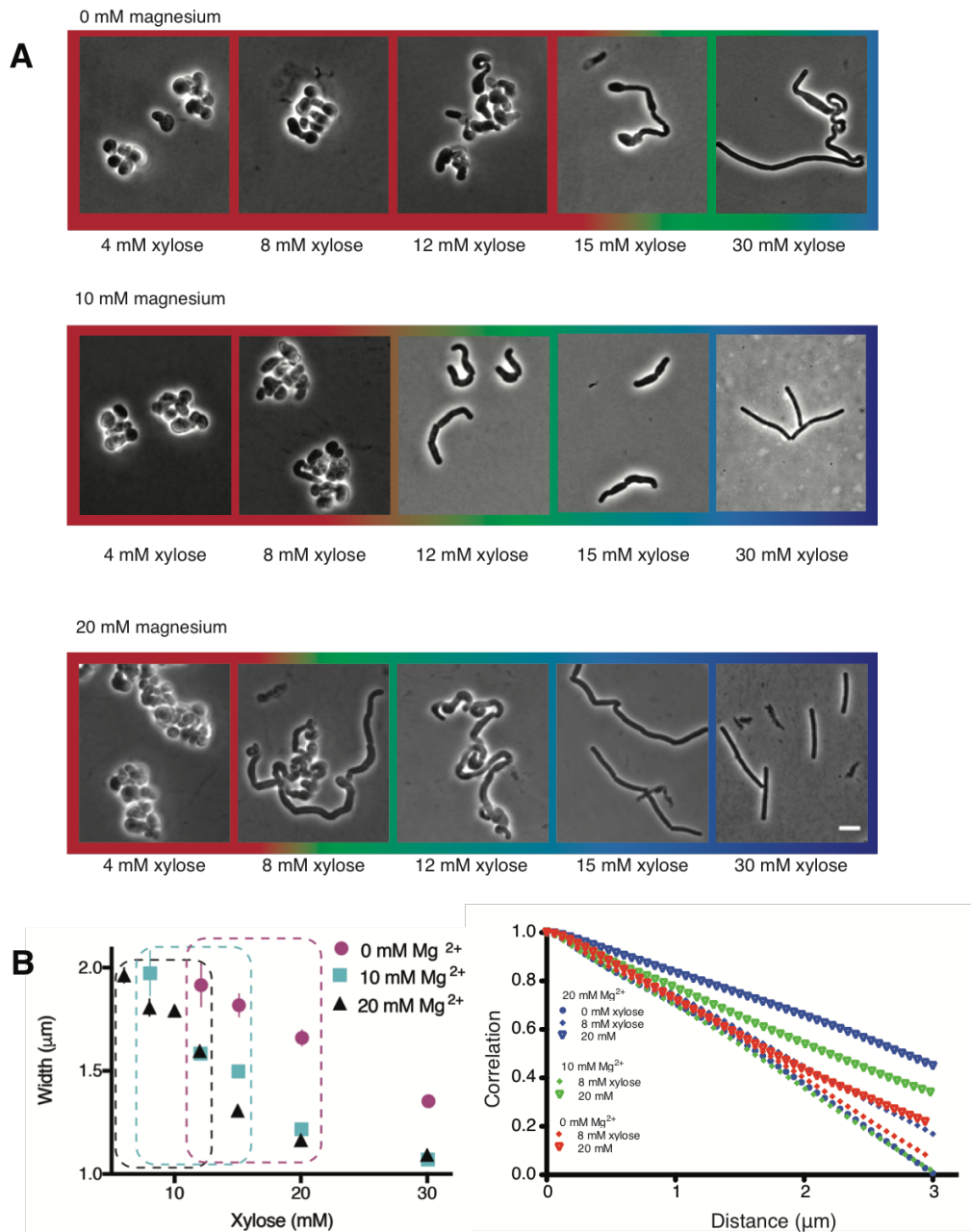
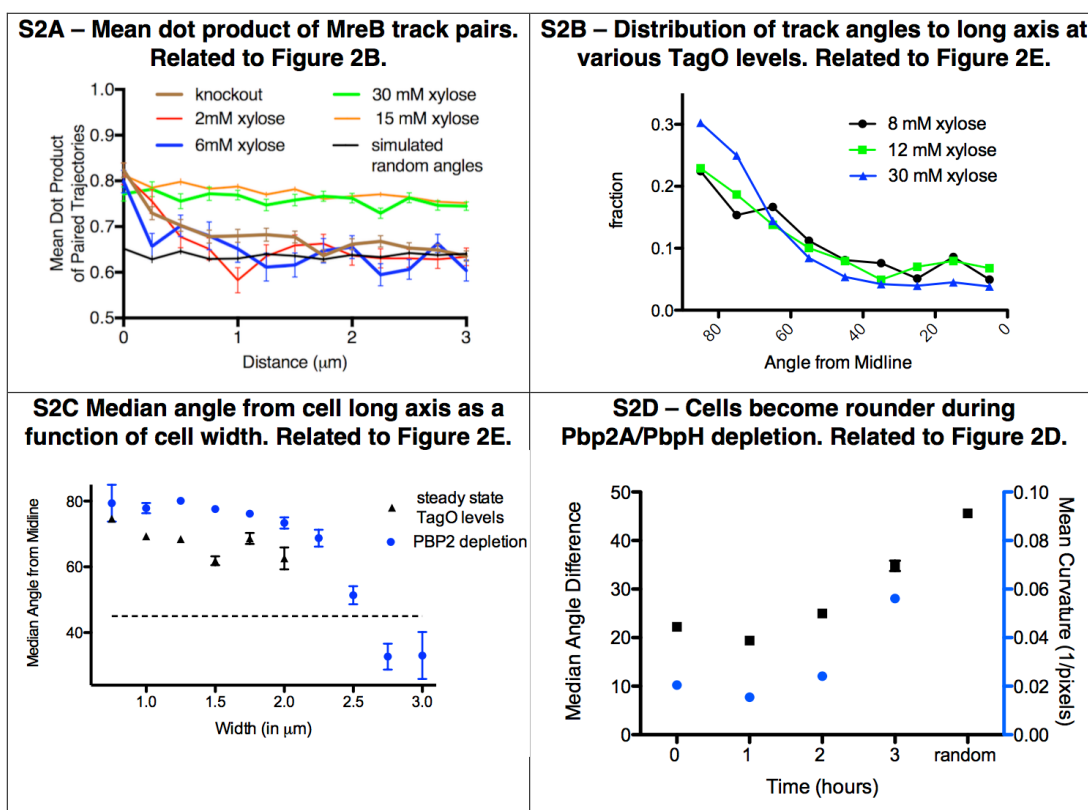




**Figure S1 (Continued)** – **(A)** TagO inducible cells grown in LB supplemented with varying  $Mg^{2+}$  levels (0, 10 and 20 mM), show similar trends in cell shape across increasing xylose concentrations, with the appearance of more rod-shaped cells that become thinner as xylose levels increase. Exogenous  $Mg^{2+}$  reduces the amount of TagO induction needed for rod shape, evidenced by shift in the amount of xylose required to form rods as  $Mg^{2+}$  is increased. (Color Outlines: Blue = rods, Green = Mixed rods and non-rods, Red = non-rods). **(B) Left** Plot of cell width as a function of TagO induction at different  $Mg^{2+}$  concentrations (error bars are SEM). Areas not plotted at lower xylose levels are regions where cells are round, with no width axis. Dotted rectangles mark conditions where both round cells and wide rods exist. Error bars are Standard Error of the Mean (SEM). **Right** At low xylose and magnesium levels, tangential correlation along the cell contours falls off faster, indicating loss of rod shape. Correlation of angles was calculated as described in methods. The curves shown are population averages of tangential correlations at selected xylose and magnesium concentrations. A cutoff of 3  $\mu m$  is applied as this is the mean cell length of *B. subtilis*.

**Figure S2 – Relationships between cell width, MreB orientation, and cell shape. Related to Figure 2.2.**



**S2E Cell roundness as a ratio of principal curvatures. Related to Figure 2E.**

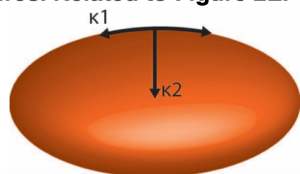


**Figure S2 – (A)** The mean dot product of MreB track pairs vs. distance between the pairs was calculated and binned at 0.25  $\mu\text{m}$  intervals. This shows a high alignment between pairs across the cell length for rods at high xylose (15 and 30mM). Round cells (2 and 6mM xylose) show a high alignment at very short distances ( $< 500$  nm), beyond which alignment falls off rapidly, approaching the value expected for randomly oriented angles (black line represents a simulation of a uniform angular distribution). **(B)** MreB filament motion is predominantly circumferentially oriented over a range of xylose levels (8-30mM) even though cells show varying widths. At 8 and 12 mM xylose, cells are a mix of rods and spheres, and therefore angles were only calculated for cells with identifiable long axes. **(C)** Median angle from the long axis of cells as a function of cell width at steady state TagO levels and PBP2a depletions (shown separately).

**Figure S2 (Continued).** (D) Mean sidewall curvature of cells increases during a Pbp2a/PbpH depletion (blue circles), along with a decrease in aligned MreB motion (black squares). (E) The principal curvatures along the cell length ( $\kappa_1$ ) and cell width ( $\kappa_2$ ) are calculated and the ratio  $\kappa_1/\kappa_2$  is taken as a measure of cell roundness. Cells become round as this ratio approaches 1. All error bars are SEM.

**Figure S3 - TagO Levels and Confinement. Related to Figure 2.3.**

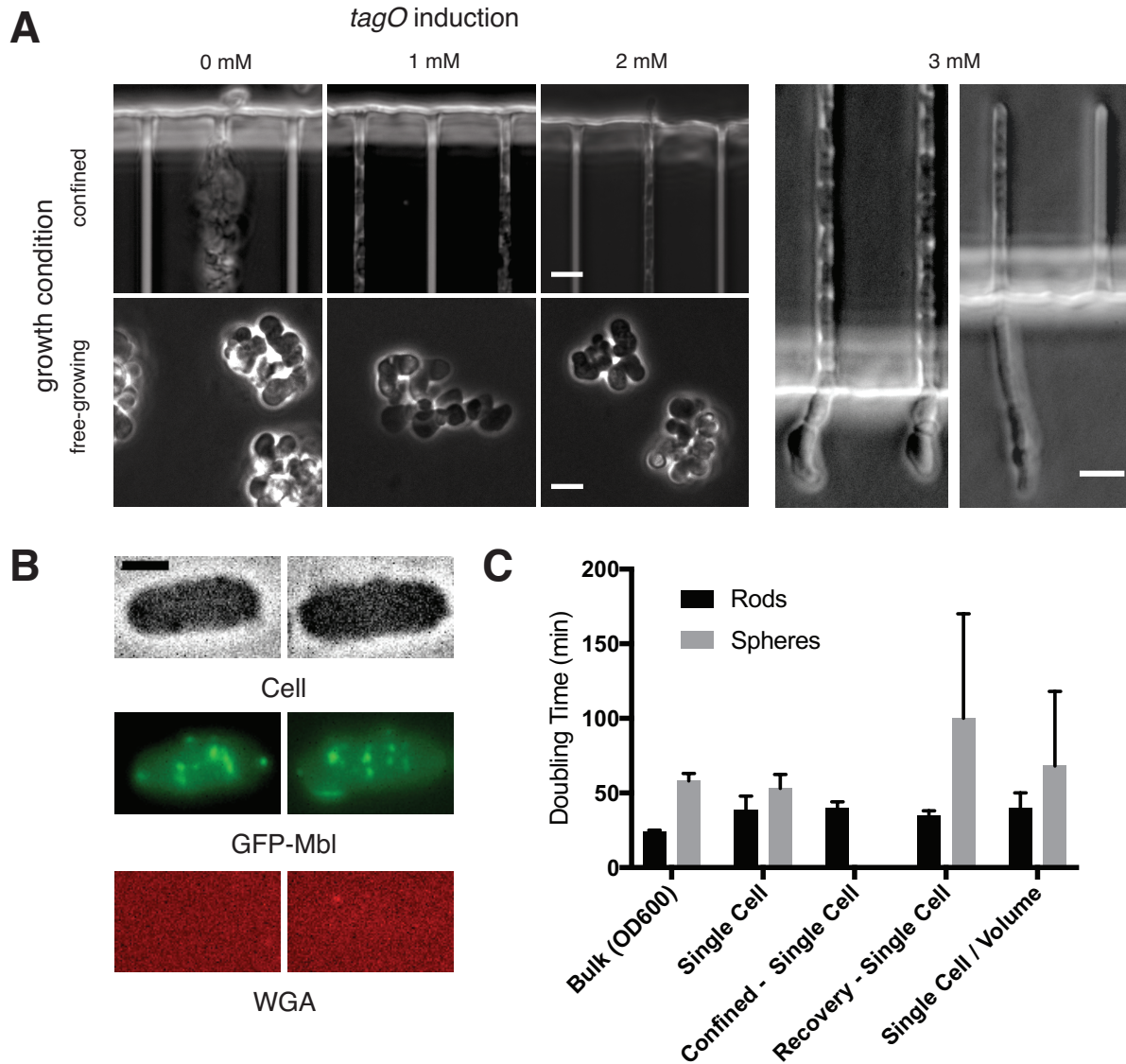


**Figure S3 (Continued)** – **(A)** Microfluidic confinement controls cell shape in cells with low TagO levels. (*Left*) Phase contrast images of BEG300 grown under differing teichoic acid induction levels in bulk culture or confined in chambers. (*Right*) Cells swell upon escaping from confinement. Swelling is visible both at initial stages of depletion, corresponding to when MreB movies were collected (left panel, cf. Figure 2.3C and Supplementary Movie 3), or at longer stages when cells were chained (right panel). Scale bars = 5  $\mu\text{m}$ . **(B)** Panels showing images of phase contrast, GFP-Mbl, and Alexa455-conjugated WGA of a representative protoplast confined into rod shape. MreB filaments are aligned along the cell circumference, (middle panel), but do not regrow cell wall as indicated by the lack of signal in the Alexa455 channel. Scale bars are 2  $\mu\text{m}$ . **(C)** Doubling time of BEG300 in different conditions. “Bulk” indicates cultures grown in liquid suspension and measured by  $\text{OD}_{600}$ . “Single Cell” indicates cells were grown under agarose pads, with doubling time measured by assaying the change in cell area over time using phase contrast microscopy. “*Confined - Single Cell*” indicates the doubling time of cell area of TagO-depleted cells confined into rod shape in microchambers as in Figure 2.3A and S3A; “*Recovery - Single Cell*” is the single-cell doubling time (in volume) of TagO-depleted cells during rod shape recovery in a cellASIC microfluidic device as in Figure 2.5B. Note that spherical cells in these recoveries show a slower doubling time with a larger standard deviation due to a subpopulation of cells dying during the experiment; “*Single cell / Volume*” indicates the doubling time of the volume of single cells grown in a cellASIC microfluidic device. As this chamber has a fixed Z height, cell volume can be approximated from measures of the 2D area. Error bars are standard deviation.

**Figure S4 – *T. maritima* MreB filaments assembled in liposomes support alignment to rod axis. Related to Figure 2.4.**

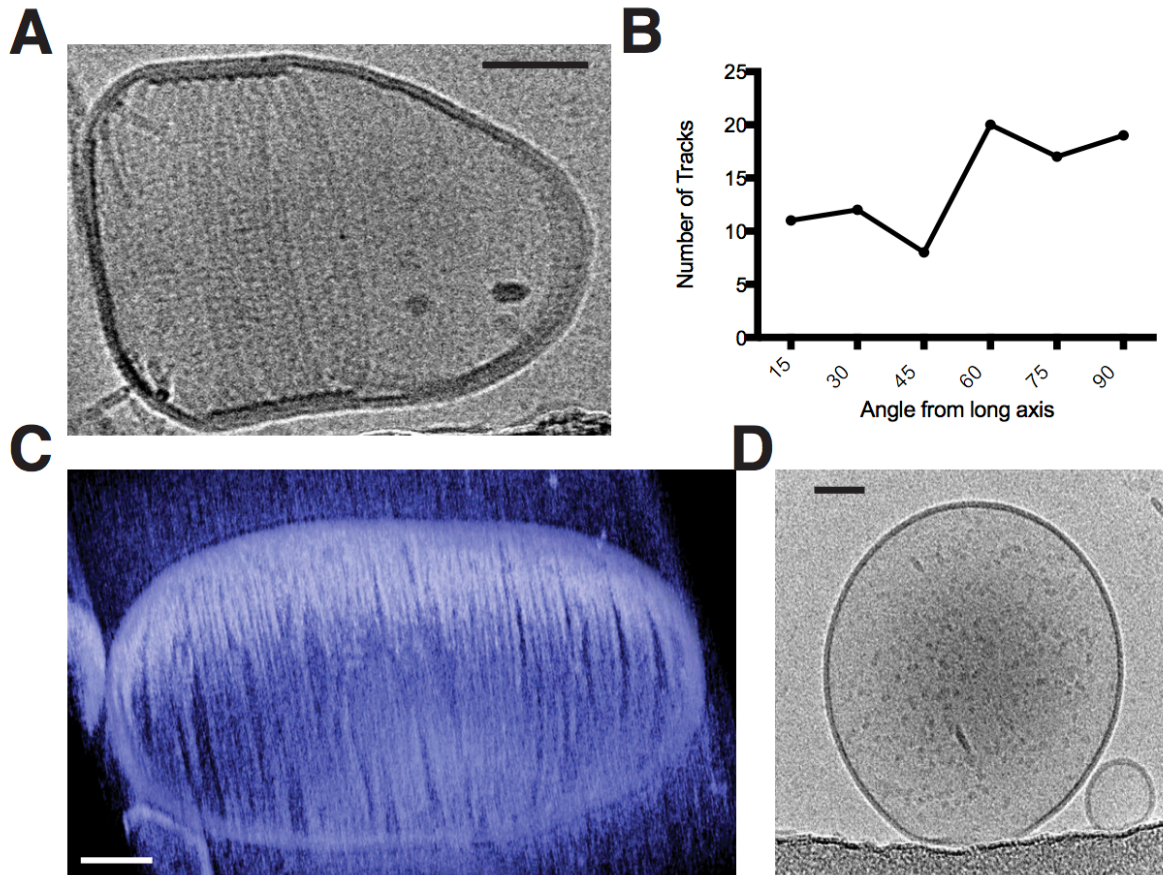


**Figure S4 – (A)** The arrangement of MreB filaments inside the liposome is helical. Scale bar is 50 nm. **(B)** Quantification of track angles for *T. maritima* MreB(V109E) filaments to the long axis of the liposome. Corresponding cryotomogram is depicted in Figure 2.4B. **(C)** Many long *T. maritima* MreB filaments inside an artificial liposome, assembled *in vitro* and imaged by electron tomography. Almost the entire inner surface of the liposome is covered with filaments, leading to deformation of the normally spherical liposome. Corresponding movie: SM5, first part. Scale bar is 50 nm. **(D)** Control showing that liposomes are spherical in the absence of MreB. Scale bar is 50 nm.

**Figure S5 – Growth of rod-shaped and spherical cells measured by doubling times, and rod shape recovery. Related to Figure 2.6.**

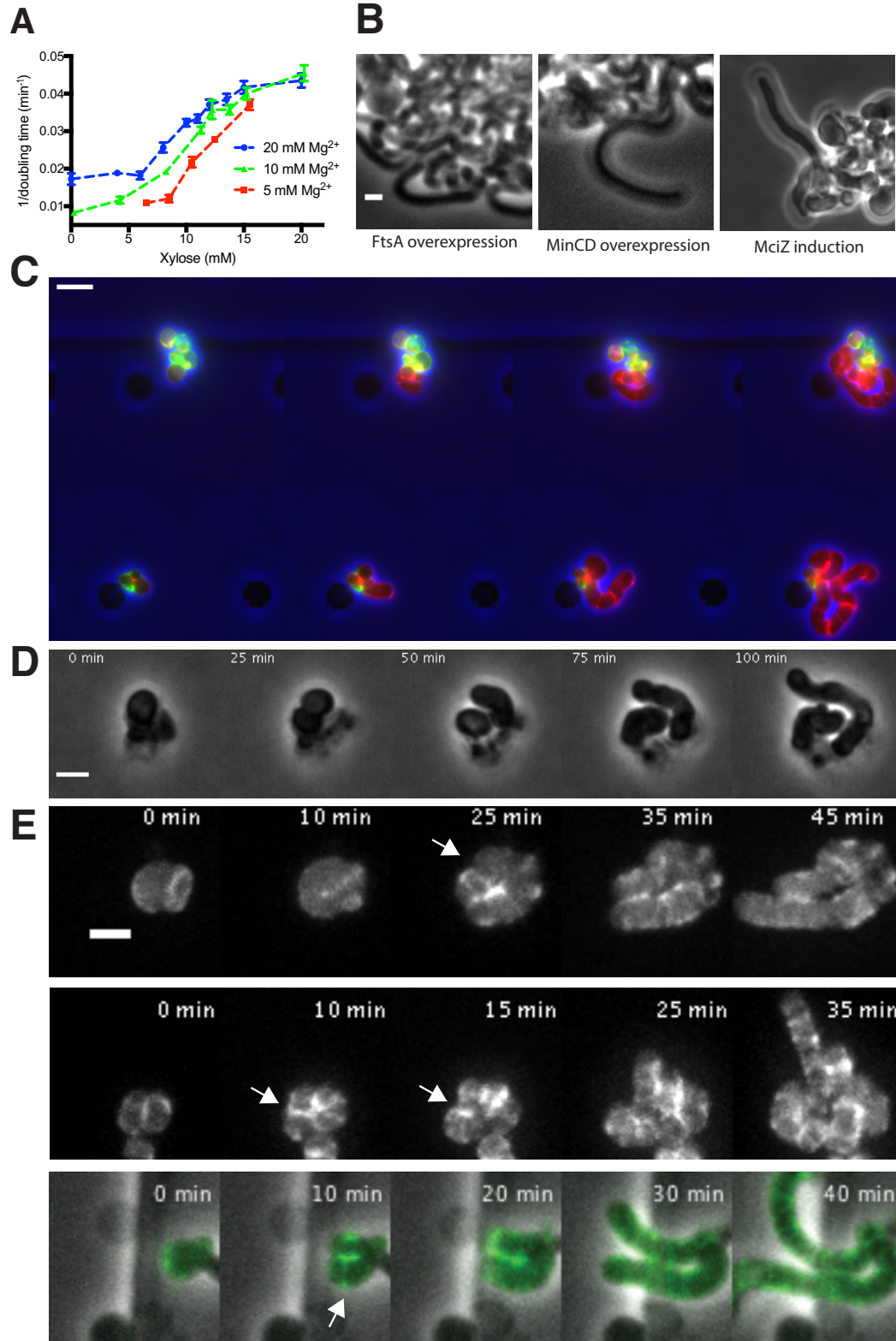


**Figure S5 (Continued)** – **(A)** Rate of doubling (1/doubling time), calculated from  $OD_{600}$ , increases with increasing levels of TagO as round cells become more rod-like. Increasing  $Mg^{2+}$  causes these curves to shift leftward, as  $Mg^{2+}$  stabilizes rod shape in combination with WTAs (see Figure S1A). Error bars are SEM. **(B)** Cy3B-ADA signal of cells in bulk culture 0, 5, and 25 min after a 20 min labeling pulse. Cy3B-ADA signal does not appreciably decrease for either rod or spherical shaped cells even at 25 min, indicating that there is no turnover of labeled material within the timescale of the FDAA incorporation experiment in Figure 2.6B. **(C)** Pulse chase labeling with FDAAs during TagO recoveries indicates that while emerging rods are composed of new cell wall, both spheres and rods incorporate new cell wall material. BCW82 was grown in a microfluidic chamber with 0 mM xylose, 20 mM  $Mg^{2+}$ , and 3  $\mu$ M HADA (green). Prior to imaging the medium was switched to 30 mM xylose (to induce TagO expression), 20 mM  $Mg^{2+}$  and 3  $\mu$ M cy3B-ADA (red, to visualize new cell wall incorporation). Cell outline (from phase) is shown in blue. Scale bar is 5  $\mu$ m; frames 30 min apart. **(D)** A montage of a rod shape recovery occurring after a division that produced an ovoid, near rod-shaped cell that subsequently elongated as a rod. This example taken from an experiment with BRB785, where Pbp2a was first depleted (in a *pbpH* null) to make round cells, then Pbp2a was reinduced with 1 mM IPTG. See also bottom panel of S5F. **(E)** Rod shape recovery occurs in the absence of cell division and FtsZ filaments. Inhibition of FtsZ filaments was conducted by three means: FtsA overexpression (bAB388, grown with 1 mM IPTG and 60 mM xylose), MinCD overexpression (bAB327 grown with 1 mM IPTG and 60 mM xylose), and MciZ induction (bAB343 grown in 1 mM IPTG and 30 mM xylose). In all cases, cells recovered rod shape. **(F)** MreB localizes in a ring-like structure (white arrows) at the neck of emerging bulges, immediately prior to rod shape formation. BEG300, containing GFP-MreB was depleted of TagO by growing in bulk culture in media lacking xylose. Cells were then loaded into a cellASIC device, and grown for 2 hours in the same media with 1 mM IPTG added to induce GFP-MreB expression. At the start of imaging, the media was switched to 30 mM xylose to induce TagO expression, and Z-stacks of GFP MreB were taken using a spinning disk confocal every 5 minutes. Shown above is the maximal intensity projection of entire cell.

Figure S6 - ConA staining of PY79 $\Delta$ *tagE* and muropeptide analysis of BEG300. Related to Figure 2.6B.

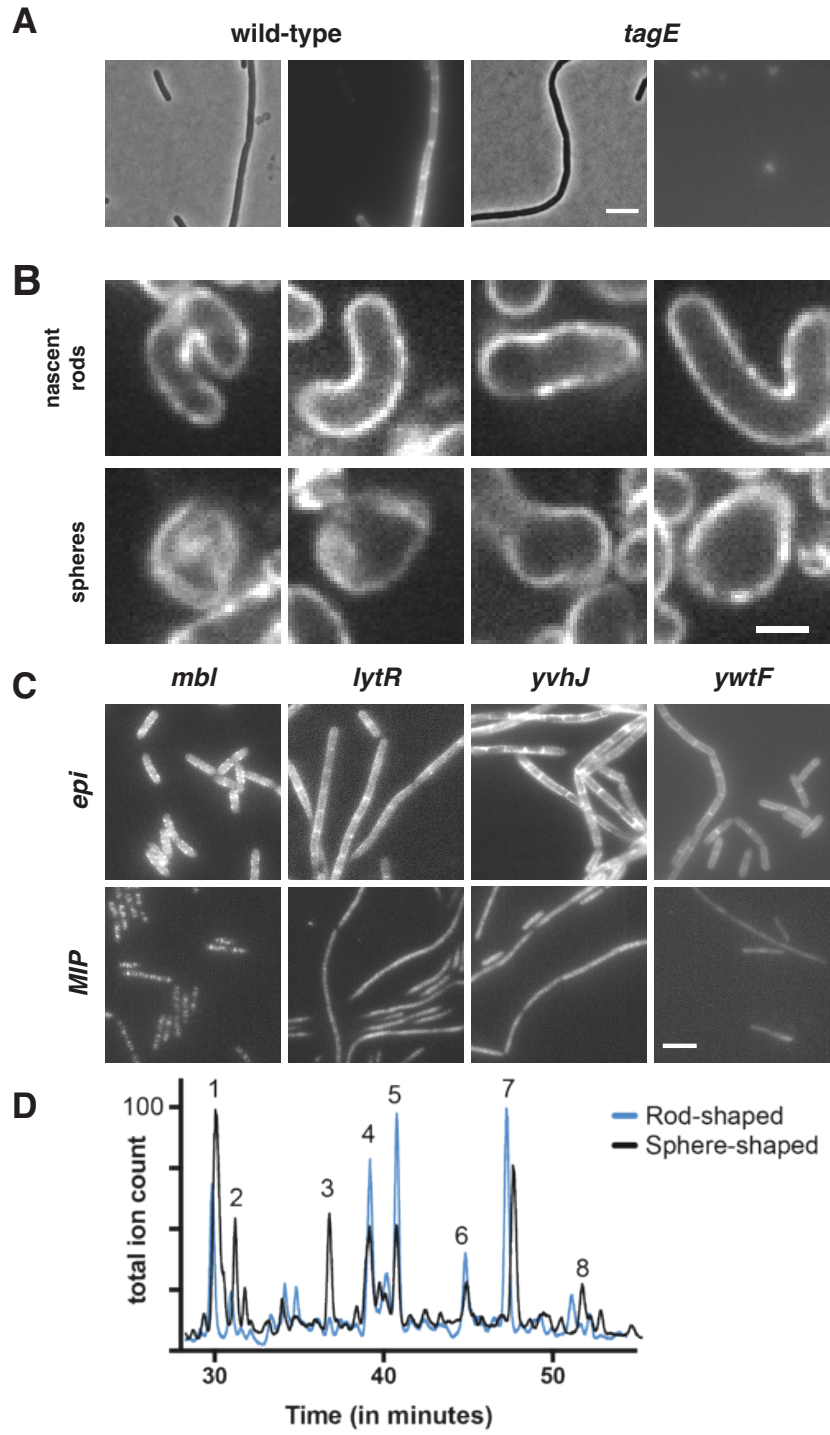




**Figure S6 (Continued)** – **(A)** Concanavalin A conjugated to Alexa Fluor 647 specifically stains wall teichoic acids and localizes uniformly around the entire cell during sphere to rod transitions. A comparison of PY79 and  $\Delta tagE$  cells stained with ConA-A647 reveals specificity of ConA for WTAs. The *tagE* gene is responsible for the glycosylation of wall-teichoic acids, rendering them susceptible to ConA binding. Scale bar is 5  $\mu\text{m}$ . **(B)** Fluorescence intensity of Alexa647-ConA, is comparable in rod shaped and round cells during sphere to rod recoveries. Furthermore, the WTA incorporation is diffuse, and not banded or localized. BEG300 was grown in bulk culture and rod shape was induced by increasing TagO levels (0 to 30 mM xylose). Scale bar is 2.5  $\mu\text{m}$ . **(C)** Wall teichoic acid ligases diffuse homogenously across the cell surface. Ligases were tagged at the native locus and promoter with msfGFP and imaged continuously with 100 ms exposures. Epifluorescent images were collected under oblique laser illumination and maximal intensity projections (MIPs) were created over 100 frames of TIRF illumination (see Movie S8). For comparison, msfGFP-tagged Mbl, which localizes in discrete patches, is shown. Scale bar is 5  $\mu\text{m}$ . **(D)** Overlaid LC/MS traces corresponding to reduced muropeptides isolated from the sacculi of rod-shaped and sphere-shaped *B. subtilis*. The total ion count was scaled to the highest peak for each trace, and muropeptides were identified under the total ion count. Peaks 1-3 correspond to uncrosslinked muropeptides; peaks 4-8 correspond to crosslinked muropeptides. Muropeptides identified included the following: a tripeptide (GlcNAc-MurNAc-L-Ala-D-Glu-m-DAP by its  $[M+1]=871.3$  (Exact mass=870.3) were identified under peak 1; a dipeptide (GlcNAc-MurNAc-L-Ala-D-Glu) was identified under peak 2  $[M+1]=699.7$  (Exact mass=698.7); a tetrapeptide (GlcNAc-MurNAc-L-Ala-D-Glu-m-DAP-D-ala by its  $[M+1]=941.2$  (Exact mass=940.2) was identified under peak 3; crosslinked, dimeric muropeptides were identified in peaks 4-7 containing the tetrasaccharide (GlcNAc-MurNAc-L-Ala-D-Glu-m-DAP-D-ala-m-DAP-D-Glu-L-Ala\_MurNAc-GlcNAc) by  $[M+1]=1795.8$  and  $[M+2]/2=898.4$ ; (Exact masses=1794.8); and peak 8 corresponded to a crosslinked, trimeric muropeptide containing two tetrapeptides (GlcNAc-MurNAc-L-Ala-D-Glu-m-DAP-D-ala) and a tripeptide (GlcNAc-MurNAc-L-Ala-D-Glu-m-DAP);  $[M+3]/3=906.9$  (Exact mass=2717.7). To calculate the amount of each species, peaks were integrated by their extracted ion chromatograms. Crosslinked species were calculated using previous literature quantification methods (Glauner et al., 1988). In the rod-shaped *B. subtilis*, 41% crosslinking was observed; in sphere-shaped *Bacillus subtilis*, only 11% crosslinking was observed.

## Materials and Methods

**Overnight culture growth.** All *B. subtilis* strains were prepared for experimentation as follows: strains were streaked from -80°C freezer stocks onto lysogeny broth (LB) agar plates. Following >12 hours of growth at 37°C, single colonies were transferred to serially diluted overnight bulk liquid cultures in LB supplemented with 20 mM magnesium chloride, placed on a roller drum agitating at 60 rpm, and grown at 25°C. After >12 hours growth to  $OD_{600} < 0.6$ , these starter cultures were transferred to or inoculated into subsequent growth conditions. All strains with *tagO* under inducible control were grown overnight in the presence of 30 mM xylose unless otherwise noted.

**Single cell and bulk growth rate measurements.** For the experiments in Figure 2.6B and Figure S3C, BEG300 cells were inoculated in the indicated medium (LB with 20 mM  $MgCl_2$  unless otherwise stated) from logarithmic phase overnights; “rods” were grown from a low dilution with 30 mM xylose, and “spheres” were grown with 0 mM xylose.

For bulk culture doubling time measurements, doubling times were calculated from the slope of a graph of time vs. dilution for a succession of serial dilutions of a given strain. Time, the dependent variable, was taken as the time for a given dilution to pass the OD cutoff of  $OD_{600} = 0.20$ .

Single cell measurements were made in three ways.

- i) Spherical and rod-shaped cells were allowed to grow on agarose pads made with LB supplemented with 20 mM  $MgCl_2$ . 30 mM xylose was added to agarose

pads for rod-shaped cells. Cells were imaged every 2 minutes for 4 hours with phase contrast microscopy as described in the section below.

- ii) Spherical and rod-shaped cells were grown in the CellASIC B04A plate in LB supplemented with 20 mM MgCl<sub>2</sub> for spherical cells and LB supplemented with 20 mM MgCl<sub>2</sub> and 30 mM xylose for rod-shaped cells. The CellASIC unit confined the cells in the Z dimension due to the fixed height of the ceiling. Cells were imaged every 10 minutes for 2 hours using phase contrast microscopy as described in the section below.
- iii) For cells growing in the mother machine microfluidic device (see below), the expansion of the cell length along the channel was quantified using FIJI (Schindelin et al., 2012; Schneider et al., 2012); only the cells closest to the mouth of the channel were counted. Since cells were always oriented along the length of the channel (see Figure 2.3A, S3A), changes in expansion in this dimension accounted for all growth.

**Imaging – phase contrast microscopy.** Phase contrast images were collected on a Nikon Ti microscope equipped with a 6.5 µm-pixel CMOS camera and a Nikon 100X NA 1.45 objective. Cells were collected by centrifugation at 6,000 x *g* for 2 min and re-suspended in the original growth medium. Unless otherwise specified, cells were then placed on No. 1.5 cover glass, 24 x 60 mm, under a 1 mm thick agar pad (2-3% agar) containing LB supplemented with 20 mM magnesium chloride. Unless otherwise noted, all cells were imaged at 37°C on a heated stage.

**Imaging – MreB particle tracking.** Images were collected on a Nikon TI microscope with a 6.5  $\mu\text{m}$ -pixel CMOS camera and a Nikon 100X NA 1.45 objective. Cells of strain BEG300 were grown overnight in LB supplemented with 30 mM xylose, 20 mM magnesium chloride, 1  $\mu\text{g}/\text{mL}$  erythromycin, and 25  $\mu\text{g}/\text{mL}$  lincomycin at 25°C at the specified xylose concentrations. 11  $\mu\text{M}$  isopropyl  $\beta$ -D-1-thiogalactopyranoside (IPTG) was added to induce GFP-MreB and the cells were shifted to 37°C and allowed to grow for 2 hours before imaging. Cells of strain BEG202 ( $\Delta tagO$ ) with GFP-Mbl under a xylose-inducible promoter were grown overnight at 25°C in LB supplemented with 20 mM magnesium chloride and 0.125 mM xylose, and shifted to 37°C for 2 hours before imaging. Cells were placed on cleaned glass coverslips thickness No. 1.5, as described in the next section. 3-6% agar pads were prepared in LB supplemented with 20 mM magnesium chloride, 11  $\mu\text{M}$  IPTG and the desired concentration of xylose. Images were collected for 3 min at 1 or 2 s intervals, as specified.

**Imaging – slide preparation.** Coverslips were sonicated in 1 M KOH for 15 min, followed by 5 washes with water. Coverslips were washed twice with 100% ethanol, and then sonicated in 100% ethanol, followed by one more wash in 100% ethanol. They were stored in ethanol and dried for 10 min before use.

**Imaging – spinning disk confocal.** Images were collected on a Nikon TI microscope with a Hamamatsu ImagEM (EM-CCD) camera (effective pixel size 160 nm) and Nikon

100X NA 1.45 TIRF objective. Z stacks were obtained at 0.2  $\mu\text{m}$  slices. Total image depth was 3  $\mu\text{m}$ . Only the top 3 slices of the cell were used in maximum intensity projections in Figure 2.3D.

**Image processing.** All image processing unless otherwise specified was performed in FIJI (Schindelin et al., 2012; Schneider et al., 2012). Images used for particle tracking were unaltered, except for trimming five pixels from the edges of some videos to remove edge artifacts detected by the tracking software. Phase contrast images and fluorescent images of protoplasts were adjusted for contrast. Phase contrast images presented in the manuscript collected from cells in the custom microfluidic device, which did not undergo quantitative processing, were gamma-adjusted ( $\gamma=1.5$ ) to compensate for changes in brightness occurring at the device's feature borders; such processing was not used for growth quantification. The images for Supplementary Movie 2 were background-subtracted for viewing purposes; unaltered images were used for quantitative processing in all cases.

**Microfluidics.** The custom microfluidic setup used to confine cells in Figure 2.3A-C, Supplementary Figure 2.3A, and Supplementary Movie 3 was previously described in (Norman et al. 2014). Briefly, a polydimethylsiloxane slab with surface features was bonded to a 22 x 60 mm glass coverslip by oxygen plasma treatment followed by heating to 65°C for >1 hr. The features in our setup differed from those described in (Norman et al. 2014), particularly in the omission of a second, wider layer in the cell chambers, which

enhanced growth at timescales beyond that of our experiments. Syringes containing growth medium were connected to the microfluidic features using Tygon tubing and stainless steel dispensing needles (McMaster Carr Supply Company). Medium was supplied to cells at a constant rate of 2-5  $\mu\text{L}/\text{min}$  using automatic syringe pumps. Imaging was carried out using phase contrast microscopy as described above. For the microfluidics experiments in Figures 2.5 and 2.6 and Supplementary Movie 6 (top), 7, and 8, the CellASIC platform from EMD Millipore was used with B04A plates.

**Cell confinement experiments.** The cell confinement experiment in Figure 2.3A-C was conducted by first loading cells into the chamber: BEG300 cells were grown to stationary phase ( $\text{OD}_{600}$  3.0 – 5.0) in LB supplemented with 20 mM magnesium chloride, passed through a 5  $\mu\text{m}$  filter, and concentrated 100-fold before loading in the custom-made microfluidic device. Both phase contrast and fluorescent imaging were performed as described in the “Imaging” section above. For observing MreB movement, MreB-GFP expression was induced with 50  $\mu\text{M}$  IPTG upon loading into the microfluidic chamber, and cells were imaged every 2 s with a camera exposure time of 300 ms.

**MreB alignment within protoplasts.** Cells of strains bJS18 (GFP-Mbl) and bEG300 (GFP-MreB) were grown overnight at 25°C in the osmoprotective SMM media (LB supplemented with 20 mM magnesium chloride, 17 mM maleic acid, 500 mM sucrose, brought to a pH of 7.0) with maximum xylose induction (30 mM); cells were shifted to 37°C in the morning. For strain bEG300, the SMM media was supplemented with 8mM

xylose (for intermediate TagO induction). Following 2 hours of growth, 10 mg/mL of freshly suspended lysozyme was added to the cultures with  $OD_{600} > 0.2$ . After growing for 1-2 hours in lysozyme, the cells were spun and concentrated. 6% agar pads made in LB-SMM were made using a polydimethylsiloxane (PDMS) mold with crosses (2, 4 and 5  $\mu\text{m}$  arms and 5  $\mu\text{m}$  center). The cells were placed on the agar pad for 2 min, allowing the cells to settle in the crosses. The pad was then placed in a MatTek dish for imaging. To check for the presence of cell walls in protoplasts, wheat germ agglutinin conjugated to Alexa-555 was used. 20  $\mu\text{L}$  of 1 mg/mL stock was added to 1 mL of cells 20 min before the start of imaging. Some cultures, after inoculation in the MatTek dish, were incubated at 37°C for 30 min to allow cell growth.

**Depletions in liquid culture.** TagO depletions in Figure 2.2A were conducted using strain BEG300 in liquid culture. Cells were prepared as overnights, as described above, then grown at the specified xylose concentration at 37°C in LB with 20 mM magnesium chloride for 4 hrs. The cells were then imaged as described above in the “Imaging – MreB particle tracking” section.

Pbp2A depletions shown in Figure 2.2C were conducted in liquid culture using strain BRB785 with an IPTG-inducible Pbp2A fusion at the native locus with the redundant transpeptidase PbpH deleted. This strain was grown overnight in the presence of 2 mM IPTG, and then inoculated into CH media containing 2 mM IPTG, 0.015% xylose, and 20 mM magnesium chloride to stabilize the cells against lysis. At an  $OD_{600}$  of 0.6, cells were spun down in a tabletop centrifuge and washed 3 times in CH media lacking IPTG. Cells

were placed under agar pads containing 20 mM magnesium chloride, and spinning disk confocal images were taken every 5 s on a Nikon Ti microscope with a 100X 1.49 TIRF objective and a Hamamatsu ImagEM C9100-13 EM-CCD camera (effective pixel size of 160 nm).

**Depletions under solid state medium.** Depletions shown in Figure 2.5A were conducted using strain BEG300. Cells were prepared as overnights in LB with 1 mM magnesium chloride and 12 mM xylose. In the morning, they were washed in LB with 12 mM xylose and no magnesium and placed under a 3% agar pad with the same medium. Phase contrast images were collected every 5 min using a Photometrics CoolSNAP HQ2 CCD camera.

**Repletions.** Repletions of TagO or Pbp2a on pads, as shown in Figure 2.5B and Supplementary Movie 6 (bottom), were performed with strains BEG300 and BRB785 respectively. Cells were grown as overnights, as described above, then depleted at 37°C for >4 hours in LB with 20 mM magnesium chloride and collected by centrifugation at 6,000 x *g* for 2 min. The cells were re-suspended in LB supplemented with 20 mM magnesium chloride and 1 mM IPTG (BRB785) and 30 mM xylose (BEG300), placed under 5% agarose pads on coverslips with thickness No. 1.5 for imaging. Phase contrast images were collected every 5 min using a Photometrics CoolSNAP HQ2 CCD camera.

For the repletions shown in Figures 2.5B-C, 2.6A, Supplementary Figure S5C, and Supplementary Movie 6 (top) and 7, performed in the CellASIC microfluidic device in a B04A plate, BCW82 and BEG300 cells were grown to OD<sub>600</sub> 1.2 – 1.5 in LB supplemented



with 20 mM magnesium chloride, centrifuged to pellet large clumps for 3 min at  $< 500 \times g$ , and the supernatant loaded into the plate. Growth medium was supplied at 5-6 PSI. Cells were grown for at least an additional 30 min before the addition of inducer to the growth medium. Phase contrast images were collected every 10 min. Fluorescent images were collected on the imaging setup described in the “Imaging – MreB Particle Tracking” section above: GFP-MreB was induced upon loading into the microfluidic chamber with 1 mM IPTG, and MreB dynamics were observed for 3 min after every 10 min, using 300 ms camera exposures taken every 2 s.

For the repletions shown in Figure 2.6C and S5F, the same procedure was used, but with imaging performed on the spinning disk confocal microscope described in “Imaging – Spinning Disk Confocal”. Z-stacks were collected with a range of 3  $\mu\text{m}$  around the focal plane and 0.2  $\mu\text{m}$  steps. The MreB localization experiments were done using strain bEG300 with full induction of GFP-MreB (1mM IPTG) and recovering cells were imaged using the spinning disk microscope, collecting Z-stacks as described before.

Where indicated, instead of visualizing MreB dynamics, fluorescent D-amino acids (Kuru et al. 2012) (7  $\mu\text{M}$ ) were added to the growth medium in the CellASIC device: HADA during depletions of TagO (0 mM xylose) and Cy3B-ADA during repletion of TagO (30 mM xylose). Cells were washed with LB supplemented with 20 mM magnesium chloride containing no D-amino acids for 1-2 min before imaging.

To test if rod shape recovery occurs in the absence of cell division, 3 strains were tested (BAB327, BAB343 and BAB388). Cells of BAB327 and BAB388 were grown in CH media with 25 mM magnesium chloride in the absence of xylose at 37°C until  $\text{OD}_{600}$

~0.5 and diluted 10-fold in fresh media. After 2 hours of growth, IPTG was added to a final concentration of 1 mM (MinCD and FtsA, respectively) and cells were incubated for an extra 1 hour. Cells were imaged on a spinning disk confocal under pads with 1 mM IPTG and 60 mM xylose (for TagO repletion). Phase-contrast and fluorescent images were acquired at 10 minute intervals for a total of 8 hours. Cells of BAB343 were grown in LB supplemented with 20 mM, magnesium chloride in the absence of xylose at 25°C overnight. The next day, after 2 hours of growth in the same media at 37°C, IPTG was added to a final concentration of 1 mM (MciZ) and cells were incubated for an extra 1 hour. Cells were imaged on a spinning disk confocal under pads with 1 mM IPTG and 30 mM xylose (for TagO repletion). Phase-contrast and fluorescent images were acquired at 10 minute intervals for a total of 4 hours.

**Depletion and repletion of Magnesium in the CellASIC.** For Supplementary Movie 8, cells of BCW51 were grown overnight at 25° C in LB supplemented with 8mM xylose, 20 mM magnesium chloride, 1 µg/ml erythromycin and 25 µg/ml lincomycin (MLS). Cells were shifted to 37°C for 2 hours and loaded into the CellASIC B04A plate at OD<sub>600</sub> ~0.6. At the start of imaging, magnesium was depleted by flowing in LB supplemented only with 8 mM xylose and MLS at 3 psi. Images were collected every 20 min over a 4 hr period. Magnesium was resupplied to the cells by changing to LB supplemented with 8 mM xylose, 20 mM magnesium chloride, and MLS. Imaging was continued every 20 min for an additional 4 hrs.

**Measurement of cell wall incorporation in the CellASIC.** For Figure 2.6B and Figure S5C, the rate of cell wall incorporation was measured by growing BCW82 cells in LB at 5 psi in a CellASIC B04A plate. Cells were loaded after being grown from induced overnight cultures for 3 hours at 37°C with 15 mM xylose, resulting in somewhat fattened rod-shaped cells. Upon loading, cells were either fully induced (30 mM xylose) or fully depleted (0 mM xylose) for 3 hrs, then pulsed with 1 mM Cy3BADA for 20 min to saturate preexisting sites of D-amino acid incorporation. Subsequently, cells were pulsed with 1 mM NADA, washed for 3 min. in the growth medium, then fixed with 10% formalin for 40 min. Next, cells were washed in CH imaging medium for 20 min prior to imaging on the spinning disk confocal microscope described in the “Depletions in liquid culture” section above.

**Measurements of cell shape at steady state growth.** Cells were grown overnight at 25°C in LB supplemented with 30 mM xylose, 20 mM magnesium chloride, 1 µg/mL erythromycin and 25 µg/mL lincomycin. In the morning they were collected at  $OD_{600} \sim 0.2$ , spun in a tabletop centrifuge at 9000 rpm for 3 min and washed in LB supplemented with various xylose (0-30 mM) and magnesium chloride (0-20 mM) levels. 25-fold serial dilutions into LB supplemented with the same xylose and magnesium chloride concentrations were made and allowed to grow at 37°C for 4 hrs. Cells at  $OD_{600} \sim 0.2$  were concentrated by spinning in a tabletop centrifuge at 9000 rpm for 3 min. They were placed on a coverslip thickness No. 1.5 under 3% agarose pads made in LB supplemented with the same concentrations of xylose and magnesium chloride. Images

were collected using the imaging setup described in the “Imaging – phase contrast microscopy” section above, as well as with a Photometrics CoolSNAP HQ2 CCD camera. The magnification and pixel size were the same in both setups.

### **Measurements of Fluorescent-D amino acid turnover**

Cells of strain BCW82 were used, which has *dacA* knocked out to prevent FDAA loss from carboxypeptidase activity (Kuru et al. 2012). For rods, cells were grown overnight at room temperature in CH media supplemented with 30 mM xylose and 20 mM magnesium and transferred to 37°C in the morning. Spherical cells were grown overnight at 37°C in CH media supplemented with 20 mM magnesium. Cells at OD > 0.4 were labelled with 25 µM Cy3-BADA for 20 minutes. 600 µL of cells were subsequently spun down at 6000 rpm for 4 minutes and resuspended in fresh media. 200 µL of cells were immediately spun down again and resuspended in 20 µL of formalin to fix them. The remaining cells were allowed to grow at 37°C for 5 and 25 minutes before spinning and fixing. Cells were imaged on the spinning disk confocal and z stacks were obtained as described in the imaging section.

### **Muropeptide analysis**

To prepare muropeptides from strain BEG300, a similar protocol was performed as reported previously (Atrih et al., 1999; Kühner et al., 2014). An overnight culture of BEG300 (2 mL) was centrifuged at 10,000 rpm for 5 min. The cell pellet was subsequently resuspended in 1 ml 0.25% SDS in 0.1 M Tris/HCl (pH 6.8). The mixture was boiled at

100 °C for 20 minutes. After cooling, the suspension was centrifuged at 16,000 rpm for 10 minutes, and the pellet was washed with 1.5 ml H<sub>2</sub>O and centrifuged again at 16,000 rpm for 10 minutes. The pellet was then washed two more times with water. The pellet was then resuspended in 1 ml H<sub>2</sub>O and sonicated for 30 minutes. 500 µl of a solution containing DNase (15 µg/ml) and RNase (60 µg/ml) in 0.1 M Tris/HCl (pH 6.8) was added. After shaking at 37 °C for 2 hours, the enzymes were inactivated at 100 °C for 5 minutes. The mixture was pelleted at 16,000 rpm and washed with 1 ml H<sub>2</sub>O twice. Wall teichoic acid was removed from the pellet by resuspending the pellet in 500 µl of 1 M HCl and incubating the mixture at 37 °C for 4 hours. The pellet was then centrifuged and washed with water at least four times to neutralize the pH to approximately pH 6. Subsequently, the pellet was resuspended in 100 µl of digestion buffer (12.5 mM NaH<sub>2</sub>PO<sub>4</sub>) with 10 µl of mutanolysin (5 U/mL in H<sub>2</sub>O, from *Streptomyces globisporus*, purchased from Sigma Aldrich). Peptidoglycan was digested overnight, shaking at 37 °C. Subsequently, the sample was centrifuged at 16,000 rpm for 10 minutes and mucopeptides were reduced by adding 50 µl of sodium borohydride (10 mg/ml, H<sub>2</sub>O) was added. The mixture was incubated for 30 minutes. To quench the mucopeptide reduction, 1.4 µl of 20% phosphoric acid was added to adjust the pH to 4. The mixture was then used for LC/MS analysis. High-performance liquid chromatography (HPLC) was carried out on an Agilent Technologies 1260 Quaternary LC system using a SymmetryShield RP18 5 µM, 4.6 x 250 mm column (Waters, Part No. 186000112). Solvent A was 0.1% formic acid in water; Solvent B was 0.1% formic acid in acetonitrile. At a flow rate of 0.5 mL/min, Solvent B was increased from 0-20% in 100 minutes, held at 20% for 20 minutes, increased to 80%

by 130 minutes, held at 80% for 10 minutes, and subsequently reduced to 0% and held at 0% for 10 minutes. To analyze the muropeptide composition, muropeptides were identified by the masses observed under specific peaks in the total ion chromatograms. Similar muropeptides were observed as previously reported for other *Bacillus subtilis* strains (Kühner et al., 2014). To quantify the amount of muropeptides observed, exact masses were integrated using extracted ion chromatograms (EICs). Subsequently, we calculated the percentage crosslinking as previously reported (Glauner et al., 1988). Technical and biological replicates were performed for each strain background.

**Particle tracking.** The MATLAB based software uTrack was used for particle tracking (Jaqaman et al. 2008). We used the comet detection algorithm to detect filaments (difference of Gaussian: 1 pixel low-pass to 4-6 pixels high pass, watershed segmentation parameters: minimum threshold 3-5 standard deviations with a step size of 1 pixel) which, at our MreB induction levels gave better localization of the resultant asymmetric particles over algorithms that search for symmetric Gaussians. Visual inspection of detected particles confirmed that most of the particles and none of the noise were being detected. A minimum Brownian search radius of 0.1-0.2 pixels and a maximum of 1-2 pixels was applied to link particles with at least 5 successive frames. Directed motion propagation was applied, with no joins between gaps allowed. Tracks were visualized using the FIJI plug-in TrackMate (Tinevez et al., 2017). For sphere to rod transitions and cells confined in microfluidic channels, movies were processed by subtracting every 8<sup>th</sup> frame from each

frame to remove stationary spots using the FIJI plugin StackDifference before tracking. The tracking was done as described earlier in this section.

**Fluorescent analysis of TagTUV.** Strains containing fluorescent fusions to TagT, TagU, and TagV were grown as described in the “Overnight culture growth” section but in CH medium instead of LB. Cells were grown for 3 hours at 37°C before imaging, then collected by centrifugation at 6,000 x *g* for 2 min and re-suspended in CH. Cells were then placed on a glass coverslip thickness No. 1.5 under an agar pad thickness 1 mm made from CH and 1.5% agarose. Timelapse images were collected with TIRF illumination, using continuous 100 ms 488 nm exposures. Epifluorescent illuminated images were collected from a single exposure, while maximal intensity projections were formed from a series of continuous 100 ms TIRF exposures.

**Teichoic acid labeling with Concanavalin A.** BEG300 cells were grown from overnights as described in the “Fluorescent analysis of TagTUV” section at 37°C for 4 hours without xylose to deplete WTAs, then induced with 30 mM xylose for 1.5 hours to re-induce WTA expression. Cells were then moved to 25°C for at least 30 min and incubated with 25 µg/mL Concanavalin A conjugated to Alexa Fluor 647. Cells were collected by centrifugation at 6,000 x *g* for 2 min, washed with CH medium, then re-suspended in fresh CH medium. Cells were then placed on a glass coverslip thickness No. 1.5 under an agar pad thickness 1 mm made from CH medium and 1.5% agarose. For PY79 and BCW61 controls, lectin-Alexa Fluor conjugate concentration was 200 µg/mL. For non-quantitative

analysis, imaging was performed with the microscope described in “Imaging – MreB Particle Tracking”; for quantitative analysis, imaging was performed with the microscope described in “Imaging – Spinning Disk Confocal”. Quantification was performed in FIJI; pixel values were corrected for mean fluorescent background.

**Data analysis – selecting directional tracks.** The output of uTrack is the position coordinates of tracks over frames. We fit a line through these coordinates using orthogonal least squares regression to minimize the perpendicular distance of the points from the line of best fit. We used principal component analysis for orthogonal regression using custom written MATLAB code. The  $R^2$  values we obtain range from 0.5 to 1. We calculated mean track positions, angles and displacement using the line of best fit for all tracks. We also calculated the mean square displacement versus time of individual tracks and fit these curves to the quadratic equation  $MSD(t) = 4Dt + (Vt)^2$ , using nonlinear least squares fitting. As later times have fewer points and are noisier, we fit the first 80% of the data for each track. We determined  $\alpha$  by fitting a straight line to the  $\log(MSD(t))$  vs.  $\log(t)$  curve. The goodness of fit was evaluated by determining the  $R^2$  value. We selected tracks for linearity and directional motion, based on the following cutoffs:  $R^2 > 0.9$ , displacement  $> 0.2 \mu\text{m}$ , velocity  $> 1e^{-9} \mu\text{m/s}$ , and  $R^2$  of the linear fit of  $\log(MSD(t))$  vs.  $\log(t) > 0.6$ .

**Data analysis – cell segmentation.** The MATLAB-based software Morphometrics (Ursell et al., 2017) was used to segment phase contrast images of cells. We used the



phase contrast setting for rod-shaped and intermediate states and the peripheral fluorescence setting for spherical states, because in this latter condition, peripheral fluorescence empirically did a better job of fitting cell outlines. The cell contours obtained were visually inspected and any erroneous contours were removed by custom written MATLAB code.

**Data analysis – track angles with respect to the long axis of the cell.** Track angles were calculated with respect to the cell midline as defined by the Morphometrics “Calculate Pill Mesh” feature, which identifies the midline based on a unique discretization of the cell shape determined from its Voronoi diagram. The difference between the track angle and midline angle was then calculated. Since the track angles  $\theta_t$  and midline angles  $\theta_m$  both ranged from  $-90^\circ$  to  $90^\circ$ , the range of angle differences  $\Delta\theta = \theta_t - \theta_m$  was  $-180^\circ$  to  $180^\circ$ . We changed the range to 0 to  $180^\circ$  by the transformation:  $\Delta\theta = 180 + \Delta\theta$  if  $\Delta\theta < 0$ , and 0 to  $90^\circ$  by the transformation:  $\Delta\theta = 180 - \Delta\theta$  if  $\Delta\theta > 90$ . The standard deviations (SD) reported are measured from the distributions with a range of 0- $180^\circ$  as this SD most accurately depicts deviations from  $90^\circ$ .

**Data analysis – mean dot product of tracks.** Custom written MATLAB code was used to calculate the normalized dot product ( $DP$ ) of track pairs along with the distance ( $d$ ) between their mean positions  $\bar{x}$  and  $\bar{y}$  as follows:

$$DP_{ij} = \cos(\theta_i - \theta_j), \quad d_{ij} = \sqrt{(\bar{x}_i - \bar{x}_j)^2 + (\bar{y}_i - \bar{y}_j)^2}$$

To eliminate out-of-cell tracks we only considered those that had 3 other tracks within a 5  $\mu\text{m}$  radius of their mean position. The dot product of track pairs (DP) and distance (d) between them was stored in data files, along with all the previous information for each individual track ( $R^2$ , velocities, angles, mean positions, displacement etc). The files were then parsed using the cutoffs described in the “Data analysis – selecting directional tracks” section. The tracks were binned based on the distance and the mean dot product calculated for each distance range as follows:

$$\overline{DP} = \frac{1}{N} \sum_{i>j}^N \cos(\theta_i - \theta_j)$$

A cutoff of 3  $\mu\text{m}$  was chosen as the maximum binning distance, which is the average length of a cell.

**Data analysis – simulation of random angles.** A data file containing simulated tracks was created by a custom written MATLAB script, which generates random angles distributed randomly on a 100 x 100  $\mu\text{m}$  area. Each track has  $R^2 = 0.95$ , velocity = 25 nm/s and displacement = 1  $\mu\text{m}$ . The same analysis code was run on these simulated tracks to generate track pairs with dot product and distance stored in a new data file. The data file was parsed using the same cutoffs as the real data and the mean dot product for each distance range calculated. The total numbers of trajectories within the simulation were much higher than the actual data (2-10 times higher).

**Data analysis – cell width.** Pill meshes were created using Morphometrics (Ursell et al., 2017), which calculates the coordinates of line segments perpendicular to the cell long

axis. For cell widths at various steady state TagO and Mg<sup>2+</sup> levels, the distance of these line segments was calculated using a custom written MATLAB script and the maximum width along the length of the cell was taken as the cell width. When measuring cell width nearest to a track (for calculating track angle as a function of cell width), the mean width of the 10 nearest contour points from the track was calculated using a custom written MATLAB script. Cell widths of emerging bulges and rods from round cells were measured manually in FIJI. Our ability to segment individual spherical cells was limited by their nonuniform contrast, perhaps arising from the nonuniform thickness of these cells in the Z dimension; consequently, Morphometrics-based width measurements in these cells was limited, especially in cells exceeding 2 μm in diameter.

### **Data analysis – cell curvature.**

Sidewall curvature of cells was extracted from the pill mesh obtained from Morphometrics. The curvature values are calculated from 3 successive contour points and smoothed over 2 pixels. The mean curvature of 3 nearest points to each track were calculated from both sides of the cell contour and called the mean curvature. Principal curvature ratio was calculated by dividing the sidewall curvature with the curvature in the radial direction (calculated from cell width assuming the cell is radially symmetric). For radial curvature we used the following expression, where  $r_{cell}$  is half the cell width:

$$\kappa_2 = \frac{1}{r_{cell}}$$

A value close to 1 indicates the two principal curvatures are similar and the cells are round.

### **Data analysis – time and curvature plots of rod shape recovery.**

Phase contrast images were used to show rod shape emergence from local bulges. Edges were enhanced in FIJI and contrast adjusted to give bright cell outlines in the images. The stack was then colored in time using temporal color code function in FIJI. To create the curvature plot, the phase contrast images were run through Morphometrics which calculates the curvature at each contour point along the cell outline. The contour points of interest were selected and plotted using a custom written MATLAB script, which colored each point according to its local curvature as calculated by Morphometrics. To provide a good resolution for positive curvatures, we rescaled the color map such that negative curvatures were colored blue and positive curvatures were scaled by their curvature value.

### **Data analysis – single cell doubling times**

Data from agar pads experiments was analyzed using custom written MATLAB code. Data from cellASIC experiments was analyzed in Morphometrics to get areas for each cell. For growth rates during sphere to rod transitions, the data was collected by manually measuring the areas of the sphere and rod regions of the same cell in FIJI. In all cases, the area of each cell per frame was calculated and the log plot of area vs time was fit to a line. The doubling time was calculated using the slope of this line.

### **Data analysis – Tangential correlation of cell contours.**

Cell contours were used to calculate tangent angles using the equation:  $\theta_i = \tan^{-1} \frac{y_{i+1} - y_i}{x_{i+1} - x_i}$

. The correlation between angles was calculated using the cosine of the angle difference binned as a function of number of points (n) between the angles:  $G(n) = \frac{1}{N} \sum_{i=1}^N \cos(\theta_{i+n} - \theta_i)$ . The number of points was converted to contour length using the pixel size of the camera to get the final correlation function:  $G(l) = \frac{1}{N} \sum_{i=1}^N \cos(\theta_{i+l} - \theta_i)$ .

For straight rods, the contour angles on average remain highly correlated over larger distances, becoming uncorrelated at the cell pole. In spherical cells, the angles become uncorrelated at shorter distances.

### **Data analysis – MreB(V109E) orientation in electron cryotomograms**

The top and bottom slices of the tubular liposomes were used, and MreB filaments were visually identified. The filament angles were measured manually in FIJI.

### ***T. maritima* MreB protein purification**

Full length, un-tagged *Thermotoga maritima* MreB and MreB(V109E) were purified as described previously (Salje et al. 2011).

### ***In vitro* reconstitution of *T. maritima* MreB filaments inside liposomes**

The protein was encapsulated inside unilamellar liposomes following a previously published protocol (Szwedziak et al., 2014). For this, 50  $\mu$ L of *E. coli* total lipid extract, dissolved in chloroform at 10 mg/mL, was dried in a glass vial under a stream of nitrogen

gas and left overnight under vacuum to remove traces of the solvent. The resulting thin lipid film was hydrated with 50  $\mu\text{L}$  of TEN100 8.0 (50 mM Tris/HCl, 100 mM NaCl, 1 mM EDTA, 1 mM  $\text{NaN}_3$ , pH 8.0), supplemented with 20 mM CHAPS (Anatrace), and shaken vigorously at 800 rpm using a benchtop micro centrifuge tube shaker for 2 hrs. The lipid-detergent solution was then sonicated for 1 min in a water bath sonicator. Subsequently, 50  $\mu\text{L}$  of MreB protein solution at 30  $\mu\text{M}$ , supplemented with 0.5 mM magnesium ATP (Jena Bioscience, Germany) was added and left for 30 min at room temperature. Next, the mixture was gradually diluted within 10-20 min to 600  $\mu\text{L}$  with TEN100 8.0 plus 0.5 mM magnesium ATP (without detergent) to trigger spontaneous liposome formation. 2.5  $\mu\text{L}$  of the solution was mixed with 0.2  $\mu\text{L}$  10 nm IgG immunogold conjugate (TAAB, UK) and plunge-frozen onto Quantifoil R2/2 carbon grid, using a Vitrobot automated freeze plunger (FEI Company) into liquid ethane.

### **Electron cryomicroscopy and cryotomography**

2D electron cryomicroscopy images were taken on an FEI Polara TEM (FEI Company) operating at 300 kV with a 4k x 4k Falcon II direct electron detector (FEI Company) at a pixel size of 1.8  $\text{\AA}$ . For electron cryotomography, samples were imaged using an FEI Titan Krios TEM (FEI Company) operating at 300 kV, equipped with a Gatan imaging filter set at zero-loss peak with a slit-width of 20 eV. A 4k x 4k post-GIF K2 Summit direct electron detector (Gatan) was used for data acquisition with SerialEM software (Mastronarde, 2005) at a pixel size of 3.8  $\text{\AA}$  at the specimen level. Specimens were tilted from  $-60^\circ$  to

+60 ° with uniform 1 ° increments. The defocus was set to between 8 and 10 μm, and the total dose for each tilt series was around 120-150 e/Å<sup>2</sup>.

## Image processing

Tomographic reconstructions from tilt series were calculated using RAPTOR (Amat et al., 2008) and the IMOD tomography reconstruction package followed by SIRT reconstruction with the TOMO3D package (Agulleiro and Fernandez, 2011; Kremer et al., 1996). Movies showing liposomes were prepared with Chimera and PyMOL (DeLano, 2002; Pettersen et al., 2004).

## Strain construction

**BCW51** [*ycgO::Pxyl-tagO*, *tagO::erm*, *amyE::sfGFP-mreB*, *sinR::phleo*] was generated by transforming BEG300 with a Gibson assembly consisting of three fragments: 1) PCR with primers Sinr\_up\_F and Sinr\_up\_R and template PY79 genomic DNA; 2) PCR with primers oJM028 and oJM029 and template plasmid pWX478a (containing *phleo*); 3) PCR with primers Sinr\_DOWN\_R and Sinr\_DOWN\_F and template genomic DNA.

**BCW61** [*tagE::erm*] was generated by transforming PY79 with a Gibson assembly consisting of three fragments: 1) PCR with primers oCW054 and oCW055 and template PY79 genomic DNA; 2) PCR with primers oJM028 and oCW057 and template plasmid pWX467a containing *cat*; 3) PCR with primers oCW058 and oCW059 and template PY79 genomic DNA.

**BCW72** [*yvhJΩPxylA-mazF (cat)*] was generated by transforming PY79 with a Gibson assembly consisting of three fragments: 1) PCR with primers oCW139 and oCW141 and template PY79 genomic DNA; 2) PCR with primers oJM029 and oMK047 and template DNA consisting of a fusion of *cat* and the *mazF* counterselectable marker from pGDREF (Yu et al., 2010); 3) PCR with primers oCW142 and oCW143 and template PY79 genomic DNA.

**BCW77** [*ywtFΩPxylA-mazF (cat)*] was generated by transforming PY79 with a Gibson assembly consisting of three fragments: 1) PCR with primers oCW159 and oCW161 and template PY79 genomic DNA; 2) PCR with primers oJM029 and oMK047 and template

DNA consisting of a fusion of *cat* and the *mazF* counterselectable marker from pGDREF (Yu et al., 2010); 3) PCR with primers oCW164 and oCW165 and template PY79 genomic DNA.

**BCW78** [*ywtFΩmsfGFP-ywtF*] was generated by transforming BCW77 with a Gibson assembly consisting of three fragments: 1) PCR with primers oCW160 and oCW161 and template PY79 genomic DNA; 2) PCR with primers oCW072 and oCW073 and BMD61 genomic DNA; 3) PCR with primers oCW163 and oCW165 and template PY79 genomic DNA.

**BCW79** [*yvhJΩmsfGFP-yvhJ*] was generated by transforming BCW72 with a Gibson assembly consisting of three fragments: 1) PCR with primers oCW139 and oCW146 and template PY79 genomic DNA; 2) PCR with primers oCW072 and oCW073 and BMD61 genomic DNA; 3) PCR with primers oCW143 and oCW145 and template PY79 genomic DNA.

**BCW80** [*lytRΩPxylA-mazF (cat)*] was generated by transforming PY79 with a Gibson assembly consisting of three fragments: 1) PCR with primers oCW101 and oCW109 and template PY79 genomic DNA; 2) PCR with primers oJM029 and oMK047 and template DNA consisting of a fusion of *cat* and the *mazF* counterselectable marker from pGDREF (Yu et al., 2010); 3) PCR with primers oCW100 and oCW125 and template PY79 genomic DNA.

**BCW81** [*lytRΩmsfGFP-lytR*] was generated by transforming BCW72 with a Gibson assembly consisting of three fragments: 1) PCR with primers oCW101 and oCW137 and template PY79 genomic DNA; 2) PCR with primers oCW072 and oCW073 and BMD61 genomic DNA; 3) PCR with primers oCW100 and oCW138 and template PY79 genomic DNA.

**BCW82** [*tagO::erm, ycgO::PxylA-tagO, amyE::Pspac-gfp-mreB (spec), dacA::kan*] was generated by transforming BEG300 with genomic DNA from BGL19.

**BEG202** [*tagO::erm amyE::Pxyl-gfp-mbl (spec)*] was generated by transforming BEB1451 with genomic DNA from BJS18.

**BEG281** [*ycgO::PxylA-tagO*] was generated by transforming with a plasmid created via ligating a Gibson assembly into pKM077. pKM77 was digested with EcoRI and XhoI. The assembly was created with two fragments: 1) PCR with primers oEG85 and oEG86 and template py79 genomic DNA; 2) PCR with primers oEG87 and oEG88.

**BEG291** [*tagO::erm, ycgO::PxylA-tagO*] was generated by transforming BEG281 with genomic DNA from BRB4282.



**BEG300** [*tagO::erm, ycgO::PxylA-tagO, amyE::Pspac-gfp-mreB (spec)*] was generated by transforming BEG291 with genomic DNA from BEG275.

**BMD61** [*mbl $\Omega$ mbl-msfGFP (spec)*] was generated by transforming py79 with a Gibson assembly consisting of four fragments: 1) PCR with primers oMD44 and oMD90 and template PY79 genomic DNA; 2) PCR with primers oMD47 and oMD56 and template synthetic, codon-optimized *msfGFP*; 3) PCR with primers oJM028 and oJM029 and template plasmid pWX466a (containing *spec*); 4) PCR with primers oMD48 and oMD50 and template genomic DNA.

**bSW99** [*amyE::spc-Pspac-mciZ*] was generated by transforming PY79 with a Gibson assembly consisting of five fragments: 1) PCR with primers oMD191 and oMD108 and template PY79 genomic DNA (containing upstream region of *amyE*); 2) PCR with primers oJM29 and oJM28 and template plasmid pWX466a (containing *spec*); 3) PCR with primers oMD234 and oSW76 and template plasmid pBOSE1400 (a gift from Dr. Briana Burton, containing *spec*); 4) PCR with primers oAB307 and oAB291 and template PY79 genomic DNA (containing *mciZ*); 5) PCR with primers oMD196 and oMD197 and template PY79 genomic DNA (containing downstream region of *amyE*).

**bAB343** [*tagO::erm, ycgO::cat-PxylA-tagO, amyE::spc-Pspac-mciZ, ftsAZ::ftsA-mNeonGreen-ftsZ*] was generated by transforming bAB185 (Bisson-Filho et. al, 2017) with genomic DNA from bSW99. *The resultant strain was then transformed with the genomic DNA from BEG291 and selected for Cm resistance. Subsequently, the resultant strain was transformed again with genomic DNA from BEG291, but colonies were selected for MLS resistance in the presence of 30 mM of xylose and 25 mM MgCl<sub>2</sub>.*

**bAB327** [*tagO::erm, ycgO::cat-PxylA-tagO, amyE::spc-Physpank-minCD, ftsAZ::ftsA-mNeonGreen-ftsZ*] was generated by transforming bAB185 (Bisson-Filho et. al, 2017) with genomic DNA from JB60 (a gift from Dr. Frederico Gueiros-Filho). *The resultant strain was then transformed with the genomic DNA from BEG291 and selected for Cm resistance. Subsequently, the resultant strain was transformed again with genomic DNA from BEG291, but colonies were selected for MLS resistance in the presence of 60 mM xylose and 25 mM MgCl<sub>2</sub>.*

**bAB388** [*tagO::erm, ycgO::cat-PxylA-tagO, amyE::spc-Physpank-ftsA, ftsAZ::ftsA-mNeonGreen-ftsZ*] was generated by transforming bAB199 (Bisson-Filho et. al, 2017) with genomic DNA from BEG291 and selected for Cm resistance. *Subsequently, the resultant strain was transformed again with genomic DNA from BEG291, but colonies were selected for MLS resistance in the presence of 60 mM xylose and 25 mM MgCl<sub>2</sub>.*

## Supplemental Text 1 - MreB Modeling

## Modeling predicts preferred MreB orientation and a typical cell width for losing binding orientation

Here we show that energetic modeling of an MreB filament directly binding to the inner membrane predicts the existence of both a preferred orientation of binding and a typical cell width for losing binding orientation. MreB monomers assemble into higher-order oligomers and bind directly to the inner membrane. When an MreB filament binds to the inner membrane, the combined MreB-membrane system requires an energy of deformation  $E_{def}(l_b)$  for the membrane to deviate from an equilibrium position and gains an energy of interaction  $E_{int}(l_b)$  from the hydrophobic binding. Both the deformation and interaction energies are expressed as functions of the bound MreB length,  $l_b$ . Note that the rigid cell wall imposes a boundary constraint on the cell membrane and that the equilibrium membrane configuration arises from a balance of membrane bending, turgor pressure, and cell wall confinement. If the MreB filament were to bind, the change in the total energy  $E$  of the membrane-MreB system is:

$$\Delta E = E_{def} - E_{int}. \quad (1)$$

The binding configuration that minimizes  $\Delta E$  corresponds to the one that is observed physically. We therefore wish to minimize  $\Delta E$ .

### Estimate of the hydrophobic interaction energy $E_{int}$

We assume that the biochemistry of MreB is conserved in prokaryotes so that, like *C. crescentus* and *E. coli* MreB (van den Ent, Izoré, et al. 2014), *B. subtilis* MreB is

assembled into antiparallel double protofilaments consisting of many monomeric units. Consider an MreB filament containing  $N_{int}$  interaction sites with a membrane, each with some independent and additive interaction energy  $E_{int}^0$ . Due to the antiparallel arrangement of the protofilaments (Salje et al. 2011; van den Ent, Izoré, et al. 2014), there are two binding sites per monomeric unit of MreB. We therefore estimate the number of binding sites per MreB binding length  $l_b$  as:

$$N_{int} = \frac{2l_b}{l_{MreB}}, \quad (2)$$

where  $l_{MreB} \approx 5.1$  nm is the length of a monomeric unit. The energy of burying the amino acids relevant to the binding is approximately:

$$E_{int}^0 \approx 6.04 \frac{\text{kcal}}{\text{mol}} = 10 kT, \quad (3)$$

where  $k$  denotes Boltzmann's constant and  $T$  denotes the ambient temperature; the energies of burying individual amino acids were derived from water/octanol partitioning. At a room temperature of  $T = 25^\circ\text{C}$ , the interaction energy per MreB binding length  $l_b$  is therefore:

$$\varepsilon_{int} = 2 \times 10 kT / l_{MreB} = 1.8 \times 10^{-11} \text{ J/m}, \quad (4)$$

and the hydrophobic interaction energy is:  $E_{int}(l_b) = \varepsilon_{int} l_b$ .

### Estimate of the membrane deformation energy

The membrane deformation energy  $E_{def}(l_b)$  can be decomposed as:

$$E_{def}(l_b) = E_{bend}^{MreB}(l_b) + E_{int}^{membrane}(l_b), \quad (5)$$

where  $E_{bend}^{MreB}$  denotes the bending energy of the MreB filament and  $E_{int}^{membrane}$  denotes the indentation energy of the membrane. We wish to find the MreB-membrane configuration that minimizes the sum of these terms. We prescribe the forms of these terms as follows.

### The bending energy of an MreB filament

We model an MreB filament as a cylindrical rod, with circular cross-sections of radius  $r_{MreB}$  and an intrinsic curvature  $1/R_{MreB}$ . The elastic energy density per unit length of bending a cylindrical rod of cross-sectional radius  $r_{MreB}$  from a curvature of  $1/R_{MreB}$  to a curvature of  $1/R$  is given by:

$$\varepsilon_{bend} = \frac{\pi Y_{MreB} r_{MreB}^4}{8} \left( \frac{1}{R} - \frac{1}{R_{MreB}} \right)^2 = \frac{B}{2} \left( \frac{1}{R} - \frac{1}{R_{MreB}} \right)^2, \quad (6)$$

where  $Y_{MreB}$  is the Young's modulus of an MreB filament and  $B$  is its flexural rigidity (Landau and Lifshitz, 1970). Assuming the Young's modulus of actin, we note that  $B = 1.65 \times 10^{-25} \text{ J} \cdot \text{m}$ , which is two orders of magnitude smaller than that previously assumed by Wang and Wingreen for an MreB bundle of cross-sectional radius 10 nm (S. Wang and Wingreen 2013). In particular, we assume that MreB binds to the inner membrane as pairs of protofilaments and does not bundle. For a uniform flattening of the MreB filament corresponding to  $R = \infty$ ,  $\varepsilon_{bend} \leq 8.2 \times 10^{-13} \text{ J/m}$ , which is less than the MreB-membrane interaction energy  $\varepsilon_{int}$  computed above. This suggests that an MreB filament may be susceptible to bending at our energy scale of interest. How much the MreB bends is

determined by a trade-off between the polymer bending energy and the indentation energy of the membrane, which we discuss next.

### **The membrane Hamiltonian**

We model the inner membrane as an isotropic, fluid membrane composed of a phospholipid bilayer, where there is no in-plane shear modulus and the only in-plane deformations are compressions and expansions. The membrane indentation energy can be expressed as the minimum of an energy functional over the indented states of the membrane. This functional is given by the Helfrich Hamiltonian:

$$F[S] = \int_S \left[ \frac{k_b}{2} (2H - H_s)^2 + \frac{k_t}{2} K + \gamma \right] dA + p \int_S dV, \quad (7)$$

where  $k_b$  is the bending rigidity of the membrane,  $k_t$  is the saddle-splay modulus of the membrane,  $H_s$  is the spontaneous curvature of the bilayer,  $\gamma$  is the membrane surface tension,  $p$  is the pressure differential at the membrane interface, and  $H$  and  $K$  are the mean and Gaussian curvatures of the surface  $S$ , respectively (Safran, 2003; Zhong-Can and Helfrich, 1989). The bending rigidity  $k_b$ , which depends on membrane composition, is typically 10 to 20 kT for lipid bilayers (Phillips et al., 2012). Assuming that phospholipids are in excess in the bulk and rearrange themselves on the membrane surface to accommodate areal changes (Safran, 2003), we take the membrane surface tension  $\gamma = 0$ . For large deformations of the inner membrane such as those induced by cell wall lysis (Deng, Sun, and Shaevitz 2011), the assumption that the phospholipids are in excess in the bulk may fail to hold and result in a nonzero surface tension. A nonzero surface

tension would only enhance the energetic preference of the correct binding orientation; hence, taking a finite surface tension would not change our conclusions. The mechanical energy needed to deform the membrane is the difference between the free energies in the deformed  $S$  and undeformed  $S_0$  states:

$$E_{ind}^{\text{membrane}} = F[S] - F[S_0]. \quad (8)$$

The surface integrals of the Gaussian curvature are topological invariants by the Gauss-Bonnet theorem and therefore cancel in the difference, hence:

$$E_{ind}^{\text{membrane}} = \left[ \frac{k_b}{2} \int_S (2H - H_s)^2 dA + p(\text{vol}[S]) \right] - \left[ \frac{k_b}{2} \int_S (2H_0 - H_s)^2 dA + p(\text{vol}[S_0]) \right]. \quad (9)$$

Here  $H$  denotes the mean curvature of the state  $S$ , and  $H_0$  denotes the mean curvature of the state  $S_0$ . For simplicity, we set the spontaneous curvature  $H_s = 0$ ; the case of nonvanishing spontaneous curvature can be considered in a similar manner. We therefore write:

$$E_{ind}^{\text{membrane}} = \min_S \left[ 2k_b \int_S (H^2 - H_0^2) dA + p \int dV \right], \quad (10)$$

where the volume integral is understood to be the difference of the volumes in the deformed and undeformed states and the areal change accompanying the membrane deformation is small, i.e.  $dA_0 \approx dA$ . We define the membrane bending energy  $E_{bend}^{\text{membrane}}[S; S_0]$  for a conformation  $S$  to be the former term and the membrane  $pV$  energy  $E_{pV}^{\text{membrane}}[S; S_0]$  to be the latter term in the right hand side of Equation 10.

As  $k_b$  is typically 10 to 20 kT, we take  $k_b = 10$  kT and  $p$  as a parameter of the model. Note that  $p$  denotes the pressure difference acting on the membrane. The value of  $p$  is important for determining the tradeoff between the membrane indentation energy  $E_{ind}^{membrane}$  and the MreB bending energy  $E_{bend}^{MreB}$  accurately, but we will show that the preferred orientation of MreB binding is robust over a broad range of  $p$ .

### Mechanical equilibrium of the undeformed membrane

Consider the balance of forces on the inner membrane in the undeformed state. Assuming that the undeformed membrane is a cylinder with radius  $r$  and length  $L$  and that sufficient phospholipids exist in the bulk so that  $\gamma = 0$ , the membrane free energy is

$$E(r) = 2k_b \int_S H_0^2 dA + p \int dV = \frac{\pi k_b L}{r} - \pi p L r^2, \quad (11)$$

which is monotonically decreasing in  $r$ . This implies that the membrane radius should be maximal at equilibrium. If  $p = 0$ , then the membrane should press against the cell wall and squeeze out the periplasmic space due to minimization of the bending energy. A model in which the periplasm and cytoplasm are isosmotic (Sochacki et al., 2011) with no mechanical force exerted by the periplasm is therefore inconsistent with the existence of a periplasm. For the periplasm to exist at equilibrium, it must contribute an additional energy term  $E_{peri}$  to the total energy, so that the total energy  $F = E + E_{peri}$  as a function of  $r$  has a stable fixed point at  $r_0 = r^* + \delta r^*$ . Here we define  $r^* = R_{cell} - h_{peri}$ , where  $R_{cell}$  is the radius of the cell and  $h_{peri}$  is the thickness of the periplasm, and  $\delta r^*$  as the initial deformed height where  $F'(r) = 0|_{r=r_0}$ . We consider expansions of  $E_{peri}$  and  $F(r)$  around

$r_0$ . As a function of the deviation in membrane height  $\delta r = r - r_0$ , we take  $E_{peri} \approx \kappa L(\delta r)^2$

and

$$F(\delta r) \approx \kappa^* L(\delta r)^2, \quad (12)$$

where  $\kappa^* = \kappa - p\pi$  is the effective membrane pinning modulus, which has been examined before in Wang and Wingreen's work (S. Wang and Wingreen 2013). For the stability of the fixed point at  $r_0$ , the condition that the second derivative  $F''(\delta r)$  is positive at  $\delta r = 0$  implies that  $\kappa^* \geq 0$ , or  $\kappa \geq p\pi$ . However, the validity of the expansion  $E_{peri}(\delta r) = \kappa L(\delta r)^2$  may be questionable when the deformed height due to polymer binding is larger than or comparable to  $\delta r^* \sim pr/\kappa$ . Hence, the pinning model may be invalid when  $p$  is vanishingly small. For various combinations of  $\kappa$  and the polymer bending rigidity where this double-bind is avoided, such as that assumed by Wang and Wingreen's model, the periplasm is effectively a rigid body. In this case, although a pinning potential can self-consistently penalize deviations in membrane height, it is more intuitive to take the formal limit  $\kappa \rightarrow \infty$  and treat the periplasm as undeformable. We therefore model the periplasm as a rigid, undeformable body that mechanically supports the cell membrane and imposes a boundary condition on the membrane shape. Any deviation from the equilibrium membrane shape induced by MreB binding is then resisted by the full effect of turgor. For this reason, in the following analysis we take  $p = p_{cell}$ , stipulate that the MreB cannot indent the inner membrane outwards, and do not consider the energetic contribution of  $E_{peri}$ .



### Configuration with a uniformly bent MreB filament: first-order approximation

With the membrane Hamiltonian as defined in the section above, we now see that the total membrane deformation energy is given by the sum of the MreB bending energy and the membrane indentation energy:

$$E_{def}(l_b) = E_{bend}^{MreB}(l_b) + E_{ind}^{membrane}(l_b) = \min_{R,S} \left[ \frac{B}{2} \int \left( \frac{1}{R} - \frac{1}{R_{MreB}} \right)^2 ds + 2k_b \int_S (H^2 - H_0^2) dA + p \int dV \right]. \quad (13)$$

The minimization of equation (13) over all surfaces  $S$  and MreB curvatures  $R = R(s)$  is generally difficult since minimization of the MreB bending energy determines the preferred conformation of MreB, which in turn restricts the set of surfaces  $S$  that equation (13) must be minimized over. In their work, Wang and Wingreen undertook an elegant approach to minimizing a similar combination of energies by writing the membrane indentation energy in Fourier space. Unlike a membrane pinning term, the pressure-volume energy in equation (13) does not admit a simple Fourier space representation. Nevertheless, considerable insight can be obtained by assuming that MreB bends uniformly. In this case, MreB deforms from a bent cylinder with a native curvature  $\frac{1}{R_{MreB}}$ , to a bent cylinder with a constant, membrane-bound curvature  $\frac{1}{R}$ . In the following, we will take the radius  $R$  of the bend to be a parameter in estimating the corresponding membrane indentation energy  $E_{ind}^{membrane}(l_b)$ ;  $R$  will be determined later. We will also assume that MreB binds perpendicular to the cell's long axis, so that the curvature of the membrane in its

undeformed state is simply  $\frac{1}{R_{cell}}$ , and determine the corrections due to a deviatory binding angle later.

To estimate  $E_{ind}^{membrane}$ , we first examine the energetic contribution of the region  $C$  of  $S$  directly involved in the MreB-membrane interaction. Note that the biochemical conformation of MreB, particularly, the antiparallel orientation of its protofilaments, constrains the geometry of the MreB-membrane binding interface. Since we describe the interface  $C$  as the surface of a bent cylinder with principal radii of curvature  $\frac{1}{r_{MreB}}$  and  $\frac{1}{R}$ , we have:

$$H \approx \frac{1}{2} \left( \frac{1}{r_{MreB}} + \frac{1}{R} \right), \quad A = 2\pi b r_{MreB} l_b \quad (14)$$

where  $r_{MreB}$  is the cross-sectional radius of MreB and  $b$  is the fraction of interaction along a cross-section of the MreB filament. Thus:

$$E_{bend}^{membrane}[C] \approx \pi b k_b r_{MreB} l_b \left( \frac{1}{r_{MreB}} + \frac{1}{R} \right)^2 - \pi b k_b r_{MreB} l_b \left( \frac{1}{R_{cell}} \right)^2, \quad (15)$$

where  $H_0 = 1/2R_{cell}$  and  $R_{cell}$  denoting the cell radius, is the mean curvature of the undeformed surface. The contribution of the  $pV$  energy over  $C$  can be similarly approximated by finding the area between two circles, one being the MreB filament and the other being the cross-section of a cell with radius  $R_{cell}$ , with  $R_{cell} \geq R$  as follows:

$$E_{pV}^{\text{membrane}}[C] \approx 2pr_{MreB} \int_{-R \sin(\frac{l_b}{2R})}^{R \sin(\frac{l_b}{2R})} \left( \sqrt{R_{cell}^2 - x^2} - \sqrt{R^2 - x^2} + R - R_{cell} \right) dx \approx \frac{pr_{MreB} l_b^3}{12} \left( \frac{1}{R} - \frac{1}{R_{cell}} \right), \quad (16)$$

where we have assumed that  $l_b \ll R$  and  $\frac{1}{R} \geq \frac{1}{R_{cell}}$ . This means that the approximation above is only valid for cases where the MreB filament can only bend up to a curvature  $\frac{1}{R_{cell}}$ . Now, since  $\frac{1}{R} \ll \frac{1}{r_{MreB}}$ , we deduce that the principal bending energy contribution over  $C$  arises from having the inner membrane tightly wrapped around an MreB filament. For  $k_b = 10kT$  and  $b = 1/6$ ,  $E_{bend}^{\text{membrane}}[C]$  takes on a value of:

$$E_{bend}^{\text{membrane}}[C] \approx \pi b k_b l_b \left( \frac{1}{r_{MreB}} \right) \equiv \varepsilon l_b, \quad \varepsilon = 1.0 \times 10^{-11} \text{J/m}, \quad (17)$$

which is smaller than, but comparable in scale to, the interaction energy  $E^{\text{int}}$  computed above. Writing out only the energetics of the binding region  $C$  under the uniform bending assumption, we therefore see that:

$$E_{def}(l_b) \approx \min_R \left[ \frac{B}{2} \left( \frac{1}{R} - \frac{1}{R_{MreB}} \right)^2 l_b + \frac{\pi b k_b l_b}{r_{MreB}} + \frac{pr_{MreB} l_b^3}{12} \left( \frac{1}{R} - \frac{1}{R_{cell}} \right) + \min_S F[\mathbf{H}] \right], \quad (18)$$

where the last term is the energetic contribution of the falloff region  $\mathbf{H} = S - C$ . In the case that  $\frac{1}{R} \rightarrow 0$ , estimates of the values of the first three terms in equation (18), for the parameter values summarized in Table S1, are  $10^{-19}\text{J}$ ,  $10^{-18}\text{J}$  and  $10^{-17}\text{J}$ , respectively. This means that, as MreB binds to the inner membrane, the resulting deformation will tend to minimize volumetric changes at the cost of inducing membrane curvature and filament bending. The energetic contribution of the falloff region  $\mathbf{H}$  can only be

quantitatively accounted for by explicitly finding the membrane shape, which encompasses a tradeoff between the membrane bending energy and the  $pV$  energy: the former term favors a gradual decay of the indentation, while the latter term prefers a steep decay as to minimize volume. Below, we find that it suffices to consider the case where MreB bends to match the cell curvature:  $R = R_{cell}$ . In this case, the energetic contribution of the falloff region  $H$  is vanishingly small compared to that of the binding region, since the membrane can heal in a manner in which its mean curvature is small compared to the mean curvature of the binding region. The energetic contribution of  $H$  can therefore be neglected, and we quantify it in future work.

### **$\Delta E$ for the pure bending of an MreB filament**

By examining the form of the energetics just over the region  $C$ , we note that the inclusion of a large pressure  $p$  increases the energetic preference of an MreB filament binding perpendicular to the cellular long axis.

Consider a case where  $p \geq p^*$  for some  $p^*$  to be determined, so that it is energetically unfavorable to displace the membrane volume as opposed to bending the MreB filament. In this case, as discussed above, the energetic contribution of the falloff region  $H$  can be neglected, and an estimate for the minimal value of such a pressure can be obtained by requiring that:

$$E_{def}(l_b) \approx \min_R \left[ \frac{B}{2} \left( \frac{1}{R} - \frac{1}{R_{MreB}} \right)^2 l_b + \frac{\pi b k_b l_b}{r_{MreB}} + \frac{p r_{MreB} l_b^3}{12} \left( \frac{1}{R} - \frac{1}{R_{cell}} \right) \right] \quad (19)$$

as a function of  $R$ , be minimal at  $R_{cell}$ . For the numerical values relevant to MreB above and summarized in Table S1, this indicates that:

$$p^* \approx \frac{12B}{r_{MreB}l_b^2} \left( \frac{1}{R_{MreB}} - \frac{1}{R_{cell}} \right) \approx 20 \text{ kPa}, \quad (20)$$

which is 1/100<sup>th</sup> of the turgor pressure of *B. subtilis*. In this case, assuming  $R = R_{cell}$ ,

$$\Delta E(l_b) \approx \left[ \frac{B}{2} \left( \frac{1}{R} - \frac{1}{R_{MreB}} \right)^2 + \frac{\pi b k_b}{r_{MreB}} - \varepsilon_{int} \right] l_b, \quad (21)$$

The energetic dependence on  $R_{cell}$  is then manifested through the pure bending of MreB when binding to the inner membrane: in particular, we may assume that the MreB filament will always bend to attain a curvature matching that of the cell's (although small deviations in the membrane height may lead to an even lower energy conformation), and the energetic contribution of the falloff region  $H$  can be neglected.

If  $p < p^*$ , note that both the membrane and the MreB filament can deform each other in a manner that minimizes the total energy, with the membrane shape determined by the geometry of the falloff region  $H$ . For vesicles with a pressure gradient  $p \approx 0$ , the fact that an MreB filament grossly deforms the membrane and generates membrane curvature (Salje et al. 2011) is predicted by the shape of  $H$ . For  $p \approx 0$ , it can also be shown that the energetic difference between MreB binding at  $R_{cell} = 500 \text{ nm}$  and  $R_{cell} = 3000 \text{ nm}$  is on the order of several  $kT$ , and so a perpendicular alignment of MreB filaments may also be energetically favorable. For simplicity, in the following discussion we shall consider the wild-type cell scenario, where  $p = p_{cell} > p^*$ , so that only the pure bending of MreB and

the associated membrane bending energy need to be considered in  $\Delta E$ . We will therefore assume the form of equation (21) for  $\Delta E$  in the discussion that follows.

### **Preferred orientation of MreB binding**

Equations (19) and (21) describe the change in free energy due to MreB binding at a perpendicular angle and bending completely to match the curvature  $\frac{1}{R_{cell}}$  of the cell membrane at this angle. Our modeling then predicts that MreB filaments tend to bind at an angle of  $\theta = 90^\circ$  relative to the long axis of *B. subtilis*: at any deviatory angle  $|\theta - 90^\circ| > 0^\circ$ , the leading-order correction to the cell radius  $R_{cell}$  in the MreB bending energy is a multiplicative factor of  $1/\cos \theta$ , which monotonically increases the MreB bending energy. Since the MreB bending energy is minimal when the principal axis of curvature of the MreB filament matches that of the cell and the curvature of the cell is maximal at a perpendicular binding angle, the angle distribution is symmetric about a minimum centered at  $\theta = 90^\circ$ . This reasoning suggests the existence of a potential well centered at  $\theta = 90^\circ$ , as shown in Figure 2.4G under the simplifying assumption that  $b = 0$ . The depth of this potential well is on the order of tens of  $kT$ , which appears to be a large enough energetic preference as to be robust to sources of stochasticity such as thermal fluctuations. Furthermore, our discussion shows that membrane binding energetics, and in particular the pure bending of an MreB filament, may complement the conjecture in Salje *et al.*'s work that the membrane insertion loop and amphipathic helix help ensure orthogonal membrane binding (Salje *et al.* 2011).

A sensitivity analysis shows that the energetic difference of an MreB filament perpendicularly binding to a region of ambient curvature  $R_{cell} = 0.5 \mu\text{m}$  and  $R_{cell} = 1.5 \mu\text{m}$  is still on the order of tens of  $kT$  over a wide range of binding energy and flexural rigidity values, as shown in Figure 2.4H. Thus, we anticipate the alignment to be robust to changes in these two parameters.

### **A typical cell radius for losing orientation**

Our modeling shows that the depth of the potential well in  $\theta$  is inversely related to  $R_{cell}$ , so that at larger cell diameters the angle distribution becomes more uniform. Varying the cell radius  $R_{cell}$  from 0.5 microns to 3.0 microns results in a reduction of the depth of the potential well, as illustrated in Figure 2.4G. We therefore anticipate MreB filaments to bind with more variance in angle for higher values of  $R_{cell}$ , consistent with the existence of a typical radius at which the binding angle becomes less robust and affected by factors such as thermal fluctuations or other sources of stochasticity.

### **Binding orientation at regions of different Gaussian curvatures**

Our modeling predicts that, in live cells, MreB filaments will bend to conform to the shape of the inner membrane. Since the binding sites are located at the outer edge of a curved MreB filament, our modeling also predicts that the binding angle distribution becomes narrower at regions of negative Gaussian curvature: to bind in a conformation that deviates significantly from the preferred binding orientation, in which the filament's deformed curvature remains of the same sign as its intrinsic curvature, an MreB filament

must bend to the extent that its curvature flips sign. Similarly, at regions of positive Gaussian curvature, the binding angle distribution will be less narrow. Representative binding angle distributions are shown in three cases of positive, vanishing, and negative Gaussian curvatures in Fig. 2.7B of the main text.

## **Supplemental Text 2 – Localization of WTA ligases and WTAs**

In order to understand how wall teichoic acid (WTA) depletion and recovery affects cell shape, we observed the spatial localization of WTAs and the extracellular ligases (the genes *lytR*, *yvhJ*, and *ywtF* (Kawai et al. 2011)) that determine their attachment to the cell wall. Previous work has suggested that YwtF and LytR localize in MreB-like patterns (Kawai et al. 2011) and associate with MreB (assayed by *in vivo* crosslinking and tandem affinity purification). We reasoned that if the synthesis or insertion of WTAs is MreB associated, then the emergence of discrete rod-shaped cells upon *tagO* repletion might correlate with preferential WTA insertion at the emerging rod, where MreB shows oriented motion. To test this, we examined 1) the localization and dynamics of fluorescent tagged WTA ligases, and 2) the spatial localization of WTAs in cells recovering from spheres into rods. We constructed sfGFP fusions to each of the WTA ligases under their native promoters, and examined their localization using TIRF and epifluorescent illumination. Although we did observe variation in ligase intensity around the cell periphery under epifluorescent illumination, we did not see any characteristic banding across the cell surface as is seen with MreB using TIRF microscopy (Fig. S6C). Furthermore, TIRF imaging of these fusions at different frame rates did not show any directional motions,



indicating they are not moving along with MreB filaments; rather these motions suggested the WTA ligases were diffusing on the cell membrane (Movie S9). We cannot rule out the possibility that the WTA ligases interact with MreB through transient associations.

We next explored the localization of WTAs, using fluorescently labeled Concanavalin A (ConA). ConA is a sugar-binding protein with specific affinity for  $\alpha$ -D-glucose, which decorates WTA polymers. ConA has previously been used to localize WTAs (Birdsell et al., 1975; Doyle et al., 1975). The gene *tagE* encodes the glycosylase that adds  $\alpha$ -D-glucose to WTA molecules (Allison et al., 2011), which is recognized by ConA. ConA staining of cells deleted for *tagE* shows no staining (Fig. S6A), verifying the specificity of ConA for WTAs over other surface sugars. We then used this probe to examine WTA localizations during recoveries. Addition of ConA to WTA-depleted cells in bulk culture shows very little staining at the cell periphery, consistent with a basal level of WTA expression; induction of *tagO* results in a dramatically increased intensity of staining. Even at early time points, when rod-shaped cells are just starting to appear in the population, WTA staining is relatively uniform, with no patterns reminiscent of the patchy distribution of MreB (Fig. S6B). Together, this data indicates that WTA ligases and WTA incorporation occur uniformly around the cell in both wild type cells as well as in TagO depleted spheres recovering into rods. These findings suggest that the changes in activity of TagO that cause the loss of rod shape (or the reformation thereof) occur uniformly around the cell wall. Furthermore, these findings also suggest that the WTA ligases do not consistently localize to MreB within *B. subtilis*.

## Supplemental Movie Legends

**SM1. Related to Figure 2.1C** - Movie showing the trajectories taken by Mbl filaments frequently cross each other close in time. BDR2061, containing GFP-Mbl expressed at the native locus under a xylose-inducible promoter, was induced with 10 mM xylose and imaged with TIRFM. Frames are 1 s apart. Scale bar is 5  $\mu$ m.

**SM2A. Related to Figure 2.2A – (*first sequence*)** Timelapse showing circumferential motions of GFP-MreB in rod shaped cells with high TagO expression (BEG300 with 30 mM xylose, and GFP-MreB induced with 50  $\mu$ M IPTG) (***second sequence***) Timelapse of GFP-MreB trajectories in equivalent conditions. (***third sequence***) Timelapse showing isotropic motions of GFP-Mbl in a *tagO* knock out strain (BEG202, GFP-Mbl was induced with 0.125 mM xylose). (***fourth sequence***) Timelapse of GFP-Mbl trajectories in equivalent conditions as above. Frames are 1 s apart in the first and second sequences, 2 s apart in the third and fourth. All Scale bars are 1  $\mu$ m.

**SM2B. Related to Figure 2.2C – (*top*)** Timelapse of GFP-Mbl trajectories occurring 2 hours after the initiation of Pbp2a depletion (***middle and bottom***). Timelapse of GFP-Mbl trajectories occurring 3 hours after initiation of Pbp2a depletion, where cells become a mixture of rod shaped and round cells. GFP-Mbl shows a mixture of circumferential (bottom) and isotropic (middle) motion. BRB785 was grown in 1 mM IPTG, washed, then

grown in media lacking IPTG. Cells were placed under a pad at the indicated times, and imaged with spinning disk confocal. Frames are 5 s apart. Scale bar is 2.5  $\mu\text{m}$ .

**SM3. Related to Figure 2.3A-C** - Timelapse showing circumferential motion of GFP-MreB in BEG300 induced at low TagO levels (2 mM xylose) when confined into long 1.5 x 1.5  $\mu\text{m}$  channels. GFP-MreB was induced with 50  $\mu\text{M}$  IPTG. Frames are 2 s apart. Scale bar is 5  $\mu\text{m}$ .

**SM4. Related to Figure 2.3D-F** – Timelapse of GFP-Mbl in protoplasted cells showing Mbl does not move directionally. BJS18 (containing GFP-Mbl expressed at an ectopic site under xylose control) was induced with 30 mM xylose. Cells were then protoplasted in SMM and grown in molds as detailed in methods. Frames are 1 s apart. Scale bar is 5  $\mu\text{m}$ . Movie was gamma-adjusted,  $\gamma = 0.8$ .

**SM5. Related to Figure 2.4 – (first sequence)** PyMOL volume rendering of an electron cryotomography 3D map of *T. maritima* MreB included in a liposome (corresponds to liposome depicted in Fig. 4E. **(second sequence)** Typical field view of an MreB liposome reconstitution experiment. The movie scans through consecutive Z-layers of the tomographic 3D reconstruction. Note that the smaller, round liposomes trapped inside the rod-shaped liposomes are not decorated with MreB filaments. **(third sequence)** Cryotomogram of *T. maritima* MreB(V109E) inside a liposome. The mutant shows less bundling of MreB filaments, but filament orientation is still skewed towards high angles,

generally preferring an orientation perpendicular to the long axis of the rod-shaped liposome (corresponds to Fig. 4B).

**SM6. Related to Figure 2.5 – (top and middle)** Timelapses showing the local recovery of rod shape upon TagO reinduction from depleted cells. Note the relatively fast growth of rods compared to parent spheres. BEG300 was grown in media lacking xylose, then either loaded into a cellASIC device (top row) or placed under an agar pad (middle row). Both rows were shifted to 30 mM xylose to induce rod-shape recovery, prior to image acquisition. Frames are 10 min apart. Scale bar is 5  $\mu$ m.

**(bottom)** Timelapse showing the local recovery of rod shape upon Pbp2a reinduction from cells depleted of Pbp2a/PbpH. BRB785 was grown media lacking IPTG for 4.5 hours, then placed on a pad with 1 mM IPTG before the start of imaging. Frames are 5 min apart. Scale bar is 5  $\mu$ m.

**SM7. Related to Figure 2.5 and 2.6 –** Timelapse of rod shape recoveries showing that circumferential MreB-GFP motion A) occurs immediately upon the formation of rod shape, and B) that circumferential motion only occurs in rod-shaped cells, even while attached non-rod cells show unaligned motion. BEG300 was grown overnight in 0mM xylose to deplete TagO. Cells were then loaded into a cellASIC chamber and grown in the same media with 1 mM IPTG to induce GFP-MreB. Prior to imaging, *tagO* expression was reinduced by switching media to contain 30mM xylose. GFP-MreB was imaged with

TIRFM. Frames are 2 s apart in the fluorescent channel (green) and 10 min apart in the phase contrast channel (grayscale). Scale bar is 5  $\mu\text{m}$ .

**SM8. Related to Figure 2.5** – Timelapse showing the loss and recovery of rod shape in cells with intermediate TagO levels when magnesium is removed and added back to the medium. BCW51 was grown in LB supplemented with 8 mM xylose and 20 mM magnesium, then loaded into a cellASIC chamber, and grown in the same media for 30 minutes. At the start of the video the media is switched to contain 0 mM magnesium, causing the cells to lose rod shape. At 4:00:00 the media is switched to contain 20 mM magnesium where the cells revert back into rod-shaped cells. Frames are 20 min apart. Scale bar is 1  $\mu\text{m}$ .

**SM9. Related to Figure 2.6B** – Timelapse showing that the teichoic acid ligases TagTUV do not move circumferentially. Strains shown are BMD61, BCW81, BCW79 and BCW78, where Mbl, TagU (LytR), TagV (YvhJ), and TagT (YwtF) respectively are fused to msfGFP, and expressed from their native promoters. Cells were grown in CH medium and imaged using TIRF illumination every 100 ms. Scale bar is 5  $\mu\text{m}$ .

## Supplemental Tables

**Table S1: Model Parameters. Related to Figure 2.4 and Supplemental Text 1.**

Quantity	Estimate	Source
<b>MreB values</b>		
MreB bound length $l_b$	220 nm	This work
MreB monomer length $l_{MreB}$	51 angstroms	(van den Ent, Izoré, et al. 2014)
MreB cross-sectional radius $r_{MreB}$	3.2 nm	(van den Ent, Izoré, et al. 2014)
MreB wild-type principal radius of curvature $R_{MreB}$	300 nm	This work
MreB Young's modulus $Y_{MreB}$	Similar to actin; 2 GPa	(Kojima et al., 1994)
MreB cross-sectional binding fraction $b$	0	This work
<b>Cell values</b>		
<i>B. subtilis</i> periplasm thickness $h_{peri}$	22 nm	(Matias and Beveridge 2005)
<i>B. subtilis</i> cross-sectional radius $R_{cell}$	500 nm	This work
<i>B. subtilis</i> internal turgor pressure $p_{cell}$	20 atm	(Whatmore and Reed, 1990)
<b>Binding energy values</b>		
Unit MreB-cell membrane interaction energy $E_{int}^0$	10 kT	This work
Absolute temperature $T$	300 K	This work
<i>B. subtilis</i> typical cross-sectional radius $R_{cell}^*$ for losing shape	about 1-1.5 microns	This work

**Table S2 – Strains used in this study**

Strain	Genotype (all strains are Py79 unless otherwise noted)	Source
BCW51	<i>ycgO::Pxyl-tagO, tagO::erm, amyE::sfGFP-mreB, sinR::phleo</i>	This work
BCW61	<i>tagE::erm</i>	This work
BCW72	<i>yvhJΩPxylA-mazF (cat)</i>	This work
BCW77	<i>ywtFΩPxylA-mazF (cat)</i>	This work
BCW78	<i>ywtFΩmsfGFP-ywtF</i>	This work
BCW79	<i>yvhJΩmsfGFP-yvhJ</i>	This work
BCW80	<i>lytRΩPxylA-mazF (cat)</i>	This work
BCW81	<i>lytRΩmsfGFP-lytR</i>	This work
BCW82	<i>tagO::erm, ycgO::PxylA-tagO, amyE::Pspac-gfp-mreB (spec), dacA::kan</i>	This work
BDR2061	<i>amyE::PxylA-gfp-mbl (spec), mblΩpMUTIN4 (erm)</i>	(Carballido-Lopez and Errington, 2003)
BEB1451	<i>hisA1 argC4 metC3 tagO::erm</i>	(D'Elia et al. 2006)

<b>Table S2 (Continued)</b>		
BJS18	<i>amyE::PxylA-gfp-mbl (spec)</i>	(Defeu Soufo and Graumann 2004)
BMD61	<i>mblΩmbl-msfGFP (spec)</i>	This work
BRB785	<i>yhdG::Pspank-pbpA (phleo), pbpH::spec, pbpA::erm, mblΩPxylA-gfp-mbl (cat)</i>	(Garner et al. 2011)
BEG202	<i>ΔtagO::erm amyE::Pxyl-gfp-mbl (spec)</i>	(Kawai et al. 2011)
BEG281	<i>ycgO::PxylA-tagO</i>	This work
BEG291	<i>tagO::erm, ycgO::PxylA-tagO,</i>	This work
BEG275	<i>amyE::Pspac-gfp-mreB (spec)</i>	(Billings et al., 2014)
BEG300	<i>tagO::erm, ycgO::PxylA-tagO, amyE::Pspac-gfp-mreB (spec),</i>	This work
BRB4282	<i>168 trpC2 ΔtagO::erm</i>	(D'Elia et al. 2006)
bAB343	<i>ftsZΩmNeonGreen-15aa-ftsZ, amyE::spc-Pspank-mciZ, ycgO::cat-Pxyl-tagO, tagO::erm</i>	This work
bAB327	<i>ftsZΩmNeonGreen-15aa-ftsZ, amyE::Phyperspank-minCD, ycgO::Pxyl-tagO, tagO::erm</i>	This work
bAB388	<i>ftsZΩmNeonGreen-15aa-ftsZ, amyE::Physpank-ftsA ycgO::cat-Pxyl-tagO, tagO::erm</i>	This work

**Table S3 – Oligonucleotides used in this study**

Primer	Sequence
oCW054	TGCAATTCAGGGTTGACTG
oCW055	ATACGAACGGTACTGAGCGAGGGAGCAGAACGGCATCTAGAATATATGATCATTG
oCW056	ACTTATTAATAATTTATAGCTATTGAAAAGAGAT
oCW057	TTTTCAATAGCTATAAATTATTTAATAAGTCTTGGAGGGTCACGGAAATAAA
oCW058	TTTCATCCTTGTTCAGGCTA
oCW072	ATGCGAAAAGGGGAAGAATTGTTTA
oCW073	GCCGCTTCCTTGGCCTGA
oCW100	TCCGTATGGAGATGGAGAGG
oCW101	CCGCTTATCCTTTTCACAGC
oCW109	ATACGAACGGTAGTTGACCAGTGCTCCCTGCCTTTGCACCTCGTCTGTTAAAT
oCW125	AAAATTAACGTAAGTATTGGGTAGTCTAGAATGAGAAACGAACGCAGAAAAAAG
oCW137	GCCTGTAAACAATTCTTCCCTTTTCGCATCCTTTGCACCTCGTCTGTTAAAT
oCW138	CAGGGACCGGGCTCAGGCCAAGGAAGCGGCATGAGAAACGAACGCAGAAAAA G
oCW139	ATAAACGGTTTCTCGCATGG
oCW141	ATACGAACGGTAGTTGACCAGTGCTCCCTGTTATTCAGTCTCCTTTATGTGATTGA
oCW142	AAAATTAACGTAAGTATTGGGTAGTCTAGAATGGCTGAACGCGTTAGAGTG
oCW143	GAGCTGTACGTCCTGCTTC
oCW145	CAGGGACCGGGCTCAGGCCAAGGAAGCGGCATGGCTGAACGCGTTAGAGTG
oCW146	GCCTGTAAACAATTCTTCCCTTTTCGCATTATTCAGTCTCCTTTATGTGATTGAC
oCW159	ATACGAACGGTAGTTGACCAGTGCTCCCTGATATCAATACCTCACGTTTCTTTAAT ATTT

**Table S3 (Continued)**

oCW160	GCCTGTAAACAATTCTTCCCCTTTTCGCATATATCAATACCTCACGTTTCTTTAATA TTT
oCW161	CTTTGCTTTCTTCGCCATTC
oCW163	CAGGGACCGGGCTCAGGCCAAGGAAGCGGCATGGAAGAACGATCACAGCGC
oCW164	AAAATTAACGTACTGATTGGGTAGTCTAGAATGGAAGAACGATCACAGCGC
oCW165	CGCCATCCCGTTCATTATAC
oMD44	AATTCTCGAAGGAGAGCCTGTTC
oMD47	TGATTTACAAACCTCATTCTGAAAAAGAATGAGGTTTTTTTATGAAAAATTCTGCT CCCTCGCTCAG
oMD48	CGTCATTTAACATCTTTTCGTGAAGGCCAGGGAGCACTGGTCAAC
oMD50	CGTGAACCTCATCATCGCTCC
oMD56	TTCTTTTTCAGAATGAGTTTTGTGAAATCATTTGTAAAGTTCATCCATTCCATGCG
oMD90	TGGCCAGGGACCGGGCTCAGGCCAAGGAAGCGGCATGCGAAAAGGGGAAGAAT TGTTTAC
oMD108	ACGAACGGTAGTTGACCAGTGCTCCCTGTCTTGACACTCCTTATTTGATTTTTTGA AGAC
oMD191	TTTGGATGGATTCAGCCCGATTG
oMD196	GGGCAAGGCTAGACGGG
oMD197	TCACATACTCGTTTCAAACGGATC
oMD234	ATACGAACGGTACTGAGCGAGGGAGCAGAATAATGGATTTCTTACGCGAAATAC G
oEG85	GAGAGCTTGATGTCACAAGCAGCTGGGAAGGAATTCGTGCCATGTCACTATTGCT
oEG86	ATAAAGAAGTCTCCTTTGGACTCGAGGCATTCAAATACAGATGCATTTTATTTCATA
oEG87	TGAAATAAAATGCATCTGTATTTGAATGCCTCGAGTCCAAAGGAGACTTCTTTATG CTTG
oEG88	AATAAGGGTAACTATTGCCGTATGGGATCCATGCTAGCTTAATTCCTTTTCACCAG CCG
oJM028	TTCTGCTCCCTCGCTCAG
oJM029	CAGGGAGCACTGGTCAAC
oMK047	TCTAGACTACCCAATCAGTACGTT
Sinr_up_F	CAGTTGAAATGGACAAACAAATC
Sinr_up_R	ACTGAGCGAGGGAGCAGAAGTGTCATCACCTTCCTTG
Sinr_DOWN_F	GTTGACCAGTGCTCCCTGTGCCTGAGCAGAGGC
Sinr_DOWN_R	GGACAGCACCATGTCTACTTAAC
oSW76	TAGATCACCTCCTTAAGCTT
oAB291	CGGTAAGTCCCCTAGCCTTGCCCTTATGGCTTTGAGATCCAATCTTT
oAB307	CAATTAAGCTTAAGGAGGTGATCTAGTGAAAGTGCACCGCATGCC

## Supplementary materials for Chapter 3

### Movie Legend

**S10** - Both mutant MreBL268F and wtMreB show shape defects in a double knockout of *mreB* and *mbi*. Strain BSH31 (first part), with sfGFP-MreBL268F and BSH34 (second part), with sfGFP-MreBwt are induced at 100  $\mu$ M IPTG and imaged using total internal



reflection microscopy at 1 sec intervals. Circumferential MreB motion can be seen in rod-like cells with mutant MreB.

**Table 1 - Strains used**

Strain	Genotype (all strains are Py79 unless otherwise noted)	Source
bSH14	amyE::erm GFP - MreBmutant L268F	This work
bSH15	amyE::erm GFP - MreBmutant I279F	This work
bSH16	amyE::erm pspac - GFP-MreBmutant M306F	This work
bSH21	amyE::erm pspac- GFP - megateriumMreBmutant L268F	This work
bSH22	amyE::erm pspac- GFP - megateriumMreBmutant I279F	This work
bSH23	amyE::erm pspac- GFP - megateriumMreBmutant M306F	This work
bSH24	amyE::erm pspac- GFP - megateriumMreB	This work
bSH25	amyE::erm pspac- GFP - MreB	This work
bSH27	$\Delta$ mreB amyE::erm pspac- GFP - MreBmutant L268F	This work
bSH28	$\Delta$ mreB amyE::erm pspac- GFP - MreBmutant I279F	This work
bSH29	$\Delta$ mreB amyE::erm pspac- GFP - MreBmutant M306F	This work
bSH30	$\Delta$ mreB mbl::cat amyE::erm pspac- GFP - MreBmutant L268F	This work
bSH31	$\Delta$ mreB mbl::cat amyE::erm pspac- GFP - MreBmutant I279F	This work
bSH32	$\Delta$ mreB mbl::cat amyE::erm pspac- GFP - MreBmutant M306F	This work
bSH33	$\Delta$ mreB amyE::erm pspac- GFP - MreBwt	This work
bSH34	$\Delta$ mreB mbl::cat amyE::erm pspac- GFP - MreBwt	This work

**Table 2 - Primers used**

oSH008	ATAACAATTAAGCTTTAAGGAGGAACCTACCATATGAGTAAAGGAGAAGAAGCTTTTCACT
oSH009	AGGCGGTGTTTTTTTCGAATGTGCTCTTCACTGCTTCGACAAT
oSH010	GTGAAGAGCACATTTCGAAAAACACCGCCTGAGCTT
oSH011	ACCTCTGTCCATGAAATCTGCTGCAAGCTCAGGC
oSH012	GAGCTTGCAGCAGATTTTCATGGACAGAGGTATAGTGTTAACC
oSH013	GATAAGGACCGGGAATTTTGTTCCTTCGCTGATGACTTTGT
oSH014	AGCGAAGAAACAAAATTCCCGGTCCTTATCGCCGAA
oSH015	GGGCCCGTGGATCCGAA
oSH016	AGGCTACCTTTAATGAACCCG
oSH017	AGGCGGTGTTTTTTTCGAGTGTGCTCTTCACTGCTTCGACAATTGTAGATACAGT
oSH018	GTGAAGAGCACACTCGAAAAACACCGCCTGAGCTTGCAGCAGATATCATG
oMD191	TTTGATGGATTAGCCCGATTG
oMD232	TCCTTTCGGGCTTTGTTAGCAGCCGGATCTTATCTAGTTTTCCCTTTGAAAAGATGGATG
oMD197	TCACATACTCGTTTCCAAACGGATC
oMD38	CATCCCGGAAATCTGCAAGC
oMD41	TTTCATCAACCTGATCGAATTGCTG

## **gBlocks used**

### *B. megaterium* MreBI279F

AAAATGTCCAGACTTCGGATCCACGGGCCCATGTTTGAATCGGTAAGACTAGAGACCTTGAATAGATTTGG  
GTAAGTACGCTCGTTTATGTAAAAGGAAAAGGAATTGTTGTGCGTGAGCCGTCTGTTGTGGCTTTG  
CAAAGTACAAAACAAATCGTTGCGGTAGGTAACGATGCAAAAAATATGATTGGTCGTACACCTGGGAA  
CGTAGTAGCCCTTCGTCCAATGAAAGATGGAGTTATTGCAGATTACGAAACAACCTGCGACGATGATGAAAT  
ATTACATCAATCAAGCTCAAAAAACAAAAAGTTTGTTCGCGGTAAGCCGTATGTAATGGTTTGTGTACCTT  
CTGGCATTACAGCTGTTGAGAAACGTGCCGTTATTGATGCGACTCGTCAGGCTGGCGCGCGTATGCGTA  
TACAATTGAAGAACCGTTTGTCTGCAGCAATCGGCGCCAATCTACCGGTCTGGGAGCCAACGGGAAGTATG  
GTAGTAGACATTGGCGGAGGAACAACAGAAGTTGCGATTATTTCTTTAGGAGGAATCGTAACATGTCAGTC  
AATCCGTATCGCTGGGACGAGATGGATGAAGCGATTATTCAATATATTTCGCAAGAATTATAATTTAATGAT  
CGGTGAGCGTACGTGAGAAGCATTAAAAGTAGAAGTCGGTTCTGCCGGAATTCAGAAGGTATTGAAAAC  
ATGGAAATTCGCGGACGTGACTTACTAACAGGTCTACCGAAAACAATCGAAATTTAGCAGAAGAAATTGC  
AGAAGCGCTAAAAGATACAGTGGCTTCTATTGTAGATTACAGTAAAAGTACATTAGAAAAACACCACCTGA  
ACTTGCAGCAGATTTTATGGATCGCGGTATTGTATTAACAGGCGGTGGCGCATTGCTACGTAATTTAGATA  
AAGTTATTAGTGAAGAAACAAATATGCCGTTGTATCGCAGAAGATCCGCTTACTGTGTTGCAATTTGGG  
ACTGGTAAAGCGTTAGAACACATTGATTTATTTAAAAATCGTACAAGCGATTTCATATCGCTAAATATTAAGA  
GGTGTAGATCGTGCCACAATTTTTCTTAAATAAACGTTTGTAGTTATTTTATTAGTCAGTATTATTGTATTAGT  
GCATTGATTGGTTTTTTCGTTAAATGGTCGTAAAATGTAACGTGGCCTGAACAGTTTGTCAAAGATACGGT  
GGTCTTGTTCAGGCTACCTTTAATGAACCCGCACAATTTG

### *B. megaterium* MreBL268F

AAAATGTCCAGACTTCGGATCCACGGGCCCATGTTTGAATCGGTAAGACTAGAGACCTTGAATAGATTTGG  
GTAAGTACGCTCGTTTATGTAAAAGGAAAAGGAATTGTTGTGCGTGAGCCGTCTGTTGTGGCTTTG  
CAAAGTACAAAACAAATCGTTGCGGTAGGTAACGATGCAAAAAATATGATTGGTCGTACACCTGGGAA  
CGTAGTAGCCCTTCGTCCAATGAAAGATGGAGTTATTGCAGATTACGAAACAACCTGCGACGATGATGAAAT  
ATTACATCAATCAAGCTCAAAAAACAAAAAGTTTGTTCGCGGTAAGCCGTATGTAATGGTTTGTGTACCTT  
CTGGCATTACAGCTGTTGAGAAACGTGCCGTTATTGATGCGACTCGTCAGGCTGGCGCGCGTATGCGTA  
TACAATTGAAGAACCGTTTGTCTGCAGCAATCGGCGCCAATCTACCGGTCTGGGAGCCAACGGGAAGTATG  
GTAGTAGACATTGGCGGAGGAACAACAGAAGTTGCGATTATTTCTTTAGGAGGAATCGTAACATGTCAGTC  
AATCCGTATCGCTGGGACGAGATGGATGAAGCGATTATTCAATATATTTCGCAAGAATTATAATTTAATGAT  
CGGTGAGCGTACGTGAGAAGCATTAAAAGTAGAAGTCGGTTCTGCCGGAATTCAGAAGGTATTGAAAAC  
ATGGAAATTCGCGGACGTGACTTACTAACAGGTCTACCGAAAACAATCGAAATTTAGCAGAAGAAATTGC  
AGAAGCGCTAAAAGATACAGTGGCTTCTATTGTAGATTACAGTAAAAGTACATTGAAAAACACCACCTG  
AACTTGCAGCAGATATTATGGATCGCGGTATTGTATTAACAGGCGGTGGCGCATTGCTACGTAATTTAGAT  
AAAGTTATTAGTGAAGAAACAAATATGCCGTTGTATCGCAGAAGATCCGCTTACTGTGTTGCAATTTGG  
GACTGGTAAAGCGTTAGAACACATTGATTTATTTAAAAATCGTACAAGCGATTTCATATCGCTAAATATTAAG  
AGGTGTAGATCGTGCCACAATTTTTCTTAAATAAACGTTTGTAGTTATTTTATTAGTCAGTATTATTGTATTAGT  
GGCATTGATTGGTTTTTTCGTTAAATGGTCGTAAAATGTAACGTGGCCTGAACAGTTTGTCAAAGATACGG  
TTGGTCTTGTTCAGGCTACCTTTAATGAACCCGCACAATTTG

### *B. megaterium* MreBM306F

AAAATGTCCAGACTTCGGATCCACGGGCCCATGTTTGAATCGGTAAGACTAGAGACCTTGAATAGATTTGG  
GTAAGTACGCTCGTTTATGTAAAAGGAAAAGGAATTGTTGTGCGTGAGCCGTCTGTTGTGGCTTTG  
CAAAGTACAAAACAAATCGTTGCGGTAGGTAACGATGCAAAAAATATGATTGGTCGTACACCTGGGAA

CGTAGTAGCCCTTCGTCCAATGAAAGATGGAGTTATTGCAGATTACGAAACAACCTGCGACGATGATGAAAT  
ATTACATCAATCAAGCTCAAAAAACAAAAAGTTTGTTCGCGGGTAAGCCGTATGTAATGGTTTGTGTACCTT  
CTGGCATTACAGCTGTTGAGAAACGTGCCGTTATTGATGCGACTCGTCAGGCTGGCGCGCGTGATGCGTA  
TACAATTGAAGAACCGTTTGCTGCAGCAATCGGCGCCAATCTACCGGTCTGGGAGCCAACGGGAAGTATG  
GTAGTAGACATTGGCGGAGGAACAACAGAAGTTGCGATTATTTCTTTAGGAGGAATCGTAACATGTCAGTC  
AATCCGTATCGCTGGGGACGAGATGGATGAAGCGATTATTCAATATATTCGCAAGAATTATAATTTAATGAT  
CGGTGAGCGTACGTGAGAAGCATTAAAAGTAGAAGTCGGTTCTGCCGGAATTCAGAAGGTATTGAAAAC  
ATGGAAATTCGCGGACGTGACTTACTAACAGGTCTACCGAAAACAATCGAAATTTAGCAGAAGAAATTGC  
AGAAGCGCTAAAAGATACAGTGGCTTCTATTGTAGATTGAGTAAAAGTACATTAGAAAAACACCACCTGA  
ACTTGCGGCAGATATTATGGATCGCGGTATTGTATTAACAGGCGGTGGCGCATTGCTACGTAATTTAGATA  
AAGTTATTAGTGAAGAAACAAATTTCCCGGTTGTCATCGCAGAAGATCCGCTTGACTGTGTTGCAATTGGG  
ACTGGTAAAGCGTTAGAACACATTGATTTATTTAAAAATCGTACAAGCGATTCATATCGCTAAATATTAAGA  
GGTGTAGATCGTGCCACAATTTTTCTTAAATAAACGTTTAGTTATTTTATTAGTCAGTATTATTGTATTAGTG  
GCATTGATTGGTTTTTCGTTAAATGGTCGTAAAAATGTAACGTGGCCTGAACAGTTTGTCAAAGATACGGTT  
GGTCTTGTTGAGGCTACCTTTAATGAACCCGCACAATTTG

## *B. megaterium* MreB

AAAATGTCCAGACTTCGGATCCACGGGCCCATGTTTGAATCGGTAAGACTAGAGACCTTGAATAGATTTGG  
GTACTGCAAATACGCTCGTTTATGTAAGGAAAAGGAATTGTTGTGCGTGAGCCGTCTGTTGTGGCTTTG  
CAAAGTATACAAAACAAATCGTTGCCGTTAGGTAACGATGCAAAAAATATGATTGGTCGTACACCTGGGAA  
CGTAGTAGCCCTTCGTCCAATGAAAGATGGAGTTATTGCAGATTACGAAACAACCTGCGACGATGATGAAAT  
ATTACATCAATCAAGCTCAAAAAACAAAAAGTTTGTTCGCGGGTAAGCCGTATGTAATGGTTTGTGTACCTT  
CTGGCATTACAGCTGTTGAGAAACGTGCCGTTATTGATGCGACTCGTCAGGCTGGCGCGCGTGATGCGTA  
TACAATTGAAGAACCGTTTGCTGCAGCAATCGGCGCCAATCTACCGGTCTGGGAGCCAACGGGAAGTATG  
GTAGTAGACATTGGCGGAGGAACAACAGAAGTTGCGATTATTTCTTTAGGAGGAATCGTAACATGTCAGTC  
AATCCGTATCGCTGGGGACGAGATGGATGAAGCGATTATTCAATATATTCGCAAGAATTATAATTTAATGAT  
CGGTGAGCGTACGTGAGAAGCATTAAAAGTAGAAGTCGGTTCTGCCGGAATTCAGAAGGTATTGAAAAC  
ATGGAAATTCGCGGACGTGACTTACTAACAGGTCTACCGAAAACAATCGAAATTTAGCAGAAGAAATTGC  
AGAAGCGCTAAAAGATACAGTGGCTTCTATTGTAGATTGAGTAAAAGTACATTAGAAAAACACCACCTGA  
ACTTGCGGCAGATATTATGGATCGCGGTATTGTATTAACAGGCGGTGGCGCATTGCTACGTAATTTAGATA  
AAGTTATTAGTGAAGAAACAAATATGCCGTTGTCATCGCAGAAGATCCGCTTGACTGTGTTGCAATTGGG  
ACTGGTAAAGCGTTAGAACACATTGATTTATTTAAAAATCGTACAAGCGATTCATATCGCTAAATATTAAGA  
GGTGTAGATCGTGCCACAATTTTTCTTAAATAAACGTTTAGTTATTTTATTAGTCAGTATTATTGTATTAGTG  
GCATTGATTGGTTTTTCGTTAAATGGTCGTAAAAATGTAACGTGGCCTGAACAGTTTGTCAAAGATACGGTT  
GGTCTTGTTGAGGCTACCTTTAATGAACCCGCACAATTTG

## Strain construction

**bSH14-16, 25** [*amyE::erm* GFP – MreBL268F/I279F/M306F/wt respectively] were generated by transforming PY79 with a Gibson assembly consisting of 3 pieces 1) *amyE* upstream amplified with primers oMD191 and oMD232 using gMD423 [*amyE::Phyerspank-mreB::erm*] as template. 2) GFP-MreB top half until mutation site with primers oSH008/011/013 and oSH009/012/14 using gMD208 [*cat::Pxyl-gfp-mreB*] as template. 3) GFP-MreB lower half from mutation site onwards until *amyE* downstream region amplified by oSH010 and oMD197 using gMD423 [*amyE::Phyerspank-mreB::erm*] as template.

**bSH21-24** [*amyE::erm pspac- GFP - megateriumMreBL268F/I279F/M306F/wt* respectively] were generated by transforming PY79 with a Gibson assembly consisting of 3 pieces 1) *amyE* upstream amplified with primers oMD191 and oSH015 with gMD423 [*amyE::Phyperspank-mreB::erm*] as template. 2) gBlock consisting of *B. megaterium MreB* sequence and desired mutations. 3) *amyE* downstream region amplified by oSH016 and oMD197 using gMD423 [*amyE::Phyperspank-mreB::erm*] as template.

**bSH27-29, 33** [ $\Delta$ *mreB amyE::erm pspac- GFP - MreBL268F/I279F/M306F/wt* respectively] were generated by transforming strain BRB2459 with genomic DNA gSH14, 15 and 16 and 25 respectively.

**bSH30-32, 34** [*mbl::cat  $\Delta$ mreB amyE::erm pspac- GFP - MreBL268F* respectively] were generated by transforming strain BSH27-29, 33 with *mbl::cat* amplified from gMD50 [*mbl::cat*] using primers oMD38 and oMD41.

**Overnight culture growth.** All strains were prepared for experimentation as follows: strains were streaked from -80°C freezer stocks onto lysogeny broth (LB) agar plates. Following >12 hours of growth at 37°C, single colonies were transferred to serially diluted overnight bulk liquid cultures in LB placed on a roller drum agitating at 60 rpm, and grown at 25°C. After >12 hours growth to  $OD_{600} < 0.6$ , these starter cultures were transferred to or inoculated into subsequent growth conditions.

**Imaging – phase contrast microscopy.** Phase contrast images were collected on a Nikon Ti microscope equipped with a 6.5  $\mu$ m-pixel CMOS camera and a Nikon 100X NA 1.45 objective. Cells were collected by centrifugation at 6,000 x *g* for 2 min and re-suspended in the original growth medium. Unless otherwise specified, cells were then placed on No. 1.5 cover glass, 24 x 60 mm, under a 1 mm thick agar pad (2-3% agar) containing LB supplemented. Unless otherwise noted, all cells were imaged at 37°C on a heated stage.

**Imaging – total internal reflection microscopy.** Images were collected on a Nikon TI microscope with a 6.5  $\mu\text{m}$ -pixel CMOS camera and a Nikon 100X NA 1.45 objective. 100  $\mu\text{M}$  isopropyl  $\beta$ -D-1-thiogalactopyranoside (IPTG) was added to induce GFP-MreB and the cells were shifted to 37°C and allowed to grow for 2 hours before imaging. Cells were placed on cleaned glass coverslips thickness No. 1.5, as described in the next section. 2% agar pads were prepared in LB supplemented with 100  $\mu\text{M}$  IPTG. Images were collected for 2-3 min at 1 sec intervals. Kymographs of the images were obtained using FIJI.

**Imaging – slide preparation.** Coverslips were sonicated in 1 M KOH for 15 min, followed by 5 washes with water. Coverslips were washed twice with 100% ethanol, and then sonicated in 100% ethanol, followed by one more wash in 100% ethanol. They were stored in ethanol and dried for 10 min before use.

### ***B. subtilis* MreB purification**

*B. subtilis* MreB was cloned into pET11a plasmid and transformed into the *E. coli* strain DH5 $\alpha$ . Strain C43 was used for expression. The primary sequence of the expressed protein was:

MFGIGARDLGLDLGTANTLVFVKGGKIVVREPSVVALQTDTKSIVAVGNDAKNMIGRTP  
GNVVALRPMKDGVIADYETTATMMKYYINQAIKNKGMFTRKPYVMVCVPSGITAVEER  
AVIDATRQAGARDAYPIEEPFAAAIGANLPVWEPTGSMVVDIGGGTTEVAIISLGGIVTS

QSIRVAGDEMDDAIINYIRKTYNLMIGDRTAEAIAKMEIGSAEAEESDNMEIRGRDLLTG  
LPKTIEITGKEISNALRDTVSTIVEAVKSTLEKTPPELAADIMDRGIVLTGGGALLRNLDKV  
ISEETKMPVLIAEDPLDCVAIGTGKALEHIIHLFKGKTRGSKCK

Expression and purification protocols were identical to Mayer *et al.* 2009 (Mayer and Amann 2009).

### ***B. subtilis* MreB labelling**

Standard maleimide labelling protocol was used. Briefly, the buffer pH was adjusted to 7 and a 100 molar excess of TCEP was added. The mixture was kept at room temperature for 20 minutes. Cy5 maleimide was freshly dissolved in dimethylformamide (DMF) and was added to the protein solution in a 1:1, 1:5 and 1:10 molar ratio and kept overnight at 4°C. The excess dye was removed by gel filtration in a NAP-5 column. 10-30% labelling was achieved.

### **Inverse micelle preparation**

Phosphatidylglycerol (PG) and phosphatidylethanolamine (PE) were dissolved in chloroform at 25mg/ml and 10 mg/ml respectively. They were mixed in a glass vial (95% PE and 5% PG) and dried under a stream of nitrogen gas to remove traces of the solvent. The resulting thin lipid film was resuspended in hexadecane in a 1(lipids):2(hexadecane) ratio and mixed thoroughly using glass pipettes until no lipid particles could be seen. The mixture was left to stand for 10-15 minutes.

50  $\mu\text{l}$  of 5  $\mu\text{M}$  MreB solution was taken. 5 mM  $\text{MgCl}_2$ , 1 mM EGTA and 15 mM imidazole (pH 7) were added in the same order to induce polymerization. Immediately, 2  $\mu\text{l}$  of this solution was taken and suspended in 20  $\mu\text{l}$  of the hexadecane-lipid solution. The mixture was pipetted vigorously to produce micelles that were seen to settle at the bottom of the tube. The micelles were imaged immediately.

### **Imaging inverse micelles**

A drop of the micellar solution was placed on a coverslip for imaging. Pre-pulled micropipettes of tip diameters 2, 5 and 10  $\mu\text{m}$  (purchased from World Precision Instruments) were mounted on a micromanipulator (Siskiyou model MX130L) attached to the microscope stage. Using the micromanipulator, the pipette was brought in close proximity to the settled micelles and, when brought close enough, the micelle was able to deform without the requirement of any external suction force. Images were collected on a Nikon TI spinning disk confocal microscope with a Hamamatsu ImagEM (EM-CCD) camera (effective pixel size 160 nm) and Nikon 100X NA 1.45 TIRF objective. Z stacks were obtained at 1  $\mu\text{m}$  slices. Total image depth was 30  $\mu\text{m}$ .

## Bibliography

- Agulleiro, J.I., and Fernandez, J.J. (2011). Fast tomographic reconstruction on multicore computers. *Bioinformatics* 27, 582–583.
- Allison, S.E., D'Elia, M.A., Arar, S., Monteiro, M.A., and Brown, E.D. (2011). Studies of the genetics, function, and kinetic mechanism of TagE, the wall teichoic acid glycosyltransferase in *Bacillus subtilis* 168. *J Biol Chem* 286, 23708–23716.
- Amat, F., Moussavi, F., Comolli, L.R., Elidan, G., Downing, K.H., and Horowitz, M. (2008). Markov random field based automatic image alignment for electron tomography. *J. Struct. Biol.* 161, 260–275.
- Amir, A., and Nelson, D.R. (2012). Dislocation-mediated growth of bacterial cell walls. *Proc Natl Acad Sci USA* 109, 9833–9838.
- Atilano, M.L., Pereira, P.M., Yates, J., Reed, P., Veiga, H., Pinho, M.G., and Filipe, S.R. (2010). Teichoic acids are temporal and spatial regulators. *Proc Natl Acad Sci USA* 107, 18991–18996.
- Atrih, A., Bacher, G., Allmaier, G., Williamson, M.P., and Foster, S.J. (1999). Analysis of peptidoglycan structure from vegetative cells of *Bacillus subtilis* 168 and role of PBP 5 in peptidoglycan maturation. *Journal of Bacteriology* 181, 3956–3966.
- Ausmees, Nora, Jeffrey R Kuhn, and Christine Jacobs-Wagner. 2003. “The Bacterial Cytoskeleton: an Intermediate Filament-Like Function in Cell Shape.” *Cell* 115 (6): 705–13.
- Balyuzi, H., Reaveley, D.A., and Burge, R.E. (1972). X-ray diffraction studies of cell walls and peptidoglycans from Gram-positive bacteria. *Nature New Biol* 235:252–253
- Baskin, Tobias I. 2005. “Anisotropic Expansion of the Plant Cell Wall..” *Annual Review of Cell and Developmental Biology* 21 (1). Annual Reviews: 203–22. doi:10.1146/annurev.cellbio.20.082503.103053.
- Becker, Eric, Nick C Herrera, Felizza Q Gunderson, Alan I Derman, Amber L Dance, Jennifer Sims, Rachel A Larsen, and Joe Pogliano. 2006. “DNA Segregation by the Bacterial Actin AlfA During *Bacillus Subtilis* Growth and Development.” *The EMBO Journal*, November, 1–13.
- Beeby, Morgan, James C Gumbart, Benoît Roux, and Grant J Jensen. 2013. “Architecture and Assembly of the Gram-Positive Cell Wall.” 88 (4): 664–72. doi:10.1111/mmi.12203.



- Ben-Yehuda, S. 2002. "RacA, a Bacterial Protein That Anchors Chromosomes to the Cell Poles." *Science (New York, N.Y.)* 299 (5606): 532–36. doi:10.1126/science.1079914.
- Bi, E F, and J Lutkenhaus. 1991. "FtsZ Ring Structure Associated with Division in Escherichia Coli.." *Nature* 354 (6349): 161–64. doi:10.1038/354161a0.
- Billings, G., Ouzounov, N., Ursell, T., Desmarais, S.M., Shaevitz, J., Gitai, Z., and Huang, K.C. (2014). De novo morphogenesis in L-forms via geometric control of cell growth. *Mol Microbiol* 93, 883–896.
- Birdsell, D.C., Doyle, R.J., and Morgenstern, M. (1975). Organization of teichoic acid in the cell wall of *Bacillus subtilis*. *Journal of Bacteriology* 121, 726–734.
- Bisson-Filho, Alexandre W, Yen-Pang Hsu, Georgia R Squyres, Erkin Kuru, Fabai Wu, Calum Jukes, Yingjie Sun, et al. 2017. "Treadmilling by FtsZ Filaments Drives Peptidoglycan Synthesis and Bacterial Cell Division.." *Science (New York, N.Y.)* 355 (6326). American Association for the Advancement of Science: 739–43. doi:10.1126/science.aak9973.
- Biteen, Julie S, Erin D Goley, Lucy Shapiro, and W E Moerner. 2012. "Three-Dimensional Super-Resolution Imaging of the Midplane Protein FtsZ in Live *Caulobacter Crescentus* Cells Using Astigmatism.." *Chemphyschem : a European Journal of Chemical Physics and Physical Chemistry* 13 (4). WILEY-VCH Verlag: 1007–12. doi:10.1002/cphc.201100686.
- Bonazzi, D., Julien, J.-D., Romao, M., Seddiki, R., Piel, M., Boudaoud, A., and Minc, N. (2014). Symmetry breaking in spore germination relies on an interplay between polar cap stability and spore wall mechanics. *Dev. Cell* 28, 534–546.
- Bork, P, C Sander, and A Valencia. 1992. "An ATPase Domain Common to Prokaryotic Cell Cycle Proteins, Sugar Kinases, Actin, and Hsp70 Heat Shock Proteins.." *Proceedings of the National Academy of Sciences of the United States of America* 89 (16): 7290–94.
- Botella, Eric, Sebastian Hübner, Karsten Hokamp, Annette Hansen, Paola Bisicchia, David Noone, Leigh Powell, Letal I Salzberg, and Kevin M Devine. 2011. "Cell Envelope Gene Expression in Phosphate-Limited *Bacillus Subtilis* Cells.." *Microbiology* 157 (Pt 9). Microbiology Society: 2470–84. doi:10.1099/mic.0.049205-0.
- Bringmann, M., Landrein, B., Schudoma, C., Hamant, O., Hauser, M.-T., and Persson, S. (2012). Cracking the elusive alignment hypothesis: the microtubule-cellulose

- synthase nexus unraveled. *Trends Plant Sci.* 17, 666–674.
- Britton, R A, D C Lin, and A D Grossman. 1998. “Characterization of a Prokaryotic SMC Protein Involved in Chromosome Partitioning..” *Genes & Development* 12 (9): 1254–59.
- Brown, Stephanie, John P Santa Maria Jr., and Suzanne Walker. 2013. “Wall Teichoic Acids of Gram-Positive Bacteria..” *Annual Review of Microbiology* 67 (1): 313–36. doi:10.1146/annurev-micro-092412-155620.
- Cabeen, Matthew T, Godefroid Charbon, Waldemar Vollmer, Petra Born, Nora Ausmees, Douglas B Weibel, and Christine Jacobs-Wagner. 2009. “Bacterial Cell Curvature Through Mechanical Control of Cell Growth..” *The EMBO Journal* 28 (9): 1208–19. doi:10.1038/emboj.2009.61.
- Carballido-López, Rut, Alex Formstone, Ying Li, S Dusko Ehrlich, Philippe Noirot, and Jeff Errington. 2006. “Actin Homolog MreBH Governs Cell Morphogenesis by Localization of the Cell Wall Hydrolase LytE.” *Developmental Cell* 11 (3): 399–409. doi:10.1016/j.devcel.2006.07.017.
- Chang, Fred, and Kerwyn Casey Huang. 2014. “How and Why Cells Grow as Rods..” *BMC Biology* 12 (1). BioMed Central Ltd: 54–11. doi:10.1186/s12915-014-0054-8.
- Charbon, Godefroid, Matthew T Cabeen, and Christine Jacobs-Wagner. 2009. “Bacterial Intermediate Filaments: in Vivo Assembly, Organization, and Dynamics of Crescentin..” *Genes & Development* 23 (9): 1131–44. doi:10.1101/gad.1795509.
- Chen, Baohui, Luke A Gilbert, Beth A Cimini, Joerg Schnitzbauer, Wei Zhang, Gene-Wei Li, Jason Park, et al. 2013. “Dynamic Imaging of Genomic Loci in Living Human Cells by an Optimized CRISPR/Cas System.” *Cell* 155 (7). Elsevier: 1479–91. doi:10.1016/j.cell.2013.12.001.
- Cho, Hongbaek, Carl N Wivagg, Mrinal Kapoor, Zachary Barry, Patricia D A Rohs, Hyunsuk Suh, Jarrod A Marto, Ethan C Garner, and Thomas G Bernhardt. 2016. “Bacterial Cell Wall Biogenesis Is Mediated by SEDS and PBP Polymerase Families Functioning Semi-Autonomously.” *Nature Microbiology* 1 (10): 16172–21. doi:10.1038/nmicrobiol.2016.172.
- D'Elia, M A, K E Millar, T J Beveridge, and E D Brown. 2006. “Wall Teichoic Acid Polymers Are Dispensable for Cell Viability in *Bacillus Subtilis*.” *Journal of Bacteriology* 188 (23): 8313–16. doi:10.1128/JB.01336-06.
- de Boer, P, R Crossley, and L Rothfield. 1992. “The Essential Bacterial Cell-Division Protein FtsZ Is a GTPase..” *Nature* 359 (6392). Nature Publishing Group: 254–56.

doi:10.1038/359254a0.

- Defeu Soufo, Hervé Joël, and Peter L Graumann. 2004. "Dynamic Movement of Actin-Like Proteins Within Bacterial Cells.." *EMBO Reports* 5 (8): 789–94. doi:10.1038/sj.embor.7400209.
- Defeu Soufo, Hervé Joël, and Peter L Graumann. 2006. "Dynamic Localization and Interaction with Other Bacillus Subtilis Actin-Like Proteins Are Important for the Function of MreB." 62 (5): 1340–56. doi:10.1111/j.1365-2958.2006.05457.x.
- Defeu Soufo, Hervé Joël, and Peter L Graumann. 2010. "Bacillus Subtilis MreB Paralogues Have Different Filament Architectures and Lead to Shape Remodelling of a Heterologous Cell System" 78 (5): 1145–58. doi:10.1111/j.1365-2958.2010.07395.x.
- DeLano, W.L. (2002). The PyMOL molecular graphics system.
- Dempwolff, Felix, Christian Reimold, Michael Reth, and Peter L Graumann. 2011. "Bacillus Subtilis MreB Orthologs Self-Organize Into Filamentous Structures Underneath the Cell Membrane in a Heterologous Cell System.." *PLoS ONE* 6 (11): e27035. doi:10.1371/journal.pone.0027035.
- Deng, Yi, Mingzhai Sun, and Joshua W Shaevitz. 2011. "Direct Measurement of Cell Wall Stress Stiffening and Turgor Pressure in Live Bacterial Cells." *Physical Review Letters* 107 (15): 158101. doi:10.1103/PhysRevLett.107.158101.
- Domínguez-Escobar, Julia, Arnaud Chastanet, Alvaro H Crevenna, Vincent Fromion, Roland Wedlich-Söldner, and Rut Carballido-López. 2011. "Processive Movement of MreB-Associated Cell Wall Biosynthetic Complexes in Bacteria.." *Science (New York, N.Y.)* 333 (6039). American Association for the Advancement of Science: 225–28. doi:10.1126/science.1203466.
- Doyle, R.J., McDannel, M.L., Helman, J.R., and Streips, U.N. (1975). Distribution of teichoic acid in the cell wall of Bacillus subtilis. *Journal of Bacteriology* 122, 152–158.
- Draper, Olga, Meghan E Byrne, Zhuo Li, Sepehr Keyhani, Joyce Cueto Barrozo, Grant Jensen, and Arash Komeili. 2011. "MamK, a Bacterial Actin, Forms Dynamic Filaments in Vivo That Are Regulated by the Acidic Proteins MamJ and LimJ" 82 (2). Blackwell Publishing Ltd: 342–54. doi:10.1111/j.1365-2958.2011.07815.x.
- Egan, Alexander J F, and Waldemar Vollmer. 2013. "The Physiology of Bacterial Cell Division.." *Annals of the New York Academy of Sciences* 1277 (January): 8–28. doi:10.1111/j.1749-6632.2012.06818.x.
- Elbaz, Maya, and Sigal Ben-Yehuda. 2010. "The Metabolic Enzyme ManA Reveals a

- Link Between Cell Wall Integrity and Chromosome Morphology..” Edited by William F Burkholder. *PLoS Genetics* 6 (9): e1001119. doi:10.1371/journal.pgen.1001119.
- Errington, Jeff, and Ling Juan Wu. 2017. “Cell Cycle Machinery in *Bacillus Subtilis*..” *Sub-Cellular Biochemistry* 84 (1). Cham: Springer International Publishing: 67–101. doi:10.1007/978-3-319-53047-5\_3.
- Esue, Osigwe, Laura Rupperecht, Sean X Sun, and Denis Wirtz. 2010a. “Dynamics of the Bacterial Intermediate Filament Crescentin in Vitro and in Vivo.” Edited by Amy S Gladfelter. *PLoS ONE* 5 (1). Public Library of Science: e8855. doi:10.1371/journal.pone.0008855.
- Esue, Osigwe, Laura Rupperecht, Sean X Sun, and Denis Wirtz. 2010b. “Dynamics of the Bacterial Intermediate Filament Crescentin in Vitro and in Vivo.” Edited by Amy S Gladfelter. *PLoS ONE* 5 (1). Public Library of Science: e8855. doi:10.1371/journal.pone.0008855.
- Fogel, Michael A, and Matthew K Waldor. 2006. “A Dynamic, Mitotic-Like Mechanism for Bacterial Chromosome Segregation..” *Genes & Development* 20 (23). Cold Spring Harbor Lab: 3269–82. doi:10.1101/gad.1496506.
- Fu, Guo, Tao Huang, Jackson Buss, Carla Coltharp, Zach Hensel, and Jie Xiao. 2010. “In Vivo Structure of the E. Coli FtsZ-Ring Revealed by Photoactivated Localization Microscopy (PALM).” Edited by Michael Polymenis. *PLoS ONE* 5 (9). Public Library of Science: e12680. doi:10.1371/journal.pone.0012680.
- Furchtgott, Leon, Ned S Wingreen, and Kerwyn Casey Huang. 2011. “Mechanisms for Maintaining Cell Shape in Rod-Shaped Gram-Negative Bacteria..” *Molecular Microbiology* 81 (2). Blackwell Publishing Ltd: 340–53. doi:10.1111/j.1365-2958.2011.07616.x.
- Gan, Lu, Songye Chen, and Grant J Jensen. 2008. “Molecular Organization of Gram-Negative Peptidoglycan..” *Proceedings of the National Academy of Sciences* 105 (48). National Acad Sciences: 18953–57. doi:10.1073/pnas.0808035105.
- Garner, E C, R Bernard, W Wang, X Zhuang, D Z Rudner, and T Mitchison. 2011. “Coupled, Circumferential Motions of the Cell Wall Synthesis Machinery and MreB Filaments in *B. Subtilis*.” *Science (New York, N.Y.)* 333 (6039): 222–25. doi:10.1126/science.1203285.
- Garner, Ethan C, Christopher S Campbell, Douglas B Weibel, and R Dyche Mullins. 2007. “Reconstitution of DNA Segregation Driven by Assembly of a Prokaryotic Actin Homolog..” *Science (New York, N.Y.)* 315 (5816). American Association for the Advancement of Science: 1270–74. doi:10.1126/science.1138527.

- Gates, Julie. 2012. "Drosophila Egg Chamber Elongation: Insights Into How Tissues and Organs Are Shaped.." *Fly 6* (4): 213–27. doi:10.4161/fly.21969.
- Gerdes, Kenn, Jakob Møller-Jensen, and Rasmus B Jensen. 2000. "Plasmid and Chromosome Partitioning: Surprises From Phylogeny" 37 (3): 455–66.
- Gerdes, Kenn, Martin Howard, and Florian Szardenings. 2010. "Pushing and Pulling in Prokaryotic DNA Segregation.." *Cell* 141 (6). Elsevier: 927–42. doi:10.1016/j.cell.2010.05.033.
- Glauner, B, J V Høltje, and U Schwarz. 1988. "The Composition of the Murein of Escherichia Coli.." *Journal of Biological Chemistry* 263 (21): 10088–95.
- Govindarajan, Sutharsan, Keren Nevo-Dinur, and Orna Amster-Choder. 2012. "Compartmentalization and Spatio-Temporal Organization of Macromolecules in Bacteria." *FEMS Microbiology Reviews* 36 (5): 1005–22. doi:10.1111/j.1574-6976.2012.00348.x.
- Harris, Leigh K, Natalie A Dye, and Julie A Theriot. 2014. "A Caulobacter MreB Mutant with Irregular Cell Shape Exhibits Compensatory Widening to Maintain a Preferred Surface Area to Volume Ratio" 94 (5): 988–1005. doi:10.1111/mmi.12811.
- Hayhurst, Emma J, Lekshmi Kailas, Jamie K Hobbs, and Simon J Foster. 2008. "Cell Wall Peptidoglycan Architecture in Bacillus Subtilis.." *Proceedings of the National Academy of Sciences of the United States of America* 105 (38): 14603–8. doi:10.1073/pnas.0804138105.
- Holden, Seamus J, Thomas Pengo, Karin L Meibom, Carmen Fernandez Fernandez, Justine Collier, and Suliana Manley. 2014. "High Throughput 3D Super-Resolution Microscopy Reveals Caulobacter Crescentus in Vivo Z-Ring Organization.." *Proceedings of the National Academy of Sciences* 111 (12). National Acad Sciences: 4566–71. doi:10.1073/pnas.1313368111.
- Høltje, J V. 1998. "Growth of the Stress-Bearing and Shape-Maintaining Murein Sacculus of Escherichia Coli.." *Microbiology and Molecular Biology Reviews : MMBR* 62 (1): 181–203.
- Huang, Wan-Zhen, Jyun-Jhih Wang, Hui-Ju Chen, Jung-Tze Chen, and Gwo-Chyuan Shaw. 2013. "The Heat-Inducible Essential Response Regulator WalR Positively Regulates Transcription of sigI, mreBH and lytE in Bacillus Subtilis Under Heat Stress.." *Research in Microbiology* 164 (10): 998–1008. doi:10.1016/j.resmic.2013.10.003.

- Ishii, T., Matsunaga, T., and Hayashi, N. (2001). Formation of Rhamnogalacturonan II-Borate Dimer in Pectin Determines Cell Wall Thickness of Pumpkin Tissue. *Plant Physiol.* 126, 1698–1705.
- Jain, I.H., Vijayan, V., and O'Shea, E.K. (2012). Spatial ordering of chromosomes enhances the fidelity of chromosome partitioning in cyanobacteria. *Proc Natl Acad Sci USA* 109, 13638–13643.
- Jaqaman, Khuloud, Dinah Loerke, Marcel Mettlen, Hirotaka Kuwata, Sergio Grinstein, Sandra L Schmid, and Gaudenz Danuser. 2008. “Robust Single-Particle Tracking in Live-Cell Time-Lapse Sequences.” *Nature Methods* 5 (8): 695–702. doi:10.1038/nmeth.1237.
- Jiang, Chao, Paul D Caccamo, and Yves V Brun. 2015. “Mechanisms of Bacterial Morphogenesis: Evolutionary Cell Biology Approaches Provide New Insights.” *BioEssays* 37 (4): 413–25. doi:10.1002/bies.201400098.
- Jones, L J. 2001. “Control of Cell Shape in Bacteria: Helical, Actin-Like Filaments in *Bacillus Subtilis*..” *Cell* 104 (6): 913–22.
- Kasahara, J., Kiriya, Y., Miyashita, M., Kondo, T., Yamada, T., Yazawa, K., Yoshikawa, R., and Yamamoto, H. (2016). Teichoic Acid Polymers Affect Expression and Localization of dl-Endopeptidase LytE Required for Lateral Cell Wall Hydrolysis in *Bacillus subtilis*. *Journal of Bacteriology* 198, 1585–1594.
- Kawai, Yoshikazu, Jon Marles-Wright, Robert M Cleverley, Robyn Emmins, Shu Ishikawa, Masayoshi Kuwano, Nadja Heinz, et al. 2011. “A Widespread Family of Bacterial Cell Wall Assembly Proteins..” *The EMBO Journal* 30 (24). Nature Publishing Group: 4931–41. doi:10.1038/emboj.2011.358.
- Kawai, Yoshikazu, Kei Asai, and Jeffery Errington. 2009. “Partial Functional Redundancy of MreB Isoforms, MreB, Mbl and MreBH, in Cell Morphogenesis of *Bacillus Subtilis*.” 73 (4): 719–31. doi:10.1111/j.1365-2958.2009.06805.x.
- Kawai, Yoshikazu, Romain Mercier, and Jeff Errington. 2014. “Bacterial Cell Morphogenesis Does Not Require a Preexisting Template Structure.” *Current Biology : CB* 24 (8). The Authors: 863–67. doi:10.1016/j.cub.2014.02.053.
- Kojima, H., Ishijima, A., and Yanagida, T. (1994). Direct measurement of stiffness of single actin filaments with and without tropomyosin by in vitro nanomanipulation. *Proc. Natl. Acad. Sci. U.S.a.* 91, 12962–12966.
- Kremer, J.R., Mastrorarde, D.N., and McIntosh, J.R. (1996). Computer visualization of three-dimensional image data using IMOD. *J. Struct. Biol.* 116, 71–76.

- Kuru, Erkin, H Velocity Hughes, Pamela J Brown, Edward Hall, Srinivas Tekkam, Felipe Cava, Miguel A de Pedro, Yves V Brun, and Michael S VanNieuwenhze. 2012. "In Situ Probing of Newly Synthesized Peptidoglycan in Live Bacteria with Fluorescent D-Amino Acids.." *Angewandte Chemie (International Ed. in English)* 51 (50): 12519–23. doi:10.1002/anie.201206749.
- Kühner, D., Stahl, M., Demircioglu, D.D., and Bertsche, U. (2014). From cells to muropeptide structures in 24 h: peptidoglycan mapping by UPLC-MS. *Sci Rep* 4, 7494.
- Laloux, Géraldine. 2013. "Spatiotemporal Control of PopZ Localization Through Cell Cycle-Coupled Multimerization." *J Cell Biol* 201 (6): 23. doi:10.1038/emboj.2009.412.
- Landgraf, Dirk, Burak Okumus, Peter Chien, Tania A Baker, and Johan Paulsson. 2012. "Segregation of Molecules at Cell Division Reveals Native Protein Localization.." *Nature Methods* 9 (5): 480–82. doi:10.1038/nmeth.1955.
- Leisch, Nikolaus, Jolanda Verheul, Niels R Heindl, Harald R Gruber-Vodicka, Nika Pende, Tanneke den Blaauwen, and Silvia Bulgheresi. 2012. "Growth in Width and FtsZ Ring Longitudinal Positioning in a Gammaproteobacterial Symbiont.." *Current Biology : CB* 22 (19). Elsevier: R831–32. doi:10.1016/j.cub.2012.08.033.
- Li, Rong, and Gregg G Gundersen. 2008. "Beyond Polymer Polarity: How the Cytoskeleton Builds a Polarized Cell." *Nature Reviews Molecular Cell Biology* 9 (11): 860–73. doi:10.1038/nrm2522.
- Li, Zhuo, Michael J Trimble, Yves V Brun, and Grant J Jensen. 2007. "The Structure of FtsZ Filaments in Vivo Suggests a Force-Generating Role in Cell Division." *Embo Journal* 26 (22): 4694–4708. doi:10.1038/sj.emboj.7601895.
- Lim, H C, I V Surovtsev, B G Beltran, F Huang, J Bewersdorf, and C Jacobs-Wagner. 2014. "Evidence for a DNA-Relay Mechanism in ParABS-Mediated Chromosome Segregation." *eLife* 3 (0): e02758–58. doi:10.7554/eLife.02758.031.
- Loskill, P., Pereira, P.M., Jung, P., Bischoff, M., Herrmann, M., Pinho, M.G., and Jacobs, K. (2014). Reduction of the peptidoglycan crosslinking causes a decrease in stiffness of the Staphylococcus aureus cell envelope. *Biophys J* 107, 1082–1089.
- Lu, C, M Reedy, and H P Erickson. 2000. "Straight and Curved Conformations of FtsZ Are Regulated by GTP Hydrolysis.." *Journal of Bacteriology* 182 (1): 164–70.

- Marston, A L, H B Thomaides, D H Edwards, M E Sharpe, and J Errington. 1998. "Polar Localization of the MinD Protein of Bacillus Subtilis and Its Role in Selection of the Mid-Cell Division Site.." *Genes & Development* 12 (21): 3419–30. doi:10.1101/gad.12.21.3419.
- Mastronarde, D.N. (2005). Automated electron microscope tomography using robust prediction of specimen movements. *J. Struct. Biol.* 152, 36–51.
- Matias, Valério R F, and Terry J Beveridge. 2005. "Cryo-Electron Microscopy Reveals Native Polymeric Cell Wall Structure in Bacillus Subtilis 168 and the Existence of a Periplasmic Space" 56 (1): 240–51. doi:10.1111/j.1365-2958.2005.04535.x.
- Mayer, Joshua A, and Kurt J Amann. 2009. "Assembly Properties of the Bacillus Subtilis Actin, MreB.." *Cell Motility and the Cytoskeleton* 66 (2): 109–18. doi:10.1002/cm.20332.
- McKenney, Peter T, Adam Driks, and Patrick Eichenberger. 2013. "The Bacillus Subtilis Endospore: Assembly and Functions of the Multilayered Coat.." *Nature Reviews. Microbiology* 11 (1): 33–44. doi:10.1038/nrmicro2921.
- Meeske, Alexander J, Eammon P Riley, William P Robins, Tsuyoshi Uehara, John J Mekalanos, Daniel Kahne, Suzanne Walker, Andrew C Kruse, Thomas G Bernhardt, and David Z Rudner. 2016. "SEDS Proteins Are a Widespread Family of Bacterial Cell Wall Polymerases.." *Nature* 537 (7622): 634–38. doi:10.1038/nature19331.
- Meier, Elizabeth L, and Erin D Goley. 2014. "Form and Function of the Bacterial Cytokinetic Ring.." *Current Opinion in Cell Biology* 26 (February): 19–27. doi:10.1016/j.ceb.2013.08.006.
- Mercier, R., Kawai, Y., and Errington, J. (2013). Excess membrane synthesis drives a primitive mode of cell proliferation. *Cell* 152, 997–1007.
- Mika, Jacek T, and Bert Poolman. 2011. "Macromolecule Diffusion and Confinement in Prokaryotic Cells.." *Current Opinion in Biotechnology* 22 (1): 117–26. doi:10.1016/j.copbio.2010.09.009.
- Monds, Russell D, Timothy K Lee, Alexandre Colavin, Tristan Ursell, Selwyn Quan, Tim F Cooper, and Kerwyn Casey Huang. 2014. "Systematic Perturbation of Cytoskeletal Function Reveals a Linear Scaling Relationship Between Cell Geometry and Fitness." *Cell Reports* 9 (4). The Authors: 1528–37. doi:10.1016/j.celrep.2014.10.040.
- Moriya, Shigeki, Eitoku Tsujikawa, Anwarul Hassan, Kei Asai, Takeko Kodama, and Naotake Ogasawara. 1998. "A Bacillus Subtilis Gene-Encoding Protein Homologous to Eukaryotic SMC Motor Protein Is Necessary for Chromosome Partition," June, 1–



9.

- Muchová, Katarína, Anthony J Wilkinson, and Imrich Barák. 2011. "Changes of Lipid Domains in *Bacillus Subtilis* Cells with Disrupted Cell Wall Peptidoglycan." *FEMS Microbiology Letters* 325 (1): 92–98. doi:10.1111/j.1574-6968.2011.02417.x.
- Møller-Jensen, Jakob, Jonas Borch, Mette Dam, Rasmus B Jensen, Peter Roepstorff, and Kenn Gerdes. 2003. "Bacterial Mitosis: ParM of Plasmid R1 Moves Plasmid DNA by an Actin-Like Insertional Polymerization Mechanism." *Molecular Cell* 12 (6): 1477–87.
- Narayanaswamy, Rammohan, Matthew Levy, Mark Tsechansky, Gwendolyn M Stovall, Jeremy D O'Connell, Jennifer Mirrieless, Andrew D Ellington, and Edward M Marcotte. 2009. "Widespread Reorganization of Metabolic Enzymes Into Reversible Assemblies Upon Nutrient Starvation." *Proceedings of the National Academy of Sciences*, June, 1–6.
- Nevo-Dinur, Keren, Sutharsan Govindarajan, and Orna Amster-Choder. 2012. "Subcellular Localization of RNA and Proteins in Prokaryotes.." *Trends in Genetics* 28 (7). Elsevier: 314–22. doi:10.1016/j.tig.2012.03.008.
- Nielsen, Henrik J, Jesper R Ottesen, Brenda Youngren, Stuart J Austin, and Flemming G Hansen. 2006. "The *Escherichia Coli* Chromosome Is Organized with the Left and Right Chromosome Arms in Separate Cell Halves" 62 (2). Blackwell Publishing Ltd: 331–38. doi:10.1111/j.1365-2958.2006.05346.x.
- Niki, H, R Imamura, M Kitaoka, K Yamanaka, T Ogura, and S Hiraga. 1992. "E.Coli MukB Protein Involved in Chromosome Partition Forms a Homodimer with a Rod-and-Hinge Structure Having DNA Binding and ATP/GTP Binding Activities.." *Embo Journal* 11 (13): 5101–9.
- Noree, Chalongrat, Brian K Sato, Risa M Broyer, and James E Wilhelm. 2010. "Identification of Novel Filament-Forming Proteins in *Saccharomyces Cerevisiae* and *Drosophila Melanogaster*.." *J Cell Biol* 190 (4). Rockefeller Univ Press: 541–51. doi:10.1083/jcb.201003001.
- Norman, Thomas M, Nathan D Lord, Johan Paulsson, and Richard Losick. 2014. "Memory and Modularity in Cell-Fatedecision Making." *Nature* 503 (7477). Nature Publishing Group: 481–86. doi:10.1038/nature12804.
- O'Connell, Jeremy D, Alice Zhao, Andrew D Ellington, and Edward M Marcotte. 2012. "Dynamic Reorganization of Metabolic Enzymes Into Intracellular Bodies." *Annual Review of Cell and Developmental Biology* 28 (1): 89–111. doi:10.1146/annurev-cellbio-101011-155841.

- Olshausen, von, Philipp, Hervé Joël Defeu Soufo, Kai Wicker, Rainer Heintzmann, Peter L Graumann, and Alexander Rohrbach. 2013. "Superresolution Imaging of Dynamic MreB Filaments in *B. Subtilis*-a Multiple-Motor-Driven Transport?." *Biophysj* 105 (5). Biophysical Society: 1171–81. doi:10.1016/j.bpj.2013.07.038.
- Osawa, Masaki, and Harold P Erickson. 2013. "Liposome Division by a Simple Bacterial Division Machinery.." *Proceedings of the National Academy of Sciences* 110 (27). National Acad Sciences: 11000–11004. doi:10.1073/pnas.1222254110.
- Osawa, Masaki, David E Anderson, and Harold P Erickson. 2008. "Reconstitution of Contractile FtsZ Rings in Liposomes.." *Science (New York, N.Y.)* 320 (5877). American Association for the Advancement of Science: 792–94. doi:10.1126/science.1154520.
- Osawa, Masaki, David E Anderson, and Harold P Erickson. 2009. "Curved FtsZ Protofilaments Generate Bending Forces on Liposome Membranes.." *The EMBO Journal* 28 (22). EMBO Press: 3476–84. doi:10.1038/emboj.2009.277.
- Ouzounov, Nikolay, Jeffrey P Nguyen, Benjamin P Bratton, David Jacobowitz, Zemer Gitai, and Joshua W Shaevitz. 2016. "MreB Orientation Correlates with Cell Diameter in *Escherichia Coli*." *Biophysj* 111 (5). Biophysical Society: 1035–43. doi:10.1016/j.bpj.2016.07.017.
- Ozyamak, Ertan, Justin Kollman, David A Agard, and Arash Komeili. 2013. "The Bacterial Actin MamK: in Vitro Assembly Behavior and Filament Architecture.." *The Journal of Biological Chemistry* 288 (6). American Society for Biochemistry and Molecular Biology: 4265–77. doi:10.1074/jbc.M112.417030.
- Pandey, Rachna, Alex Ter Beek, Norbert O E Vischer, Jan P P M Smelt, Stanley Brul, and Erik M M Manders. 2013. "Live Cell Imaging of Germination and Outgrowth of Individual *Bacillus Subtilis* Spores; the Effect of Heat Stress Quantitatively Analyzed with SporeTracker." Edited by Adam Driks. *PLoS ONE* 8 (3): e58972–10. doi:10.1371/journal.pone.0058972.
- Paredez, A R. 2006. "Visualization of Cellulose Synthase Demonstrates Functional Association with Microtubules." *Science (New York, N.Y.)* 312 (5779): 1491–95. doi:10.1126/science.1126551.
- Pettersen, E.F., Goddard, T.D., Huang, C.C., Couch, G.S., Greenblatt, D.M., Meng, E.C., and Ferrin, T.E. (2004). UCSF Chimera—A visualization system for exploratory research and analysis. *Journal of Computational Chemistry* 25, 1605–1612.

- Phillips, R., Kondev, J., Theriot, J., and Garcia, H. (2012). *Physical Biology of the Cell* (Garland Science).
- Polka, J K, J M Kollman, D A Agard, and R D Mullins. 2009. "The Structure and Assembly Dynamics of Plasmid Actin Alfa Imply a Novel Mechanism of DNA Segregation." *Journal of Bacteriology* 191 (20): 6219–30. doi:10.1128/JB.00676-09.
- Pollard, Thomas D, and Gary G Borisy. 2003. "Cellular Motility Driven by Assembly and Disassembly of Actin Filaments.." *Cell* 112 (4): 453–65.
- Pooley, H.M., Abellan, F.-X., and Karamata, D. (1993). Wall Teichoic Acid, Peptidoglycan Synthesis and Morphogenesis in *Bacillus Subtilis*. In *Bacterial Growth and Lysis*, (Boston, MA: Springer, Boston, MA), pp. 385–392.
- Ptacin, Jerod L, Steven F Lee, Ethan C Garner, Esteban Toro, Michael Eckart, Luis R Comolli, W E Moerner, and Lucy Shapiro. 2010. "A Spindle-Like Apparatus Guides Bacterial Chromosome Segregation." *Nature Cell Biology* 12 (8): 791–98. doi:10.1038/ncb2083.
- Ramamurthi, Kumaran S, Sigolene Lecuyer, Howard A Stone, and Richard Losick. 2009. "Geometric Cue for Protein Localization in a Bacterium.." *Science (New York, N.Y.)* 323 (5919): 1354–57. doi:10.1126/science.1169218.
- Raskin, David M, and Piet A J de Boer. 1999. "Rapid Pole-to-Pole Oscillation of a Protein Required for Directing Division to the Middle of Escherichia Coli," *Proceedings of the National Academy of Sciences of the United States of America* 96 (9): 4971–76.
- Redgwell, R.J., MacRae, E., Hallett, I., Fischer, M., and Perry, J. (1997). In vivo and in vitro swelling of cell walls during fruit ripening. *Planta* 203, 162–173
- Reimold, Christian. 2013. "Motion of Variable-Length MreB Filaments at the Bacterial Cell Membrane Influences Cell Morphology.." *Molecular Biology of the Cell*, June, 31. doi:10.1091/mbc.E12-10-0728.
- Renner, L.D., Eswaramoorthy, P., Ramamurthi, K.S., and Weibel, D.B. (2013). Studying biomolecule localization by engineering bacterial cell wall curvature. *PLoS ONE* 8, e84143.
- Saberi, Saeed, and Eldon Emberly. 2010. "Chromosome Driven Spatial Patterning of Proteins in Bacteria.." Edited by James M Briggs. *PLoS Computational Biology* 6 (11). Public Library of Science: e1000986. doi:10.1371/journal.pcbi.1000986.
- Safran, S.A. (2003). *Statistical thermodynamics of surfaces, interfaces, and membranes* (Westview Press).

- Salje, Jeanne, Fusinita van den Ent, Piet de Boer, and Jan Löwe. 2011. "Direct Membrane Binding by Bacterial Actin MreB." *Molecular Cell* 43 (3). Elsevier Inc.: 478–87. doi:10.1016/j.molcel.2011.07.008.
- Schindelin, J., Arganda-Carreras, I., Frise, E., Kaynig, V., Longair, M., Pietzsch, T., Preibisch, S., Rueden, C., Saalfeld, S., Schmid, B., et al. (2012). Fiji: an open-source platform for biological-image analysis. *Nat. Methods* 9, 676–682.
- Schirner, Kathrin, Laura K Stone, and Suzanne Walker. 2011. "ABC Transporters Required for Export of Wall Teichoic Acids Do Not Discriminate Between Different Main Chain Polymers.." *ACS Chemical Biology* 6 (5): 407–12. doi:10.1021/cb100390w.
- Schneider, C.A., Rasband, W.S., and Eliceiri, K.W. (2012). NIH Image to ImageJ: 25 years of image analysis. *Nat. Methods* 9, 671–675.
- Sochacki, K.A., Shkel, I.A., Record, M.T., and Weisshaar, J.C. (2011). Protein diffusion in the periplasm of *E. coli* under osmotic stress. *Biophys J* 100, 22–31.
- Strauss, Michael P, Andrew T F Liew, Lynne Turnbull, Cynthia B Whitchurch, Leigh G Monahan, and Elizabeth J Harry. 2012. "3D-SIM Super Resolution Microscopy Reveals a Bead-Like Arrangement for FtsZ and the Division Machinery: Implications for Triggering Cytokinesis." Edited by Linda Amos. *PLoS Biology* 10 (9). Public Library of Science: e1001389. doi:10.1371/journal.pbio.1001389.
- Swulius, Matthew T, and Grant J Jensen. 2012. "The Helical MreB Cytoskeleton in *Escherichia Coli* MC1000/pLE7 Is an Artifact of the N-Terminal Yellow Fluorescent Protein Tag.." *Journal of Bacteriology* 194 (23). American Society for Microbiology: 6382–86. doi:10.1128/JB.00505-12.
- Swulius, Matthew T, Songye Chen, H Jane Ding, Zhuo Li, Ariane Briegel, Martin Pilhofer, Elitza I Tocheva, et al. 2011. "Long Helical Filaments Are Not Seen Encircling Cells in Electron Cryotomograms of Rod-Shaped Bacteria.." *Biochemical and Biophysical Research Communications* 407 (4): 650–55. doi:10.1016/j.bbrc.2011.03.062.
- Szardenings, Florian, David Guymier, and Kenn Gerdes. 2011. "ParA ATPases Can Move and Position DNA and Subcellular Structures.." *Current Opinion in Microbiology* 14 (6): 712–18. doi:10.1016/j.mib.2011.09.008.
- Szwedziak, P., Wang, Q., Bharat, T.A.M., Tsim, M., and Löwe, J. (2014). Architecture of the ring formed by the tubulin homologue FtsZ in bacterial cell division. *Elife* 3, e04601.

- Teleman, A A, P L Graumann, D C Lin, A D Grossman, and R Losick. 1998. "Chromosome Arrangement Within a Bacterium.." *Current Biology : CB* 8 (20): 1102–9.
- Thanbichler, Martin, and Lucy Shapiro. 2006. "MipZ, a Spatial Regulator Coordinating Chromosome Segregation with Cell Division in *Caulobacter*." *Cell* 126 (1). Elsevier: 147–62. doi:10.1016/j.cell.2006.05.038.
- Thomas, Kieth J, and Charles V Rice. 2014. "Revised Model of Calcium and Magnesium Binding to the Bacterial Cell Wall." *BioMetals* 27 (6). Springer Netherlands: 1361–70. doi:10.1007/s10534-014-9797-5.
- Thompson, D'Arcy Wentworth. *On Growth and Form*. Cambridge: Cambridge UP, 1968. Print
- Thompson, Stephen R, George H Wadhams, and Judith P Armitage. 2006. "The Positioning of Cytoplasmic Protein Clusters in Bacteria.." *Proceedings of the National Academy of Sciences of the United States of America* 103 (21). National Acad Sciences: 8209–14. doi:10.1073/pnas.0600919103.
- Tinevez, J.-Y., Perry, N., Schindelin, J., Hoopes, G.M., Reynolds, G.D., Laplantine, E., Bednarek, S.Y., Shorte, S.L., and Eliceiri, K.W. (2017). TrackMate: An open and extensible platform for single-particle tracking. *Methods* 115, 80–90.
- Typas, Athanasios, Manuel Banzhaf, Carol A Gross, and Waldemar Vollmer. 2012. "From the Regulation of Peptidoglycan Synthesis to Bacterial Growth and Morphology.." *Nature Reviews. Microbiology* 10 (2): 123–36. doi:10.1038/nrmicro2677.
- Ursell, Tristan S, Jeffrey Nguyen, Russell D Monds, Alexandre Colavin, Gabriel Billings, Nikolay Ouzounov, Zemer Gitai, Joshua W Shaevitz, and Kerwyn Casey Huang. 2014. "Rod-Like Bacterial Shape Is Maintained by Feedback Between Cell Curvature and Cytoskeletal Localization.." *Proceedings of the National Academy of Sciences* 111 (11). National Acad Sciences: E1025–34. doi:10.1073/pnas.1317174111.
- Ursell, T., Lee, T.K., Shiomi, D., Shi, H., Tropini, C., Monds, R.D., Colavin, A., Billings, G., Bhaya-Grossman, I., Broxton, M., et al. (2017). Rapid, precise quantification of bacterial cellular dimensions across a genomic-scale knockout library. *BMC Biol.* 15, 17.
- van den Ent, Fusinita, Thierry Izoré, Tanmay AM Bharat, Christopher M Johnson, and Jan Löwe. 2014. "Bacterial Actin MreB Forms Antiparallel Double Filaments.." *eLife*

3 (May): e02634. doi:10.7554/eLife.02634.

- van Teeffelen, Sven, Siyuan Wang, Leon Furchtgott, Kerwyn Casey Huang, Ned S Wingreen, Joshua W Shaevitz, and Zemer Gitai. 2011. "The Bacterial Actin MreB Rotates, and Rotation Depends on Cell-Wall Assembly.." *Proceedings of the National Academy of Sciences of the United States of America* 108 (38). National Acad Sciences: 15822–27. doi:10.1073/pnas.1108999108.
- Verwer, R W. 1980. "Oriented Fragmentation of Escherichia Coli Sacculi by Sonication.." *Journal of Bacteriology* 141 (1). American Society for Microbiology (ASM): 6.  
[http://www.ncbi.nlm.nih.gov/entrez/query.fcgi?cmd=Retrieve&db=PubMed&dopt=Citation&list\\_uids=6986361](http://www.ncbi.nlm.nih.gov/entrez/query.fcgi?cmd=Retrieve&db=PubMed&dopt= Citation&list_uids=6986361).
- Wachi, M., and Matsushashi, M. (1989). Negative control of cell division by mreB, a gene that functions in determining the rod shape of Escherichia coli cells. *Journal of Bacteriology* 171, 3123–3127.
- Wang, Siyuan, and Ned S Wingreen. 2013. "Cell Shape Can Mediate the Spatial Organization of the Bacterial Cytoskeleton.." *Biophysical Journal* 104 (3). Elsevier: 541–52. doi:10.1016/j.bpj.2012.12.027.
- Wang, Siyuan, Jeffrey R Moffitt, Graham T Dempsey, X Sunney Xie, and Xiaowei Zhuang. 2014. "Characterization and Development of Photoactivatable Fluorescent Proteins for Single-Molecule-Based Superresolution Imaging.." *Proceedings of the National Academy of Sciences* 111 (23). National Acad Sciences: 8452–57. doi:10.1073/pnas.1406593111.
- Wang, Xindan, Paula Montero Llopis, and David Z Rudner. 2014. "Bacillus Subtilis Chromosome Organization Oscillates Between Two Distinct Patterns.." *Proceedings of the National Academy of Sciences* 111 (35). National Acad Sciences: 12877–82. doi:10.1073/pnas.1407461111.
- Wang, Xindan, Xun Liu, Christophe Possoz, and David J Sherratt. 2006. "The Two Escherichia Coli Chromosome Arms Locate to Separate Cell Halves.." *Genes & Development* 20 (13). Cold Spring Harbor Lab: 1727–31. doi:10.1101/gad.388406.
- Webb, C D, A Teleman, S Gordon, A Straight, A Belmont, D C Lin, A D Grossman, A Wright, and R Losick. 1997. "Bipolar Localization of the Replication Origin Regions of Chromosomes in Vegetative and Sporulating Cells of B. Subtilis.." *Cell* 88 (5). Elsevier: 667–74. doi:10.1016/S0092-8674(00)81909-1.
- Whatmore, A.M., and Reed, R.H. (1990). Determination of turgor pressure in Bacillus subtilis: a possible role for K<sup>+</sup> in turgor regulation. *J. Gen. Microbiol.* 136, 2521–

2526.

- White, Courtney L, and James W Goyer. 2012. "MreB: Pilot or Passenger of Cell Wallsynthesis?." *Trends in Microbiology* 20 (2). Elsevier Ltd: 74–79.  
doi:10.1016/j.tim.2011.11.004.
- Wyrick, P B, and H J Rogers. 1973. "Isolation and Characterization of Cell Wall-Defective Variants of Bacillus Subtilis and Bacillus Licheniformis.." *Journal of Bacteriology* 116 (1). American Society for Microbiology (ASM): 456–65.
- Yao, X, M Jericho, D Pink, and T Beveridge. 1999. "Thickness and Elasticity of Gram-Negative Murein Sacculi Measured by Atomic Force Microscopy.." *Journal of Bacteriology* 181 (22): 6865–75.
- Young, Kevin D. 2010. "Bacterial Shape: Two-Dimensional Questions and Possibilities." *Annual Review of Microbiology* 64 (1): 223–40.  
doi:10.1146/annurev.micro.112408.134102.
- Yu, H., Yan, X., Shen, W., Shen, Y., and Zhang, J. (2010). Efficient and precise construction of markerless manipulations in the Bacillus subtilis genome. *Journal of Microbiology*, 20(1):45-53
- Zheng, Hai, Po-Yi Ho, Meiling Jiang, Bin Tang, Weirong Liu, Dengjin Li, Xuefeng Yu, Nancy E Kleckner, Ariel Amir, and Chenli Liu. 2016. "Interrogating the Escherichia Coli Cell Cycle by Cell Dimension Perturbations.." *Proceedings of the National Academy of Sciences* 113 (52). National Acad Sciences: 15000–15005.  
doi:10.1073/pnas.1617932114.
- Zhong-Can, O.Y., and Helfrich, W. (1989). Bending energy of vesicle membranes: General expressions for the first, second, and third variation of the shape energy and applications to spheres and cylinders. *Phys. Rev. A* 39, 5280–5288.
- Zimmerman, S B, and S O Trach. 1991. "Estimation of Macromolecule Concentrations and Excluded Volume Effects for the Cytoplasm of Escherichia Coli.." *Journal of Molecular Biology* 222 (3): 599–620.